T-CYCLE EPR Development at 275 GHz for the study of reaction kinetics & intermediates

Panarelli, E.G.

Cover Page

Universiteit Leiden

The handle http://hdl.handle.net/1887/68233 holds various files of this Leiden University dissertation.

Author: Panarelli, E.G.
Title: T-CYCLE EPR Development at 275 GHz for the study of reaction kinetics & intermediates
Issue Date: 2018-12-10

T-CYCLE EPR
Development at 275 GHz for the study of reaction kinetics & intermediates.

Proefschrift

ter verkrijging van
de graad van Doctor aan de Universiteit Leiden,
op gezag van Rector Magnificus prof.mr. C.J.J.M. Stolker,
volgens besluit van het College voor Promoties
te verdedigen op maandag 10 december 2018
klokke 16.15 uur

door

Enzo Gabriele Panarelli

geboren te Cuneo (Italië)
in 1989

Contents

1

Introduction

1.1 Motivation and scope

Over the past century, scientific breakthroughs whose contributors were bestowed with a Nobel prize have been achieved in a wide range of fields thanks to studies related to chemical kinetics. In biochemistry, for instance, fundamental chemical kinetics investigations allowed to unravel the biocatalytical role of RNA [1], and to shed light on the mechanisms of protein degradation [2], of DNA repair [3], and of the synthesis of ATP [4] [5]. In inorganic chemistry, important studies clarified, for instance, the adsorption of gases on solid surfaces [6] [7], the mechanism of certain chain reactions [8], the mechanism of formation and decomposition of ozone [9], the dynamics of chemical elementary processes [10], and molecular dynamics on the femtosecond time scale [11].

Given the wealth of information that can be derived from chemical kinetics, it is important to develop methodologies for detection of reactive species with adequate time resolution. Coupling kinetic information with structural information opens the doors to understanding the mechanisms and functions of reactive (bio)chemical systems. This thesis is devoted to the development of methods for kinetic investigations (Rapid Freeze-Quench and Temperature-Cycle), coupled with the spectroscopic technique of choice for structural investigations of paramagnetic spin systems, namely Electron Paramagnetic Resonance, particularly at high magnetic field [12].

In this introductory Chapter the necessary background is provided to understand the research described in this thesis. First, the grounds of the theory of chemical kinetics are outlined, which allow the qualitative and quantitative interpretation of chemical reactivity. Following, an overview is given on Rapid Freeze-Quench, one of the most widespread methods to freeze reaction intermediates for spectroscopic characterization. Next, an alternative method to investigate chemical reactions is introduced. Finally, the theory and applications are presented of Electron Paramagnetic Resonance, the spectroscopic technique used for the kinetic investigations throughout this research.

1.2 Chemical kinetics

The study of the kinetics of reactive chemical species can give important insights in the understanding of the mechanism and function of a dynamical chemical system. In enzymatic reactions, for example, knowing about the reaction mechanism may unravel the entire functioning of proteins and their relations with the more complex biological contexts they operate in. As the main subject of this thesis is, in broad sense, the development of a method to qualitatively and quantitatively study reactive chemical systems, ample use has been made of concepts deriving from

the theory of chemical kinetics, whose principles are briefly described hereinafter. Way more complete descriptions can be found in textbooks, like [13].

A chemical reaction is characterized by its *velocity*, namely the rate at which reactants are depleted and products are generated, defined by the so-called *rate law* of a reaction. A simple and generic chemical reaction may be written as follows:

$$c_A A + c_B B \longrightarrow c_P P \tag{1.1}$$

where A and B are two reactants, which react to yield a product P. c_A, c_B, and c_P are the stoichiometric coefficients of A, B, and P, respectively. The velocity $v(t)$ at which A and B are depleted, or P is formed, defines the rate law of the reaction, and can be written as Equation 1.2:

$$v(t) = -\frac{1}{c_A}\frac{d[A]}{dt} = -\frac{1}{c_B}\frac{d[B]}{dt} = +\frac{1}{c_P}\frac{d[P]}{dt} \tag{1.2}$$

where [A], [B], and [P] are the concentrations (in mol per volume unit) of species A, B, and P, respectively. The negative sign indicates the depletion of the reagents, while the positive sign indicates the generation of the product.

Experimentally, the rate law can be related to the concentration of the reagents through a proportionality constant k, called *rate constant*. Equation 1.2 can thus also be written as:

$$v(t) = k[A]^a[B]^b \tag{1.3}$$

where k is the rate constant of the reaction, and a and b are coefficients whose sum expresses the *order of reaction*, and commonly takes on the values of 0, 1, 2, or half-integer numbers. It is important to notice that the value of k, as well as the order of reaction, are properties that can only be determined experimentally.

Bimolecular reactions of the kind expressed by Equation 1.1 are often of second order, meaning that the coefficients a and b are equal to 1 and their sum is 2. Determining the rate constant of a second-order reaction is possible by adjusting the experimental conditions such that one of the two reactants (say B) is present in excess concentration as compared to the other. When $[B] \gg [A]$, the concentration of B does not change significantly in time, so that it can be approximated to a constant, and be included in the rate constant. Equation 1.3 can thus be written as:

$$k[\text{A}][\text{B}] \cong k'[\text{A}] \tag{1.4}$$

where $k' = k[\text{B}]$ is the *apparent* rate constant. From Equations 1.2, 1.3, and 1.4, the dependence of the concentration of one reactant on time can be expressed analytically:

$$\frac{d[\text{A}]}{dt} = -k'[\text{A}] \tag{1.5}$$

where the stoichiometric coefficient c_A was set, for simplicity, to 1. Since the form of Equation 1.5 resembles the rate law of a first-order reaction, such conditions are called of *pseudo-first order*. By integrating Equation 1.5, the resulting dependence of [A] on time turns out to be exponential:

$$[\text{A}]_t = [\text{A}]_0 e^{-k't} \tag{1.6}$$

where $[\text{A}]_t$ and $[\text{A}]_0$ are, respectively, the concentration of reagent A at time t, and the initial concentration of reagent A. It is clear from Equation 1.6 that operating under pseudo-first-order conditions is an advantage when studying the kinetics of a chemical reaction, because the concentration dependence of one single reactant as a function of time takes the form of a simple exponential and can be easily linearized. Pseudo-first-order conditions were used in Chapters 2 and 4 of this thesis.

In spite of its name, a rate constant is not really constant, because it depends on several physical conditions of the reacting system, most importantly the temperature. An empirical relation between k and T was found by the Swedish scientist Svante Arrhenius [14], after whom the following equation takes its name:

$$k(T) = \mathcal{A}e^{-\frac{E_a}{RT}} \tag{1.7}$$

where $\mathcal{A}$ is a constant called pre-exponential factor, E_a is the *activation energy* of the reaction (which is an inherent property of the reaction and does not depend on temperature), and R is the universal gas constant. The Arrhenius equation is found to be valid for many reactions; however, there exist variations on such an equation that plug in additional terms (for instance, a temperature-dependent pre-exponential factor) to account for deviations of some reactions from the simple Arrhenius behaviour. The activation energy featuring in Equation 1.7 represents the kinetic barrier the reactants have to go through in order to reach the so-called transition state,

which evolves into the product [15]. Thermodynamic formulations of the Arrhenius equation, such as the Eyring equation [16], correlate the activation energy to the Gibbs energy of activation, which contains the activation enthalpy used to define whether a reaction is endo- or exothermic. When the activation enthalpy is positive, the reaction is called *endothermic*, as it requires energy to progress, and the rate constant increases as a function of temperature. On the contrary, when the activation enthalpy is negative, the reaction is *exothermic*, meaning it releases energy as heat as it progresses, and the rate constant decreases as a function of temperature.

Equation 1.7 can be used to plot the logarithm of k versus $\frac{1}{T}$ (known as Arrhenius plot) to find the activation energy when the behaviour of k as a function of T is known. Use of the Arrhenius plot is made in the analysis of Chapter 4 of this thesis.

Many chemical reactions, like virtually all enzymatic reactions, do not occur in one single step that turns the reagent(s) directly to the product(s). Rather, several intermediate steps take place, each one of them producing a transient species that serves as the reagent for the next step. A chemical reaction can thus be conceived as a sequence of *elementary reactions*, each defined by a rate constant k_j and an intermediate species I_j:

$$A + R_1 \underset{k_{-1}}{\overset{k_1}{\rightleftharpoons}} I_1 + R_2 \underset{k_{-2}}{\overset{k_2}{\rightleftharpoons}} I_2 + R_3 \underset{k_{-3}}{\overset{k_3}{\rightleftharpoons}} \cdots \underset{k_{-n}}{\overset{k_n}{\rightleftharpoons}} P \tag{1.8}$$
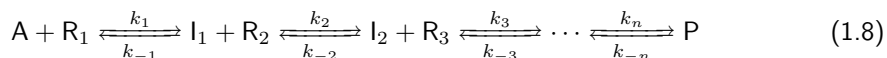
where A is the initial reagent, R_j are the reactive species involved in each step, and P is the final product. The R_j's are not necessarily present, as the intermediates I_j might evolve spontaneously to the next product. In principle each elementary reaction may or may not be in chemical equilibrium (indicated by the double arrows), characterized by a forward rate constant (k_j) and a backward rate constant (k_{-j}).

An important feature of the reaction intermediates is their transient nature. Reaction intermediates tend to be energetically unstable, so that their conversion towards the products is highly favourable and fast [17]. For this reason, their concentration during the reaction peaks well before the reaction is complete. Also, their concentration tends to be much lower than that of the reagent(s) and the product(s), given the high rate of conversion to the product(s). The typical concentration profile as a function of time of an intermediate of a first-order reaction can be seen in Figure 1.1, where, as the concentration of reagent A (in red) decreases exponentially and the product P (in blue) is generated, the intermediate I (in green) peaks at some point during the reaction, and then fades away upon completion of the reaction. A great many (bio)chemical reactions occur in short time scales (e.g., in milliseconds), like those under study in Chapter 2, 4, and 5 of this thesis. The reaction intermediates of such reactions are therefore not easy

to detect, as the time they exist during the reaction is extremely short, and their usually low concentration does not help detecting them. For this reason, several techniques have emerged to address the problem of intermediate detection.
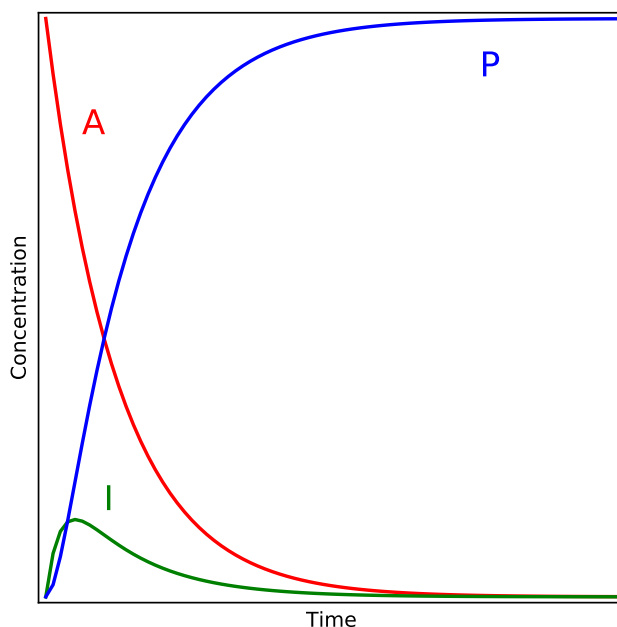
Figure 1.1: Concentration profiles of the species involved in a simple first-order reaction of the kind A $\xrightarrow{k_1}$ I $\xrightarrow{k_2}$ P, with A being the reagent (plotted in red), I the intermediate (plotted in green), and P the product (plotted in blue). Notice that in this example no equilibrium is considerered in between the elementary reactions. Furthermore, the second elementary reaction, generating the product from the intermediate, is faster than the first elementary reaction, being $k_2 = 5k_1$.

1.3 Rapid Freeze-Quench

One of the most commonly used techniques to trap reaction intermediates on time scales of milliseconds is the so-called Rapid Freeze-Quench (RFQ), first implemented by Bray in 1961 [18] and in use ever since. Owing to the relatively high time resolution of this technique (down to milliseconds), and to the possibility to couple it to several spectroscopic detection methods, RFQ has been improved over the years and widely employed in combination with Electron Paramagnetic

Resonance (EPR). Chapter 2 of this thesis is devoted to the coupling of RFQ to high-frequency EPR, and many details are provided there. Here, a brief introduction to the principles of RFQ is provided.

RFQ consists of the rapid reaction quench of a mixture of two or more chemically reactive samples, caused by the mixture's fast freezing in a cryogenic bath. Prior to the freezing, the reagents have first rapidly and homogeneously mixed and then reacted for a well-defined amount of time. In the setup used for the experiments of Chapter 2 of this thesis, the two reactants (here labeled A and B) are contained in two separate syringes that are mounted on a stage coupled to a ram. The ram is connected to a console-controlled servo motor that can move the ram upwards, thereby pushing the pistons of the syringes symmetrically and injecting equal volumes of the solutions of reactants to the mixer, to which the syringes are connected by suitable plastic tubes. The mixer is specifically designed to rapidly and homogeneously mix the two reactant solutions before injecting them to a so-called *aging tube*, whose length is one of the parameters that determine the reaction time (t_r) of the mixture. At the end of the aging tube is a nozzle that sprays the mixture into a cryogenic bath (most commonly isopentane at a temperature of about 140 K). The cold medium immediately freezes the droplets of mixture, thereby quenching the reaction at a specific t_r. The frozen droplets take the shape of particles that can be collected in a sample holder for later measurements. Specifically in this thesis (see Chapter 2), the RFQ particles were collected in EPR tubes and later transferred into smaller capillaries suitable for high-frequency EPR.

In the RFQ setup used in Chapter 2, three parameters can be directly set in the ram-controlling console, which will determine the *reaction time* of the mixture for a given length of the aging tube. These parameters are:

- the *ram velocity* U_R (between 0.8 and 8 cm s^{-1}), which is the actual velocity of the ram;

- the *total displacement* d_T (between 0.01 and 10 cm per experiment), which is the length by which the ram moves per experiment;

- the delay factor, which sets one or more incubation times between consecutive ram displacements.

For the RFQ experiment designed in Chapter 2, only the first two settings were taken into account. In what follows is shown how the ram velocity and the total displacement directly affect the *flow rate* of the mixture pushed by the pistons through the syringes to the mixer and the

aging tube. The flow rate in turn affects the reaction time, which is the time the mixture spends in the aging tube, and thus the time amount by which the reaction has progressed. Notice that the following equations were derived from [19], whose notation is reproduced here.

The flow rate (in mL s^{-1}) is described by the continuity equation relating the ram velocity (directly set from the console) and the flow velocity in the aging tube:

$$Q = A_s U_R = A_r U_x \tag{1.9}$$

where A_s is the cross-sectional area of the syringe (in cm^2), U_R is the ram velocity (in cm s^{-1}), A_r is the cross-sectional area of the aging tube (in cm^2), and U_x is the flow velocity in the aging tube (in cm s^{-1}). Since the cross-sectional area of the syringe is related to the total volume of the syringe, being $V_s = A_s d_T$, it results from Equation 1.9 that $Q = \frac{V_s}{d_T} U_R$, which indicates that the flow rate is directly determined by the console-controlled ram velocity and total displacement.

Since the flow velocity in the aging tube can be expressed as $U_x = l_r/t_r$, the numerator being the length of the aging tube and the denominator being the time the mixture spends in the reaction tube (or reaction time), through Equation 1.9 it is possible to express the reaction time as:

$$t_r = \frac{l_r}{U_x} = \frac{A_r}{A_s} \frac{l_r}{U_R} = \left(\frac{D_r}{D_s}\right)^2 \frac{l_r}{U_R} \tag{1.10}$$

where D_r and D_s are the diameters of the aging tube and of the syringe, respectively. In the experiments described in Chapter 2 of this thesis, they have values of 0.05 cm and 0.7 cm, respectively, while the ram velocity is set to 3.2 cm s^{-1}. In this way, once the console parameters are set, and the syringe volume and the aging tube diameter are known, Equation 1.10 allows to calculate the reaction time per RFQ experiment only as a function of the length of the aging tube.

A final important remark concerns the so-called *dead time* or — as is called in Chapter 2 — the *freezing time* of the RFQ setup. Owing to the connections between the tubes, the syringes, and the mixer, any RFQ setup has an intrinsic *dead volume* that is filled by the mixture during the freezing time, which adds up to the actual reaction time. The temporal outcome of a RFQ experiment is thus expressed in terms of an overall non-consistently defined *aging time* [20] or *quenching time* [21], which has to be corrected by the freezing time (determined experimentally) when performing quantitative kinetic studies with RFQ.

1.4   Laser-induced Temperature-jumps

The laser-induced Temperature-jump (T-jump) methodology was originally developed to study the relaxation of (bio)chemical systems in equilibrium, following the perturbation of the equilibrium induced by a heat source (such as an electrical discharge [22] or a near-infrared (NIR) laser pulse [23]), which causes the system to quickly reach a higher temperature before going back to the initial temperature after the heat source is turned off. Particularly in the case of a laser-induced T-jump, the absorption of the NIR energy, typically by the solvent molecules (e.g., water), results in the heating of the sample volume, with a temperature difference (ΔT) that depends on:

- the heat conductivity and heat capacity of the solvent and sample holder;

- the optical intensity of the laser pulse;

- the optical absorption of the solvent molecules at a specific excitation wavelength.

In this thesis, a laser-induced T-jump methodology was developed, in combination with high-frequency Electron Paramagnetic Resonance (hence named T-Cycle EPR), for the investigation of reaction kinetics between two chemically reactive species. The T-jump method developed here has similarities with the one employed for relaxation studies. However, the important difference with T-jump relaxation methodologies is that T-Cycle EPR involves the application of T-jumps on a system that does not feature any chemical equilibrium, i.e., a frozen mixture of reactants where no reaction is taking place. As such, the method is thus not developed with the aim of observing the relaxation of the system back to its equilibrium state following a laser-induced T-jump. Rather, the jumps applied here serve as "heating shots" that warm up the system to a temperature where a chemical reaction can take place for a certain amount of time, to which follows the return of the system to a frozen state where no reaction occurs. This allows the observation of the step-wise progress of a chemical reaction as a function of time, with no focus whatsoever as regards the relaxation of the system.

An important aspect of the sample heating with a laser pulse for kinetic studies is that it should take place homogeneously over the whole sample volume, so as to ensure a single, well-defined reaction temperature of the sample – this being the equilibrium temperature between two opposing driving forces, namely the heating by the laser pulse, and the cooling by the thermal bath. To this end, a small sample volume is paramount, in order to maximize the rate of heat transfer. This is one of the reasons why the T-jump methodology developed here was coupled

to high-frequency EPR, which makes use of relatively small sample volumes. Evidence of the homogenous heating produced by the laser pulses used in the setup of T-Cycle EPR described in this thesis is given in Figure 1.2, where the 275 GHz cw EPR spectra of a solution of TEMPOL in a mixture of water and glycerol are shown as a function of the nominal laser power. To record these spectra, the laser was turned on continuously, and a spectrum was recorded for different laser powers, in increasing order. These spectra can be easily interpreted and simulated by taking into account one single spectral component (as described in the Appendix to Chapter 3), which implies they are not the summation of many different spectra that originate from zones of the sample at different temperatures. The homogenous heating of the sample produced by the laser-induced T-jumps applied here is facilitated by the small sample volume (about 20 nL), and is in agreement with what has been reported by Azarkh and Groenen in [24].

A key point to achieve fast and homogenous T-jumps is the efficient absorption of the NIR energy by the solvent molecules. Water has a broad absorption in its NIR spectrum peaking around 1450 nm, originating from the first overtone of the O—H bond stretching [25]. The absorption coefficients at 1600 nm (i.e., about the wavelength of the laser used in Chapters 3 to 5, at 1550 nm) of pure water [26], pure glycerol [27], and mixtures of water and glycerol 1:1 in volume [27] are, respectively, 7.7, 11.6, and 9.8 cm^{-1}. In particular, the mixture of water and glycerol has an absorption increased by roughly 25% as compared to that of pure water, an observation in agreement with the work by Azarkh and Groenen [24].

1.5 Electron Paramagnetic Resonance

Electron Paramagnetic Resonance (EPR) is a powerful spectroscopic technique useful for structural investigations of paramagnetic species such as organic radicals, metal ions, or defect centres in solids. Similarly to the more common Nuclear Magnetic Resonance (NMR), where radio-frequency-induced nuclear spin transitions are measured, in EPR microwave-induced transitions between electron spin energy levels are detected. Since the energy of the spin levels of an electron are very sensitively influenced by its environment, valuable information can be extracted from an EPR spectrum when the quantum mechanical energy description of the electron – its spin Hamiltonian – is known. Nowadays, alongside the traditional continuous-wave (cw) approach in EPR, more and more sophisticated microwave pulse sequences are being developed to provide ever more detailed information on the spin systems of interest. Moreover, the technical achievements in microwave technology made EPR at higher microwave frequencies feasible, making it very accessible and widespread, allowing improved spectral resolution (both in EPR and Electron Nuclear Double Resonance spectra), a better identification of certain parameters of the
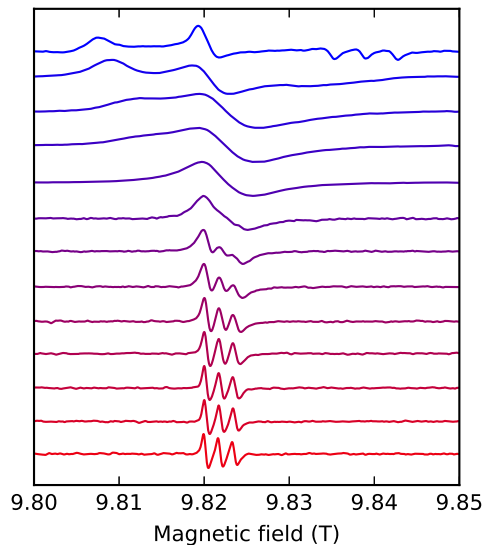
Figure 1.2: 275 GHz cw EPR spectra of TEMPOL, at a concentration of 1 mM, in solution with a mixture of water and glycerol 95:5 in volume. The spectra are recorded with the laser turned on continuously at increasing optical power (top blue @ 0.0 W, bottom red @ 2.0 W), from a cryostat temperature of -50 °C.

spin Hamiltonian (like the zero-field splitting), and a higher absolute sensitivity owing to a large Boltzmann factor [12], not to mention that in certain systems the only possibility to induce EPR transitions is with microwave quanta of high frequency. Hereinafter is a general introduction to the basic theory of EPR meant to understand the spin systems studied in this thesis. Complete treatments of the subject can be found, for instance, in [28] and [29].

1.5.1 The electron Zeeman effect and the g-factor

To illustrate the principles of EPR, the simplest paramagnetic system is considered first, namely an isolated electron having a spin $S = 1/2$. When a particle with non-zero spin is subject to an externally applied magnetic field, the energy levels associated to its spin will split as a function of the magnetic field (Equation 1.11), a phenomenon first observed by the Dutch physicist Pieter Zeeman and thus called Zeeman effect. Quantum mechanically, energy levels resulting from such effect on an electron spin can be expressed with the following spin Hamiltonian ($\mathcal{H}$):

$$\mathcal{H} = g_e \mu_B \mathbf{S} \cdot \mathbf{B} \qquad\qquad (1.11)$$

where $g_e = 2.0023$ is the g-factor of an isolated electron in the vacuum, μ_B is the Bohr magneton, $\mathbf{B}$ is the external magnetic field, and $\mathbf{S}$ is the electron spin. Since $\mathbf{B}$ is oriented along one direction (conventionally, z), only the magnetic field magnitude B_0 is taken into account, and therefore only the S_z component of the spin operator $\mathbf{S}$. In particular for the case of $S = 1/2$, the eigenvalues of S_z are $m_S = \pm\frac{1}{2}$, and the eigenvalues of the spin Hamiltonian of Equation 1.11 (namely, the energy levels of the electron spin) can be written as $E_\pm = \pm\frac{1}{2}g_e\mu_B B_0$, which evidences the dependence of the energy splitting on the external magnetic field.

The energy splitting of the spin levels is thus proportional to the magnitude of the external magnetic field, but also depends on the g-factor, a quantity that acts as a proportionality constant and is very sensitive to the magnetic environment of the electrons. In general, the g-factor is a tensorial entity, $\mathbf{g}$, and is called *anisotropic* when the diagonal components g_x, g_y, and g_z of the matrix representation in the eigenbasis of $\mathbf{g}$ are not equal. When this is the case, the splitting of the spin levels is different in different spatial directions, and the EPR transition arising from the spin Hamiltonian of Equation 1.11 will be observed at different values of the magnetic field, each one associated to a direction of $\mathbf{g}$.

To better illustrate the Zeeman effect and the influence of an anisotropic g-factor, in Figure 1.3 are plotted the spin levels of an $S = 1/2$ system with a strongly anisotropic $\mathbf{g}$ (as is the case for the system described in Chapter 5 of this thesis) as a function of the externally applied magnetic field. At zero field, the spin states are degenerate, and by increasing the magnitude of the external magnetic field, such states are split anisotropically and proportionally to g_x (red), g_y (green), or g_z (blue). When operating at 9.5 GHz (Figure 1.3 A), one of the most common frequencies in EPR, the three transitions (depicted as grey lines) associated to the three different values of $\mathbf{g}$ are observed between roughly 300 and 350 mT. In particular, the two at higher field (corresponding to g_x and g_y) are separated by about 5 mT. When going to higher magnetic field, a correspondingly higher microwave frequency is required to match the energy difference between the spin levels and induce an EPR transition. Figure 1.3 B shows such situation at the EPR frequency of 275 GHz, with the three transitions associated to the anisotropic $\mathbf{g}$ spreading between about 8700 and 9600 mT, and the two at higher field separated by about 140 mT. This simple example highlights a fundamental advantage of high-frequency (HF) EPR versus low-frequency (LF) EPR, namely a better resolution in magnetic field even for slightly anisotropic g-factors.
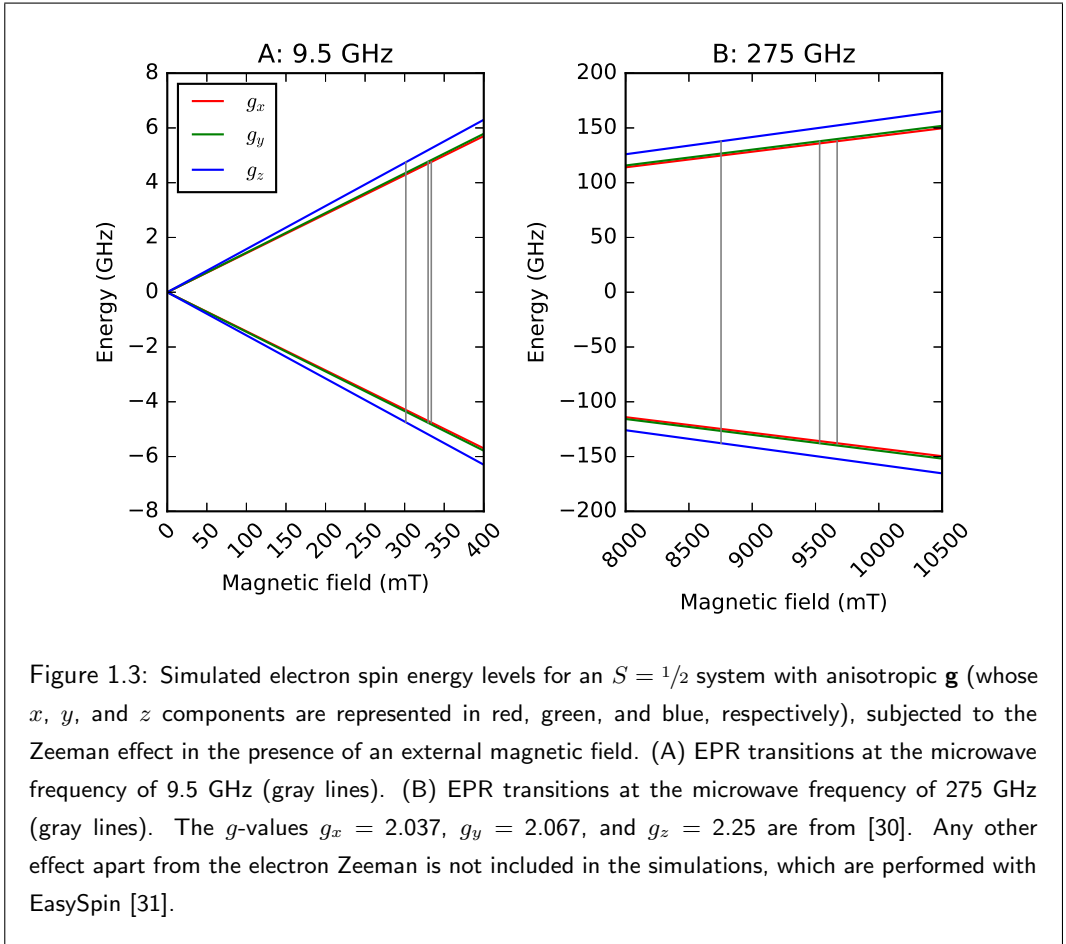
Figure 1.3: Simulated electron spin energy levels for an $S = \frac{1}{2}$ system with anisotropic **g** (whose x, y, and z components are represented in red, green, and blue, respectively), subjected to the Zeeman effect in the presence of an external magnetic field. (A) EPR transitions at the microwave frequency of 9.5 GHz (gray lines). (B) EPR transitions at the microwave frequency of 275 GHz (gray lines). The g-values $g_x = 2.037$, $g_y = 2.067$, and $g_z = 2.25$ are from [30]. Any other effect apart from the electron Zeeman is not included in the simulations, which are performed with EasySpin [31].

1.5.2 Electron spin – nuclear spin interaction: the hyperfine coupling

One of the most interesting properties of spins is their ability to interact with each other. The interaction between electron spins and nuclear spins, called hyperfine coupling, provides a great deal of information about the chemical environment of an electron. In the general case where one electron with spin $S = \frac{1}{2}$ interacts with one nucleus with spin I, the resulting spin Hamiltonian can be expressed as:

$$\mathcal{H} = g_e \mu_B \mathbf{S} \cdot \mathbf{B} - g_N \mu_N \mathbf{I} \cdot \mathbf{B} + \mathbf{S} \cdot \mathbf{A} \cdot \mathbf{I} \tag{1.12}$$

where the first term represents the electron Zeeman effect, the second term represents the nuclear Zeeman effect, and the third term represents the hyperfine interaction between the

electron spin and the nuclear spin. Like for the electron Zeeman term, also the nuclear Zeeman term contains a nuclear g-factor, g_N, and the nuclear magneton, μ_N. The hyperfine interaction is represented by the tensor **A**, which can be viewed as composed of an *isotropic* contribution and an *anisotropic* one (similarly to the **g** tensor), namely $\mathbf{A} = a_{iso} + \mathbf{T}$.

The effect of the Zeeman term on the nuclear spin is similar to that on the electron spin, namely it splits the energy levels of the nuclear spin as a function of the external magnetic field. To understand how this works, Figure 1.4 schematically illustrates the energy splitting of a system composed of one electron spin $S = \frac{1}{2}$ with isotropic g-factor, interacting with one nuclear spin $I = 1$ (such as that of ^{14}N). For simplicity, the terms of the spin Hamiltonian of Equation 1.12 are applied separately and sequentially in the scheme. When no external magnetic field is applied, all the energy levels of this $S = \frac{1}{2}$; $I = 1$ system are collapsed on one and are thus degenerate (A). Upon applying a magnetic field, the electron spin levels are subject to the Zeeman term (Figure 1.4 B) and are split according to the magnetic quantum numbers $m_S = +\frac{1}{2}$ and $m_S = -\frac{1}{2}$, customarily labeled α and β, respectively. Also the nuclear spin is subject to the Zeeman term (Figure 1.4 C), so that each of the α and β states are further split according to the magnetic quantum number of the nuclear spin, $m_I = +1$, $m_I = 0$, and $m_I = -1$. Lastly, the hyperfine coupling term applies on the aforesaid levels, shifting them by an amount defined by the hyperfine tensor **A** (Figure 1.4 D). In the scheme of Figure 1.4, only the isotropic component (a_{iso}) of the hyperfine coupling is taken into account. It can be appreciated how the single-line EPR signal arising from an isotropic g-factor and no hyperfine coupling (Figure 1.4 B, bottom) is split into $2I + 1 = 3$ equally spaced lines (the spacing in magnetic field being proportional to a_{iso}) as a result of the hyperfine interaction with the $I = 1$ nucleus of ^{14}N (Figure 1.4 D, bottom).

In real systems, it is often the case that both the hyperfine coupling *and* the g-factor are anisotropic. When the spectral resolution is not high enough, as in low-frequency EPR, it can be arduous to discern the various contributions of the **A** and **g** tensors on the EPR spectrum. At LF-EPR, such contributions might be hidden within the spectral linewidth, which is often broader than the magnitude of the hyperfine coupling itself, for instance. This can be visualized in Figure 1.5, where a spectral simulation is provided of a system such as a nitroxide radical (like TEMPOL, see Chapters 3 and 4), which features an unpaired electron with spin $S = \frac{1}{2}$ interacting with a ^{14}N nucleus with spin $I = 1$. Both the g-factor and the hyperfine coupling are anisotropic, so that each of the three components of **g** is split into $2I + 1 = 3$ lines, for a total of in principle 9 lines. However, the 9.5 GHz spectrum of Figure 1.5 A shows a rather different situation, the reason for it being that both the splitting due to the g-factor and the
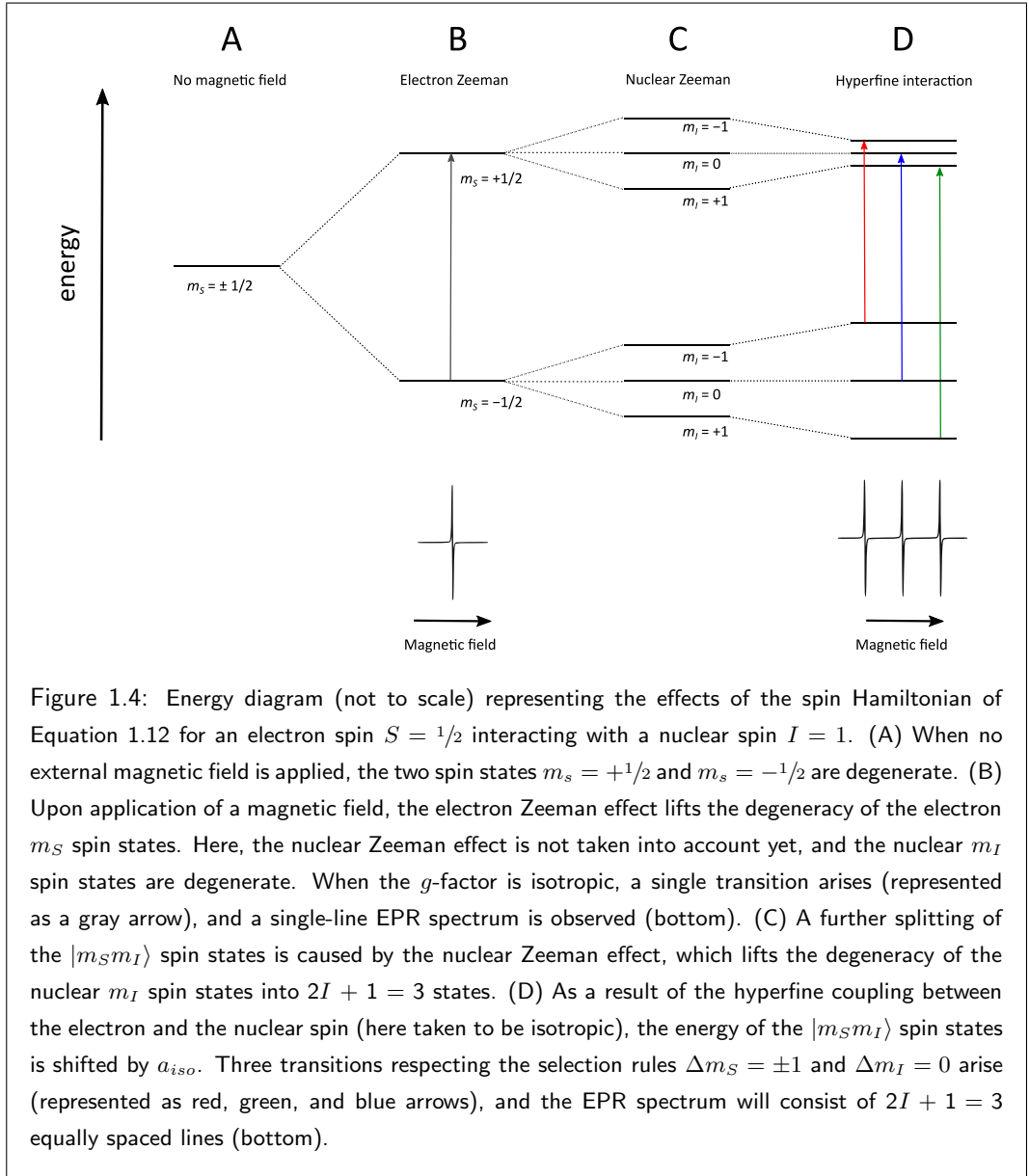
Figure 1.4: Energy diagram (not to scale) representing the effects of the spin Hamiltonian of Equation 1.12 for an electron spin $S = 1/2$ interacting with a nuclear spin $I = 1$. (A) When no external magnetic field is applied, the two spin states $m_s = +1/2$ and $m_s = -1/2$ are degenerate. (B) Upon application of a magnetic field, the electron Zeeman effect lifts the degeneracy of the electron m_S spin states. Here, the nuclear Zeeman effect is not taken into account yet, and the nuclear m_I spin states are degenerate. When the g-factor is isotropic, a single transition arises (represented as a gray arrow), and a single-line EPR spectrum is observed (bottom). (C) A further splitting of the $|m_S m_I\rangle$ spin states is caused by the nuclear Zeeman effect, which lifts the degeneracy of the nuclear m_I spin states into $2I + 1 = 3$ states. (D) As a result of the hyperfine coupling between the electron and the nuclear spin (here taken to be isotropic), the energy of the $|m_S m_I\rangle$ spin states is shifted by a_{iso}. Three transitions respecting the selection rules $\Delta m_S = \pm 1$ and $\Delta m_I = 0$ arise (represented as red, green, and blue arrows), and the EPR spectrum will consist of $2I + 1 = 3$ equally spaced lines (bottom).

splitting due to the A_x and A_y components of **A** are smaller than the spectral linewidth. The red and green dotted lines indicate the field positions of, respectively, the transitions associated to the g_x component and its A_x hyperfine component, and the transitions associated to the g_y component and its A_y hyperfine component. Only the A_z hyperfine component is large enough

to be discerned at 9.5 GHz, as shown by the peaks around 335 and 342 mT (the blue dotted line represents the field positions of such transitions). All the other transitions are hidden within the linewidth of the central peak around 339 mT, and cannot be resolved at the microwave frequency of 9.5 GHz. However, going to HF-EPR offers a much clearer picture of the system under study. In the spectrum of Figure 1.5 B, simulated for the microwave frequency of 275 GHz, the peaks associated to the three transitions arising from the anisotropic **g** are clearly recognizable. The hyperfine splitting of the A_x and A_y components is still too small as compared to the spectral linewidth; however, the A_z component is large enough to give rise to three clearly separated lines of the g_z component around 9831, 9834, and 9837 mT. This example shows the advantages of high-frequency EPR over low-frequency EPR also in determining the hyperfine components of a paramagnetic system.

1.5.3 High-spin systems

So far, only the case of a single unpaired electron with spin $S = 1/2$ has been considered. However, it is fairly common to come across paramagnetic systems with spin higher than $1/2$, such as transition metal ions (like in Chapter 2), or several electron spins ferromagnetically coupled (like in Chapter 5).

In a high-spin system such as a transition metal ion, the unpaired electrons of the d (or f) orbitals are subject to a second-order effect of the spin-orbit coupling known as zero-field splitting (ZFS), which is a term that adds to the system's spin Hamiltonian and takes the following form:

$$\mathcal{H}_{ZFS} = \mathbf{S} \cdot \mathbf{D} \cdot \mathbf{S} \tag{1.13}$$

where **D** represents the zero-field splitting tensor. The name originates from the fact that such contribution does not depend on the external magnetic field, and an energy separation between the spin levels is present even in the absence of an externally applied magnetic field, being an intrinsic property of the system.

In Chapter 2 of this thesis, the paramagnetic system under study is a d^5 Fe(III) center, which turns from a high-spin (HS) $S = 5/2$ state to a low-spin (LS) $S = 1/2$ state as a result of the replacement of its axial ligand, which induces a change in the strength of the crystal field. Figure 1.6 shows the zero-field splitting of the spin levels for HS-Fe(III). It can be noticed how, even in the absence of an external magnetic field ($B_0 = 0$), the spin levels (arranged in degenerate spin multiplicities called Kramers doublets) are split by an amount proportional to **D**. In this

Figure 1.5: Simulated cw EPR spectra at 9.5 GHz (A) and 275 GHz (B) for an electron spin $S = 1/2$ with anisotropic g-factor, with anisotropic hyperfine coupling with a ^{14}N nucleus with spin $I = 1$. The colored dotted lines represent the field positions of the transitions associated to the g_x, g_y, and g_z components (in red, green, and blue respectively). Simulations are performed with EasySpin [31], with tensors $\mathbf{g} = [2.0030, 2.0058, 2.0083]$ and $\mathbf{A} = [18, 18, 99]$ MHz set the same as for TEMPOL (see Chapters 3 and 4), and isotropic Voigtian linewidths (0.25 mT at 9.5 GHz and 0.5 mT at 275 GHz).

case, the zero-field splitting tensor is isotropic, and so large ($D = 315$ GHz [32]) that even at room temperature only the lowest Kramers doublet (corresponding to $m_S \pm 1/2$) is populated, and only transitions between the $m_S = +1/2 \longleftrightarrow m_S = -1/2$ levels can be observed.

Systems with spin higher than $1/2$ can also be the result of separate electron spins at a distance such that they can interact with each other. The electron–electron interaction consists of a classically-viewed dipolar contribution, and a quantum-mechanical *exchange* contribution:

$$\mathcal{H}_{12} = \mu_B(\mathbf{S}_1 \cdot \mathbf{g}_1 \cdot \mathbf{B} + \mathbf{S}_2 \cdot \mathbf{g}_2 \cdot \mathbf{B}) + \mathbf{S}_1 \cdot \mathbf{D}_{12} \cdot \mathbf{S}_2 - J_{12}\mathbf{S}_1 \cdot \mathbf{S}_2 \tag{1.14}$$
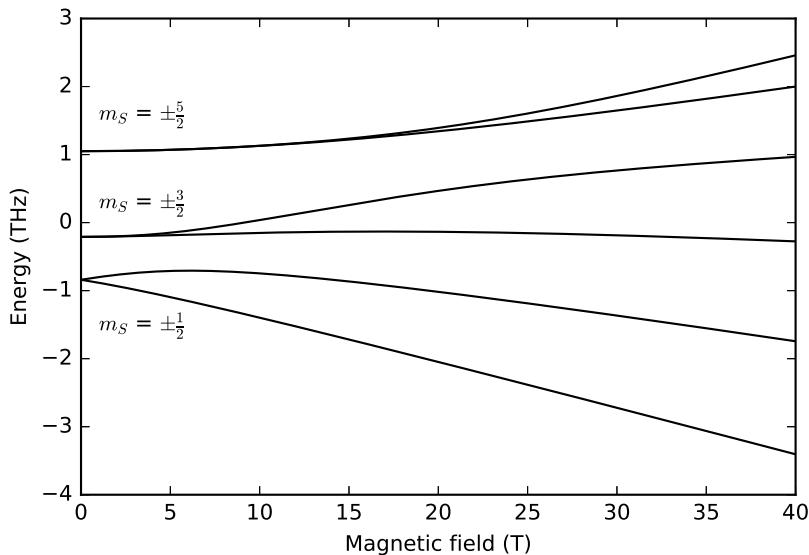
Figure 1.6: Simulated electron spin energy levels as a function of the external magnetic field for an $S = {}^5\!/_2$ system with isotropic g and isotropic $D = 315$ THz (from [32]). Simulations are performed with EasySpin [31] showing the x direction.

where, in analogy to Equation 1.11, the first term is the electron Zeeman effect, the second term is the dipolar coupling between the two electrons ($\mathbf{D}_{12}$ being the dipolar coupling tensor), and the third term is the exchange interaction between the two electrons (J_{12} being the isotropic exchange coupling). The subscripts refer to electron 1 or 2.

In Chapter 5 of this thesis, the paramagnetic intermediate of the enzyme under study is suggested to be a triplet system composed of a Cu^{2+} ion interacting with a tyrosyl radical (an organic radical), both with spin $S = {}^1\!/_2$. Figure 1.7 shows the diagram of the magnetic field dependence of the spin levels of a simplified system, namely one where the g-factor is isotropic and there is no hyperfine interaction with the spin of the copper nucleus. As a result of the interaction of two spins $S = {}^1\!/_2$, an $S = 0$ and an $S = 1$ spin multiplicity are generated (named singlet and triplet, respectively), whose energy separation is proportional to the exchange coupling J_{12}. The $m_S = 1$ state of the $S = 1$ spin multiplicity is further split from the $m_S = 0$ and $m_S = -1$ states by the dipolar coupling tensor $\mathbf{D}_{12}$ at zero field. Transitions are possible only within the $S = 1$ spin state, and not between the $S = 0$ and the $S = 1$ spin state.
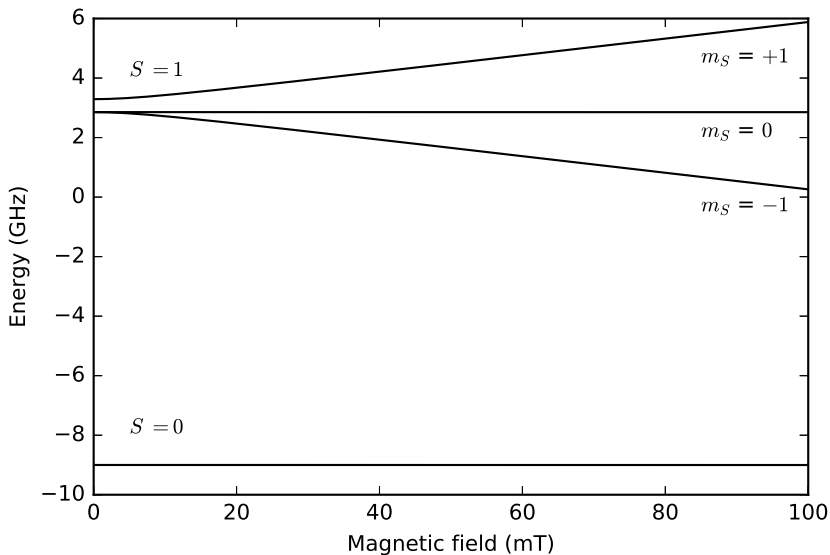
Figure 1.7: Simulated electron spin energy levels as a function of the external magnetic field for a triplet system made of two interacting $S = 1/2$ electron spins, with isotropic g, isotropic exchange coupling $J_{12} = 12$ GHz, and anisotropic $\mathbf{D}_{12} = [290, 290, -580]$ MHz (from [30]). Simulations are performed with EasySpin [31] showing the x direction.

EPR transitions are called "allowed" when they occur between spin levels with selection rule $\Delta m_S = \pm 1$. However, at LF-EPR, weaker transitions arise, called "forbidden", that deviate from the aforementioned selection rule and, in the case of a triplet state, occur between spin levels with $\Delta m_S = \pm 2$. These transitions, also called *half-field* transitions, occur when the Zeeman terms of the spin Hamiltonians of Equations 1.13 and 1.14 (which are field-dependent) are small in comparison to the ZFS or spin-spin interaction terms – in other words, when the external magnetic field is low or, equivalently, when the EPR microwave frequency is low. Under such circumstances, the spin levels are not well-defined by single magnetic quantum numbers, but rather are a mix of them. The abundance of half-field transitions at LF-EPR makes the resulting spectra extremely hard if not impossible to interpret, especially with systems with spin $S > 1$. However, the spin levels of such systems are "well-behaved" at high magnetic field, namely when the Zeeman terms are bigger than the ZFS or spin-spin interaction terms, meaning that the single spin levels can be correctly described by their magnetic quantum numbers, and no "forbidden" transitions occur. For this reason, HF-EPR is particularly suited for the study

and interpretation of high-spin systems.

1.5.4   Slow-to-fast motion and rigid limit in EPR spectra

All the EPR spectra shown thus far originate from samples in the so-called *rigid limit*, namely samples whose paramagnetic species are not free to quickly rotate in any direction – a situation proper of solids. When this is the case, the paramagnetic species in a solid matrix are bound to a specific direction, and so are their electron spins. Such a rigid system is susceptible to the orientation of the external magnetic field as compared to the orientations of its own spin-Hamiltonian parameters, and the anisotropy (when present) is observable in the EPR spectra. In particular, powders and frozen solutions (i.e., disordered glasses) can be seen as ensembles of spins ranging all possible spatial directions – as opposed to single crystals, which have all of their spins oriented in the same direction, thus giving rise to EPR spectra associated to one specific spatial orientation. When the EPR spectrum of a powder is recorded (hence also called *powder* spectrum), the spin transitions of all possible orientations are induced, and a continuous absorption is measured. In practice, however, the resulting powder spectrum does not look like a continuous absorption as a result of the field modulation employed to record the spectrum, which causes it to appear like a first-derivative spectrum. All the spectral simulations shown before correspond to powder spectra.

The complete opposite case as that of a powder spectrum is when the paramagnetic species are freely rotating in their medium, a situation that normally occurs with molecules in solutions, and that is referred to as *fast motion*. Due to the fast rotational motion (or "tumbling") of the paramagnetic species in the solution, all the anisotropic terms of the system's spin Hamiltonian average out. What is thus visible in the EPR spectrum of a paramagnetic species in a solution is the mean value of the **g** tensor and the isotropic component (a_{iso}) of the hyperfine **A** tensor. The components of the **D** tensor average to zero in the fast-motion regime and the zero-field splitting is thus not measurable.

An intermediate situation between the rigid-limit and the fast-motion regimes also exists, namely when the medium containing the electron spins still allows rotational motion of the paramagnetic species, but such motion is hindered by physical factors such as the high viscosity of the solution (which is the case for the mixtures of water and glycerol described in Chapters 3 and 4) or steric effects (such as a spin label attached to a protein). As a result of these hindrance effects, the rotational motion of the paramagnetic species is slowed down or, equivalently, their *rotational correlation time* (τ_c) becomes longer, which affects the spin relaxation processes and the spectral line shapes [33]. The time τ_c is defined as the average time in which a molecule

rotates by one radian in a certain spatial direction, and it ranges from picoseconds for the fast-motional regime, to nanoseconds up to microseconds for the slow-motional regime. There are several models to describe such slow-motion effects (like the Stokes-Einstein equation used in the Appendix to Chapter 3 of this thesis), through which valuable information on the surroundings of a spin system can be obtained, such as the temperature of a solution, or the conformation of a spin-labeled protein.

Nitroxide radicals such as TEMPOL exhibit important changes of the spectral line shape as a function of their rotational correlation time. This is shown, as an example, in Figure 1.8, where the spectral linewidth changes of solutions of TEMPOL are plotted as a function of the sample temperature (in the range between 143 K and 293 K). A different dependence of the solution's viscosity on temperature affects the spectral shapes differently, so that a solution of TEMPOL in pure water (A), and a solution of TEMPOL in a mixture of water and glycerol 1:1 in volume (B) behave very differently as a function of temperature. Since the viscosity of liquid water does not change much with temperature, the mobility of the molecules in the solution is fast and roughly constant. This can be seen in the spectra of Figure 1.8 A in the temperature range from 293 K down to 253 K, where the spectral line shape does not change much. The three-line spectrum originates from the a_{iso} component of the hyperfine interaction of the electron with the ^{14}N nucleus, as the anisotropic component is averaged to zero as a result of the fast rotational motion of the molecules in the solution. From 243 K down, the solution freezes and a powder spectrum arises, which has however an unusual shape. This is due to the fact the TEMPOL molecules, at a relatively high concentration, form clusters in the absence of glycerol in solution, becoming close enough to each other for their spins to interact intermolecularly, which results in a broadening of the line shape. Figure 1.8 B shows a rather different situation, because the viscosity of water and glycerol solutions varies greatly with temperature, affecting the rotational motion of the molecules and thus the spectral shape. A progressive spectral broadening is visible in the temperature range between 263 and 233 K, this being the range where the sample transitions from a fast-motion regime through a slow-motion regime, down to a rigid-limit regime. The plot of Figure 1.8 B highlights the importance of glycerol added to the solution, which has a "de-clustering" effect on the TEMPOL molecules. As a result, the changes in the spectral line shape of TEMPOL are easy to interpret and simulate, yielding information on the temperature of the solution (see Appendix to Chapter 3).

Figure 1.8: 9.5 GHz cw EPR spectra of solutions of TEMPOL at a concentration of 2 mM, (A) in pure water and (B) in a mixture of water and glycerol 1:1 in volume. The spectra were recorded with a Bruker Biospin EMX 080 EPR spectrometer, in the temperature range between 143 K and 293 K, controlled by a nitrogen-flow cryostat ER4131VT temperature control system (Bruker).
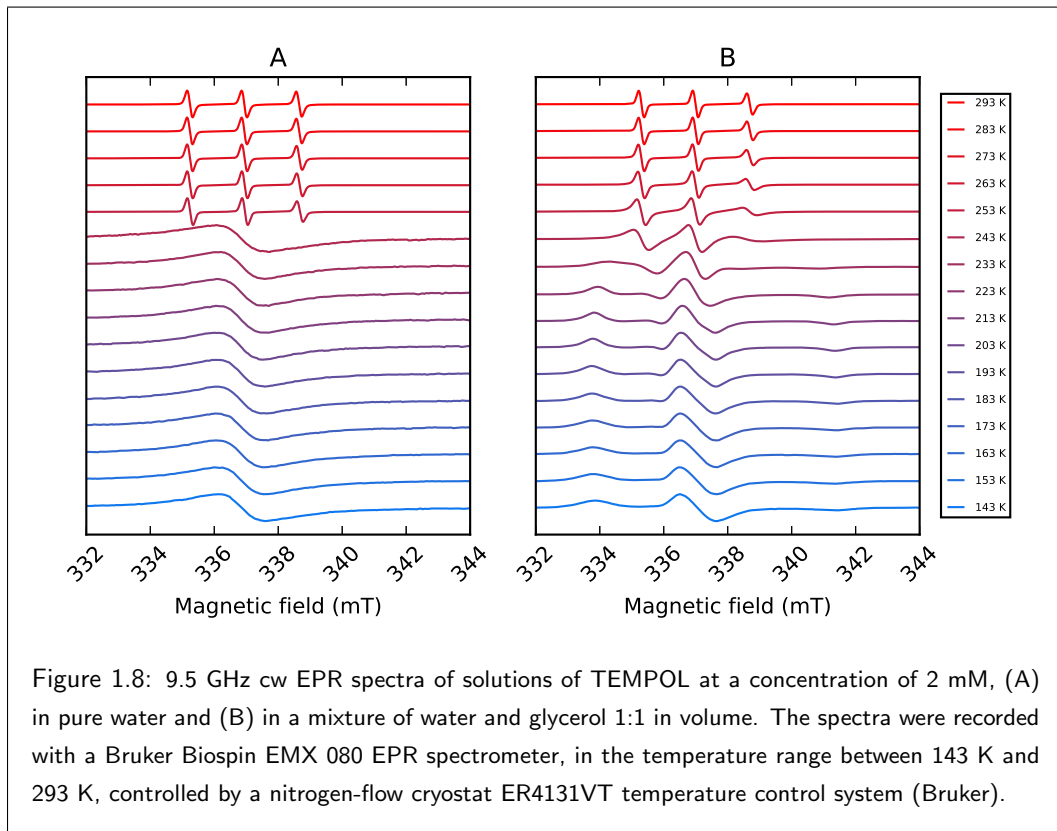
1.5.5 Home-built 275 GHz EPR spectrometer

The EPR spectra at the microwave frequency of 275 GHz described in this thesis were performed on a spectrometer built around 2000 by Blok and coworkers at Leiden University, and described in great detail by the same authors in [34]. The construction of such spectrometer was driven by ever-growing interest in HF-EPR, after spectrometers at frequencies such as 95 and 140 GHz became commercially available.

Here, a brief description of the setup is provided. A simplified block diagram of the home-built 275 GHz EPR spectrometer is shown in Figure 1.9, and consists of four main parts:

(A) Two microwave sources, producing two microwave beams at the frequencies of 91.9 GHz and of 89.7 GHz, which are sent to diode triplers that return the frequencies of 275.7 GHz and 269.1 GHz. The former is the frequency used to excite the sample, while the latter serves as the local oscillator for the superheterodyne receiver.

(B) A microwave bridge operating in reflection mode, suitable for both cw and pulsed experiments. It transmits the incoming microwave frequencies to and from the resonant cavity with a quasi-optical transmission setup, which allows the confined beams of electromagnetic waves to travel in free space, thus making the transmission losses negligible – as opposed to conventional waveguide technologies at such high frequencies.

(C) A single-mode, tunable resonant cavity which is located at the bottom of a variable-temperature helium-gas flow cryostat placed at the center of a superconducting magnet. The cavity is coupled to the microwave bridge through a corrugated circular waveguide whose geometry maximizes the microwave coupling and minimizes the transmission losses. The cavity has an absolute sensitivity as high as 10^8 spins per mT. The cylindrical cavity has a diameter of 1.4 mm and a length between 0.8 and 1.4 mm that can be varied with two plungers located at both sides, which move synchronously and symmetrically inward and outward so as to allow the tuning of the cavity. Underneath the cavity is a coil that generates the field modulation for cw experiments, and a grid that allows irradiation of the sample from an external source.

(D) A superconducting solenoid magnet capable to reaching 14 T. The scan-to-scan field stability is less than 0.1 mT, while the day-to-day field stability is less than 1 mT.

The microwave beam reflected from the resonant cavity, carrying the EPR signal, is transmitted through the corrugated waveguide back to the bridge, where it reaches a Martin-Puplett diplexer, which combines the EPR signal at 275.7 GHz with the local oscillator at 269.1 GHz, giving both the same well-defined polarization. The coupled output signal is then directed to a polarization-sensitive microwave mixer where a signal is produced at the so-called intermediate frequency (IF) of $275.7 - 269.1 = 6.6$ GHz. The IF signal is finally amplified and fed to a lock-in detector for cw experiments, or a boxcar integrator for pulsed experiments.
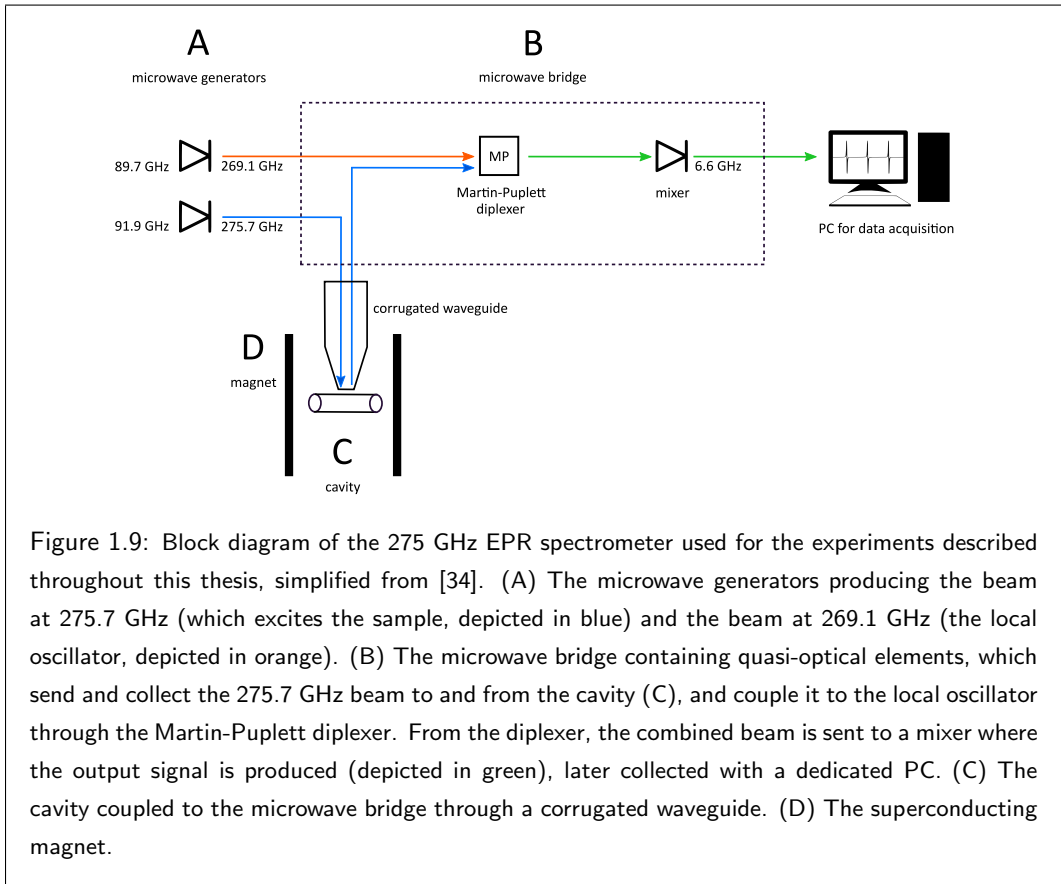
Figure 1.9: Block diagram of the 275 GHz EPR spectrometer used for the experiments described throughout this thesis, simplified from [34]. (A) The microwave generators producing the beam at 275.7 GHz (which excites the sample, depicted in blue) and the beam at 269.1 GHz (the local oscillator, depicted in orange). (B) The microwave bridge containing quasi-optical elements, which send and collect the 275.7 GHz beam to and from the cavity (C), and couple it to the local oscillator through the Martin-Puplett diplexer. From the diplexer, the combined beam is sent to a mixer where the output signal is produced (depicted in green), later collected with a dedicated PC. (C) The cavity coupled to the microwave bridge through a corrugated waveguide. (D) The superconducting magnet.

2

Effective coupling of Rapid Freeze-Quench to High-Frequency Electron Paramagnetic Resonance

2.1 Introduction

Determination of reaction rates and detection of short-lived intermediates of fast chemical reactions are an important goal in those fields that involve molecular chemistry, such as biochemistry, pharmaceutics, medicine, environmental science, and material science, to name a few. Kinetics and intermediates shed light on the mechanism of a reaction, which in turn yields broader information about the chemical system under study.

One possible stratagem to investigate chemical kinetics is that of letting the reaction unfold for controlled time steps and then "freezing" it. In this way it is possible to follow the decay and growth of reactants and products, or the evolution of reaction intermediates. One of the most widely used techniques to attain this is called *Rapid Freeze-Quench* (RFQ), in use since 1961 [18], which is often coupled to Electron Paramagnetic Resonance (EPR) in view of the paramagnetic nature of the intermediates of a great deal of chemical reactions.

The multi-frequency approach in EPR is of particular interest, namely when low-frequency experiments (e.g. those at the standard frequency of 9.5 GHz, called X-band) are combined with high-frequency ones (HF-EPR, e.g. those at microwave frequencies of 95 and 275 GHz). Such approach offers a better and more complete characterization of the magnetic system under study. However, collection of RFQ samples is – to say the least – problematic for applications in HF-EPR, because the size of HF resonant cavities is hugely reduced as compared to the standard 9.5 GHz EPR, thus making the sample holders and the sample volume dramatically small. In Table 2.1 is shown a comparison of the typical sample volumes used for three EPR frequencies, namely 9.5, 95, and 275 GHz. The sample volume downsizes by about 10^4 times going from low to high frequency. It is therefore vital to develop a sample packing technique that guarantees an efficient, homogeneous, and reproducible sample collection in the small capillaries used as sample holders for HF-EPR.

Frequency (GHz)	Cavity length (mm)	Effective sample volume
9.5	30	100 μL
95	4	1 μL
275	1	20 nL

Table 2.1: Comparison of the sample volumes involved in some EPR frequencies.

In the literature there have been endeavors to implement and standardize packing techniques for RFQ-EPR applications [35] [36] [37] [38] [39] [40] [21].

Ballou et al. [35] and Oellerich et al. [36] are the earliest reported attempts to study a chemical reaction detected with X-band EPR on a timescale of less than 80 ms. Although of great interest given the short timescale, both authors attribute the large inaccuracy on the reaction rates (errors bigger than 10%) to the nonuniform and irreproducible packing of the RFQ particles. Indeed, in both papers the authors report a rather low and nonhomogeneous packing efficiency, between $0.5 \div 0.7$ the former, and between $0.4 \div 0.6$ the latter. Oellerich even concludes that this problem constitutes an "intrinsic deficiency of freeze-quench EPR spectroscopy", and indeed, as described below, this is a serious issue not easily circumvented.

Nami et al. [37] propose an improved method to collect and pack RFQ particles from an isopentane suspension, based on pumping said suspension through an EPR tube in which a filter has been placed. The RFQ particles are trapped at the filter and the isopentane is easily removed. The advantages of this method are its reproducibility and efficiency: the authors report a packing factor between $0.68 \div 0.76$, which is indeed a considerable improvement, also compared to previous studies (see below). A slightly modified version of this method is applied in this work.

Schuenemann et al. [38] are the first to report the application of RFQ to HF-EPR in a multi-frequency EPR study (at 9.6, 94, 190, and 285 GHz), on a timescale of up to 40 ms. Although HF-EPR implies dealing with sample holders of reduced size, the method used by the authors to pack the RFQ for HF-EPR is basically the same as for low frequency, i.e., compacting the sample sprayed in a tube of the appropriate size by means of a metal rod. However, the authors' focus is to detect the reaction intermediate of the reaction under study, rather than its reaction rate, so that inhomogeneous sample packing is of no concern to them.

In the context of RFQ-HFEPR, Manzerova et al. [39] bring about an innovative method to freeze-quench reactants, reduce them to fine particles, and collect them. They report a technology based on rotating copper wheels kept at a temperature of 80 K, on which the mixture of the reactants is sprayed through a home-built nozzle. The reactant mixture is thus freeze-quenched, and the sample is then "scraped" off the wheels and collected by tapping with a capillary suitable for 130 GHz EPR. Although such approach introduces the advantage of not having to handle static frozen particles floating in isopentane, the packing factor the authors report is 0.5, thus being no improvement as compared to those from the aforementioned studies.

All of the aforesaid publications require a large amount of sample, which is often a disadvantage when working with biological samples. Kaufmann et al. [40] and Pievo et al. [21] reported the development of, respectively, a micro-fluidic mixer (after its introduction by Cherepanov and de Vries [20]) and a micro-mixer, both requiring volumes of hundreds of microliters, thus suitable

for RFQ-HFEPR studies of biological samples. It is interesting that Kaufmann also implemented a new way of collecting the RFQ samples, based on the idea of Manzerova [39]: they use a rotating aluminum plate kept at a temperature of 80 K, on which the reagent mixture is sprayed and freeze-quenched. The RFQ powder is then collected by tapping the capillary on it. However, the packing efficiency is not mentioned, while in [21] a packing factor of 0.5 ÷ 0.6 is reported. From the cited literature thus emerges a serious difficulty in RFQ-HFEPR when it comes to collect RFQ particles and study them in a standardized, efficient, and reproducible way.

In the literature, a common and practical way of testing the performance of RFQ-HFEPR is making use of the binding reaction of sodium azide to myoglobin. This reaction (Scheme 2.1) is a well-understood model system that offers several advantages in EPR studies because of its convenient spectral properties [35] [36] [21].

$$[\text{Fe}^{3+}_{HS}\text{—OH}_2] + \text{N}_3^- \rightarrow [\text{Fe}^{3+}_{LS}\text{—N}_3^-] + \text{H}_2\text{O} \tag{2.1}$$
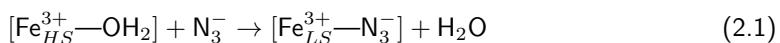
Myoglobin (abbreviated Mb) is an iron- and oxygen-binding hemoprotein, similar to hemoglobin, whose function is that of reversibly storing and transporting oxygen in the muscle tissues of many vertebrates [41]. At neutral pH, the heme iron (Fe(III), a d^5 ion) of ferric myoglobin (also known as *met-myoglobin*) exhibits an octahedral coordination environment with one of the axial positions being occupied by variable ligands. The nature of such variable ligands determines the energy splitting between the upper and lower groups of d orbitals. Water can be one of these ligands, and weakly binding to the heme-Fe(III), thus generating a high-spin (HS) $S = {}^5/_2$ state. However, when an exogenous strong-binding ligand such as azide (N_3^-) replaces the axial water molecule, the stronger ligand-field effect induced on Fe(III) converts its spin state to low-spin (LS) with $S = {}^1/_2$. Scheme 2.1 illustrates the binding reaction of azide to myoglobin.
The spectral features of HS- and LS-Fe(III) are completely different, the former having an intense signal around $g = 6$, while the latter having a rhombic signal around $g = 2$. Such features turn out to be so handy that the binding reaction of sodium azide to myoglobin has become a standard when evaluating RFQ-EPR methods, both at low and high frequency [35] [36] [39] [21].

The present work originates from the premises cast by Nami in her PhD thesis [42], who explored the feasibility of multi-frequency EPR coupled with RFQ making use of the binding reaction of sodium azide to met-myoglobin, based on an improved method to pack and load capillaries for HF-EPR [37]. However, her investigations at high-frequency EPR (95 and 275 GHz) yielded unconvincing results, given the huge scatter of the data points. The two main limitations that can be envisaged in [42] are:

- The reaction time scale selected for the study was very short, namely less than 10 ms for a reaction with a characteristic time twice as long;

- The manganese(II) ions introduced in the RFQ samples, used for internal calibration, were originally mixed in the sodium azide solution, rather than in the myoglobin solution. In this way, the $^{Mb}/_{Mn^{2+}}$ ratio is affected by possible irreproducible mixing of the RFQ apparatus, which results in an inconstant ratio for different RFQ samples.

For these two reasons, in this work it was chosen to select a longer time scale for the myoglobin reaction of Scheme 2.1 (namely, up to $\sim$ 50 ms), and to add $MnCl_2$ to the myoglobin solution, rather than to the sodium azide solution, prior to mixing in the RFQ apparatus.

Another critical aspect of this study is the packing of the RFQ samples in the sample holders suitable for 275 GHz EPR, namely quartz capillaries with an inner diameter of 150 μm, hosting a sample volume of 20 nL in the resonant cavity. While the general procedure to prepare the X-band RFQ samples is the same as described in [42], an improved method for sample preparation for 275 GHz was devised.

2.2 Experimental

2.2.1 Materials

Equine-heart met-myoglobin, sodium azide (NaN_3), and DMSO were purchased from Sigma-Aldrich (cat. n. M1882-1G, 15,795-3, and 154938-1L respectively). $MnCl_2$ was purchased from Baker Chemicals (cat. n. 0173). Myoglobin was dissolved in phosphate buffer 100 mM at pH 7.8, with the addition of 5% v/v DMSO and 50 μM of $MnCl_2$, to form a solution with concentration 2.4 mM. Sodium azide was dissolved in phosphate buffer 100 mM at pH 7.8 to form a solution with concentration 24 mM. After RFQ mixing, the Mb:azide ratio is 1.2:12 mM. The concentration of the myoglobin solution was determined spectrophotometrically using the extinction coefficient $\epsilon_{505} = 9.7$ mM^{-1} cm^{-1}.

2.2.2 Sample preparation

Ten RFQ samples (named Mb1 to Mb10) were prepared with the same RFQ apparatus and method described in [37] (2-mL syringes, ram velocity 3.2 cm s^{-1}, displacement 3 mm), at a mixing temperature of 21.5 °C, and at reaction times ranging between 2 and $\sim$ 50 ms. These

ten samples were initially measured at 9.5 GHz, and later (about a year after), the same were used for measurements at 275 GHz.

Table 2.2 summarizes, for each RFQ sample, the corresponding reaction time, that is calculated from the parameters used in the RFQ setup, and not corrected by the so-called *freezing time*.

RFQ sample label	Mb1	Mb2	Mb3	Mb4	Mb5	Mb6	Mb7	Mb8	Mb9	Mb10
Calculated reaction time (ms)	2.0	3.1	4.9	7.8	9.8	15.6	25.0	31.3	39.1	48.8

Table 2.2: Calculated reaction time of the RFQ samples.

In addition, two myoglobin solutions without any sodium azide were prepared (labeled Mb0), meant to represent reaction 2.1 before it has started, namely at $t = 0$. For the spectra at 9.5 GHz, the Mb0 solution was prepared from the same batch used to prepare the RFQ samples. However, for the spectra at 275 GHz, since about a year passed from the preparation of the RFQ samples, the Mb0 solution was made from an independent batch, but with identical composition as described in Subsection 2.2.1.

Sample packing for 9.5 GHz EPR

The preparation of RFQ samples for 9.5 GHz EPR is a procedure that was successfully standardized by Nami [37]. With this procedure, the RFQ samples are straightforwardly packed in quartz tubes, readily used as sample holders for 9.5 GHz EPR. The essential steps of this procedure, conducted in a polystyrene box filled with dry ice pellets, are briefly reported below:

- The quartz tubes (10 cm long, 3 mm inner diameter) are open on both sides, and are customized by tapering them on one side. This allows the accommodation of a polypropylene disk used as a filter.

- The tapered end is connected through a latex tubing to a hand-held 60-mL Norm-Jet disposable syringe used to create underpressure (instead of a water aspirator, as described in the original procedure).

- While manually creating underpressure in the syringe, the other side of the quartz tube is dipped in cold isopentane contained in a vial in contact with dry ice. The isopentane is thus aspirated through the tube, which is pre-cooled by it.

- By maintaining the underpressure in the syringe, the pre-cooled quartz tube is quickly transferred into the vial containing the RFQ sample in cold isopentane. This vial has previously been lain on dry ice to ensure thermal contact. By pushing the quartz tube to the end of the sample vial (and making sure that the filter-containing tapered part is always in contact with dry ice so as to prevent the sample from warming), the RFQ sample is sucked up the tube and accumulates through it thanks to the filter. With the settings of the RFQ apparatus described above, a 3-mm quartz tube is typically filled with roughly 4 to 5 cm of sample.

- When all the isopentane contained in the sample vial has been aspirated, the latex tubing is cut and the quartz tube is stored in liquid nitrogen. As opposed to the procedure described in [42], the sample in the tube is not further packed more tightly with a steel rod because of the relatively big amount of sample present in the tube, and because a tighter packing would result in a more difficult handling for applications at 275 GHz (see 2.2.2).

The quartz tubes prepared in this way are ready to be measured with a 9.5 GHz EPR spectrometer, and do not need further treatments.

Sample packing for 275 GHz EPR

The preparation of RFQ samples for 275 GHz EPR is by far more complicated than for 9.5 GHz EPR. The minuscule size of the capillaries used as sample holders (150 μm inner diameter) poses a twofold problem. Firstly, accidental warming of the samples is easy and fast, in view of the tiny volumes involved. For this reason, since the warming of the samples has to be avoided at all costs, they have to be handled at cryogenic temperatures. This leads to the second issue, which is the difficulty of handling such small capillaries in a cryogenic atmosphere, while wearing cryoprotective gloves that reduce the user's hand sensibility.

A successful sample packing in capillaries for 275 GHz EPR is thus a troublesome procedure that requires a trained operator. Following is a description of the basic steps of this procedure (as reported in essence in [42]), which is carried out in a polystyrene box half-filled with liquid nitrogen. Thanks to a flow of cold nitrogen gas blowing on the surface of the liquid nitrogen, the average temperature in the box within the first 10 cm from the liquid nitrogen surface is kept below -100 °C.

- A home-built stainless-steel plate (15 × 15 cm) is placed on top of an octagonal polystyrene box (14 × 14 × 6 cm). The plate has a central hole (6 cm diameter) that accommodates an agate mortar (whose surface sits at the same height as the plate), tightened with screws. This mortar is used to grind the RFQ samples under liquid nitrogen. The plate
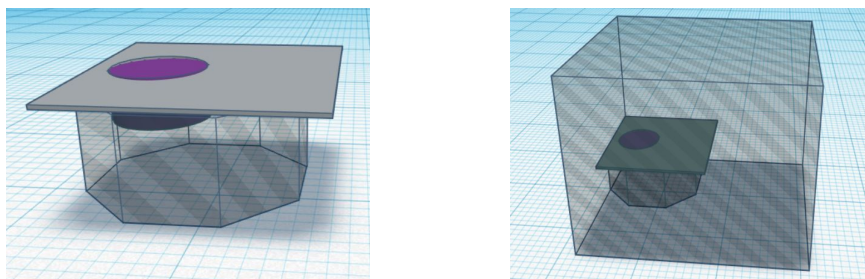
Figure 2.1: 3D renderings of the tools used for the packing procedure for 275 GHz EPR. Left: octagonal polystyrene box with metal plate and agate mortar on top. Right: bigger polystyrene box to be filled with liquid nitrogen. (This rendering does not show the grid-like array of holes perforated on the metal plate.)

also features a grid-like array of perforated holes (2 mm diameter, separated by 1 cm), which allow a better thermal exchange with the liquid nitrogen beneath once the box is filled.

- The ensemble of plate, mortar, and octagonal box (Figure 2.1, left) is placed in another, larger polystyrene box (29 × 25 × 24 cm), which is then filled with liquid nitrogen up to the level of the plate surface (Figure 2.1, right). In this way, also the octagonal box will fill with liquid nitrogen, and so will the mortar, which will always be immersed in it. It is important, prior to pouring the nitrogen, to wet the outside bottom of the octagonal box, so that a film of ice will form that keeps the octagonal box steady in its position during the procedure.

- A RFQ sample contained in a quartz tube (as described in 2.2.2) is transferred from liquid nitrogen into dry ice pellets for a few minutes to ensure the softening of the content upon reaching a relatively higher temperature. In this way, after quickly transferring the quartz tube onto the plate contained in the liquid nitrogen box, it is possible to collect the RFQ sample in the form of pellets by tapping the surface with a pre-cooled glass capillary (2 mm outer diameter). This pellet of sample is then dropped in the mortar filled with liquid nitrogen with the help of another, smaller pre-cooled glass capillary (1.1 mm outer diameter) pushed through the first one. Two to four pellets are the necessary amount of sample to be ground and packed in a capillary for 275 GHz EPR.

- The pellets of sample are ground to a fine powder in the mortar filled with liquid nitrogen,
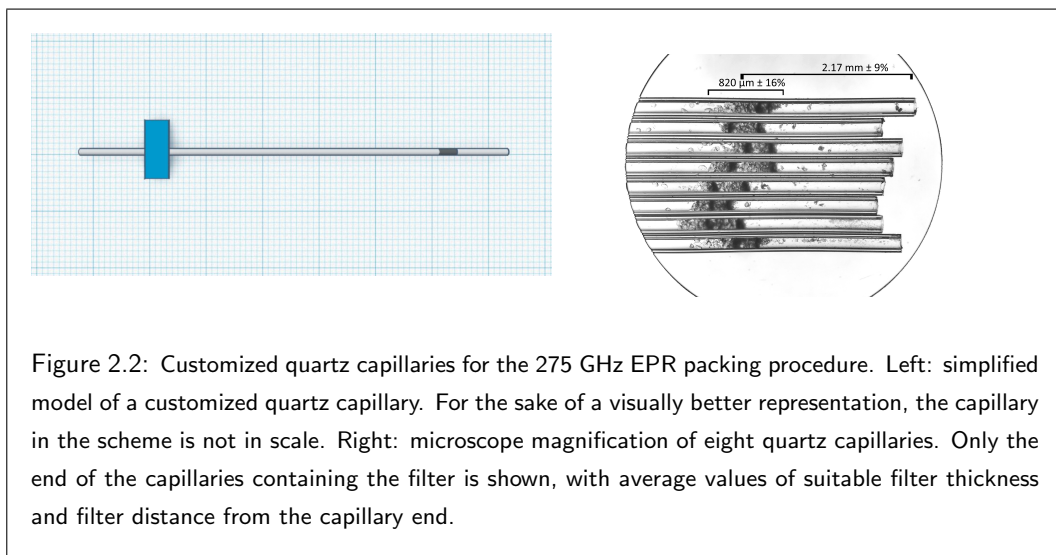
Figure 2.2: Customized quartz capillaries for the 275 GHz EPR packing procedure. Left: simplified model of a customized quartz capillary. For the sake of a visually better representation, the capillary in the scheme is not in scale. Right: microscope magnification of eight quartz capillaries. Only the end of the capillaries containing the filter is shown, with average values of suitable filter thickness and filter distance from the capillary end.

by means of a pre-cooled agate pestle. Since the ground sample has the tendency to stick onto the surface of the mortar, it is important to scoop it with a pre-cooled metal spatula so as to stir it around and facilitate the packing procedure.

- A customized quartz capillary of 150 μm inner diameter is used to collect the sample (Figure 2.2, left). Note that the customized capillary has a small tape flag that ensures the filter (and therefore the sample) to sit at a fixed position in the capillary, so that the sample will result in the middle of the insert's resonant cavity. Also, it can be noticed that the capillary has an extra portion of it beyond the flag. This portion allows the capillary to be connected - through a plastic tubing - to a 60-mL Norm-Jet disposable syringe with a straight-cut Luer needle, used to manually create underpressure over the capillary and aspirate the powdered sample.

- Once the capillary is connected to the syringe, the underpressure made, and the capillary pre-cooled, the latter is dipped into the mortar, and by manually keeping the syringe piston tight, the sample is sucked up the capillary till the silica gel filter, where it accumulates. This is a critical step, because if the filter does not have specific value ranges of thickness and distance from the capillary bottom (Figure 2.2, right), the powdered sample will accumulate only at the tip of the capillary and get stuck there. This results in a gradual decrease of the underpressure, and further packing is made impossible.

- When at least 5 mm of the capillary have been filled with sample, the capillary is placed
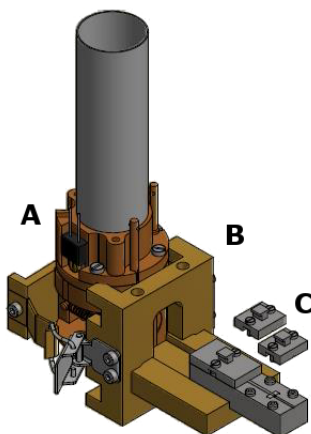
Figure 2.3: 3D rendering of the home-built probe head used for 275 GHz EPR (A), the loading stage clamped to the probe head (B), and the metal block with its three lids used to keep the sample cold (C).

on a pre-cooled home-built metal block (Figure 2.3, C), whose function is that of helping keep the capillary at low temperature, protecting it from accidental warming. The extra portion of capillary connected to the syringe is cut, and the metal block is closed with its own lids, which are then fixed with screws. The metal block is then put in dry ice, and is ready for the loading. At least two to three capillaries are prepared per sample, because their accidental breaking or exposure to room temperature is easy during handling and loading.

Sample loading for 275 GHz EPR

As opposed to the straightforward sample loading for 9.5 GHz EPR, at 275 GHz special care and equipment is needed for the reasons exposed in 2.2.2.

Ensuring that the sample stays at cryogenic temperature during the whole loading procedure is paramount. To this end, at the moment of the sample loading the spectrometer probe head has to be pre-cooled to a temperature between -90 and -80 °C (i.e., about the temperature of dry ice). With the help of a loading stage that can be clamped to the probe head (Figure 2.3, B), a capillary can be transferred from the metal block where it is accommodated (Figure 2.3, C) into the probe head. Also the loading stage is pre-cooled to dry-ice temperature, and the loading procedure is carried out under a flow of cold nitrogen gas that prevents excessive warming of the

components and of the sample, and prevents from excessive water condensation from air.

Once the loading stage is clamped onto the probe head and the metal block is correctly positioned on the loading stage, the transfer of the capillary is done by lifting up the block's lid that lies farthest away from the probe head entrance (i.e., the region of the capillary where the RFQ sample sits), and simply pushing the capillary towards the probe head. This action is repeated two more times, i.e., until the last lid (the one lying closest to the probe head) has been lifted, and the whole capillary is located inside the probe head. Afterwards, the probe head can be put back into the cryostat and taken to the desired temperature.

In this way the sample is never exposed to warm air, and stays at cryogenic temperature from the beginning to the end of the loading procedure.

2.2.3   EPR measurements

EPR measurements were performed with a 9.5 GHz (X-band) and a 275 GHz spectrometer. The former is an ELEXSYS E680 X-band (9.5 GHz) spectrometer from Bruker BioSpin GmbH, equipped with a He-flow ESR900 cryostat from Oxford Instruments. The latter is a home-built spectrometer [34], equipped with a He-flow CF935 cryostat from Oxford Instruments, and a home-built probe head with a single-mode cavity specifically designed for cw measurements [43]. The 275 GHz EPR spectrometer operates with a 14–Tesla superconducting magnet having a IPS120-10 power supply, both from Oxford Instruments, which allow a precision on the magnetic field of less than 0.01 mT.

The experimental parameters used to record the EPR spectra of the RFQ samples are summarized in Table 2.3. The X-band spectra were recorded averaging 4 scans at a temperature of 20 K, and within a field range of less than 500 mT it is possible to detect both the HS-Fe(III) (low field), and the LS-Fe(III) (high field). The 275 GHz spectra were recorded averaging between 16 to 36 scans (depending on the sample) at a temperature of 10 K, and, given the high magnetic field required to operate at such high frequency, it is not convenient to record both the low-field HS-Fe(III) signal and the high-field Mn^{2+} one in one single spectrum. Whenever shown, error bars represent the noise level of the averaged spectra.

2.2.4   Internal calibration

RFQ samples are inherently heterogeneous because of both the quality of the mixing, and the amount and density of the packed particles in the collection tubes. In order to achieve quantitative results it is therefore pivotal to device a way to calibrate the EPR signals resulting from such samples. For low-frequency 9.5 GHz EPR (X-band), this is readily attained, because both the

EPR freq. (GHz)	Field range (mT)	# of points	Mod. freq. (kHz)	Mod. ampl. (mT)	Time const. (s)	Conversion time (ms)	Microwave power (μW)	T (K)
9.5	2.5 ÷ 447.5	4096	100	0.5	0.08	40.96	100	20
275 (Mb part)	3100 ÷ 4000	1000	1.7	1.3	3	250	1.74	10
275 (Mn part)	9810 ÷ 9885	1000	1.7	0.3	1	500	0.83	10

Table 2.3: Experimental parameters of the spectra at 9.5 GHz and 275 GHz. *Mod. freq.* and *Mod. ampl.* are the field modulation frequency and amplitude, respectively.

low-field HS-Fe(III) and the high-field LS-Fe(III) are detectable, and the total intensity of the heme-Fe(III) is distributed between these two forms [21]. However, since at high-frequency 275 GHz EPR only the low-field HS-Fe(III) is visible, a reference signal is needed to normalize the Fe(III) signal. This is achieved by addition of $MnCl_2$ to the myoglobin solution [44], prior to the mixing in the RFQ apparatus. The Mn^{2+} ion exhibits intense, sharp peaks around $g = 2$, a feature that makes it ideal for use as an internal standard.

2.2.5 Methodology

The myoglobin-to-azide ratio of 1:10 allows to treat reaction 2.1 as a pseudo-first-order kinetics [42], so that the logarithmic ratio of the concentration of the HS-Fe(III) at any reaction time t and at time $t = 0$ (from now on, $[HS]_t$ and $[HS]_0$, respectively) is proportional to the reaction time (Equation 2.2). The k' is called the *apparent* reaction rate, and is the product of the actual reaction rate and the azide concentration, $[N_3^-]$ (Equation 2.3).

$$\ln \frac{[HS]_t}{[HS]_0} = -k' \cdot t \tag{2.2}$$

$$k' = k \cdot [N_3^-] \tag{2.3}$$

At high-frequency EPR (275 GHz), the ratio of the HS-Fe(III) concentrations, $[HS]_t/[HS]_0$ (from now on defined as $Y(t)$), is directly proportional to the ratio of the EPR intensity of the respective signals normalized by the Mn^{2+} signal, $(S'_{HS})_t/(S'_{HS})_0$, as shown in Equation 2.4. Note that S' represents the signal S *normalized* by manganese (Equation 2.5).

$$Y(t) = \frac{[HS]_t}{[HS]_0} = \frac{(S'_{HS})_t}{(S'_{HS})_0} \tag{2.4}$$

$$(S'_{HS})_t = \frac{(S_{HS})_t}{S_{Mn}} \tag{2.5}$$

At 9.5 GHz, the detection of Mn^{2+} is problematic, so that the normalization of the HS-Fe(III) signal is done with the LS-Fe(III) one (S_{LS}). Pievo *et al.* [21] showed that in this case $Y(t)$ can be written as:

$$Y(t) = \frac{R_t}{R_t + \lambda} \tag{2.6}$$

$$R_t = \frac{(S_{HS})_t}{(S_{LS})_t} \tag{2.7}$$

$$\lambda = \frac{(S_{HS})_0}{(S_{LS})_\infty} \tag{2.8}$$

where the λ factor in Equation 2.6 is the ratio of the HS-Fe(III) signal at $t = 0$, $(S_{HS})_0$, (i.e., reaction not begun yet), and the LS-Fe(III) signal at $t \rightarrow \infty$, $(S_{LS})_\infty$, (i.e., reaction completed), as expressed in Equation 2.8. R_t is the ratio of the HS- and LS-Fe(III) at the time t.

Both at 9.5 GHz and at 275 GHz, the signals S used in Equations 2.2 to 2.8 were the peak-to-peak intensities of the spectra of Figure 2.4 (at 9.5 GHz) and Figure 2.7 (at 275 GHz), measured at appropriate field values.

2.3 Results

The X-band spectra of the ten myoglobin-azide RFQ samples in the time range between 2.0 and 48.8 ms show a clear decay of the low-field HS-Fe(III) signal at $B_0 = 115.3$ mT, accompanied by a proportional increase of the rhombic high-field LS-Fe(III) one at $B_0 = 241.9$, 304.8, and 391.9 mT (Figure 2.4). It can be noticed that already in the Mb1 sample at $t = 2.0$ ms the LS-Fe(III) is detectable, while in the Mb10 sample at $t = 48.8$ ms the HS-Fe(III) signal has not completely disappeared, indicating that the reaction is not completed yet.

Figure 2.5 (top) shows the signal decay $Y(t)$ obtained from the X-band spectra, versus the calculated reaction time (see Table 2.2). The HS signal intensity was taken at $B_0 = 112.7$ mT (max) and $B_0 = 117.2$ mT (min), while the LS signal intensity was taken from the central component of the rhombic spectrum at $B_0 = 304.0$ mT (max) and $B_0 = 306.3$ mT (min). Spectra of RFQ samples Mb5, Mb6, Mb8, and, to a lesser extent, Mb10, show a broadened signal in the range B_0 between 150 and 250 mT, clearly due to a contamination most likely during the preparation of the RFQ samples. However, this contamination does not prevent an accurate determination of the intensity of the signals of interest, since they fall outside of the
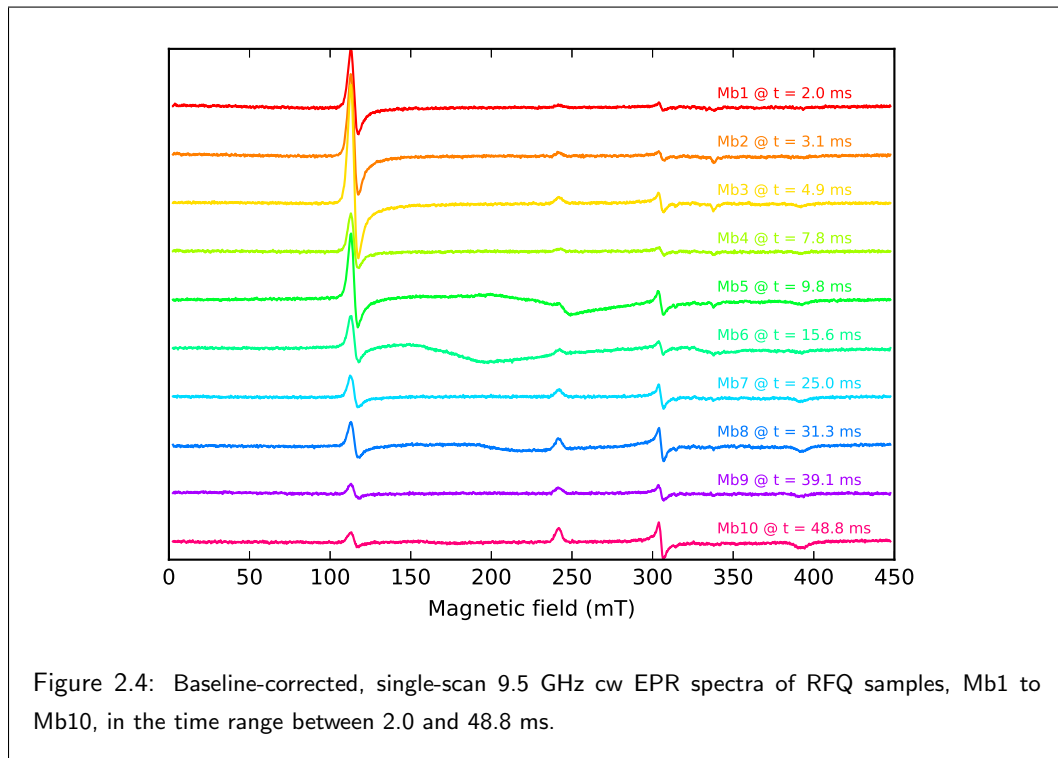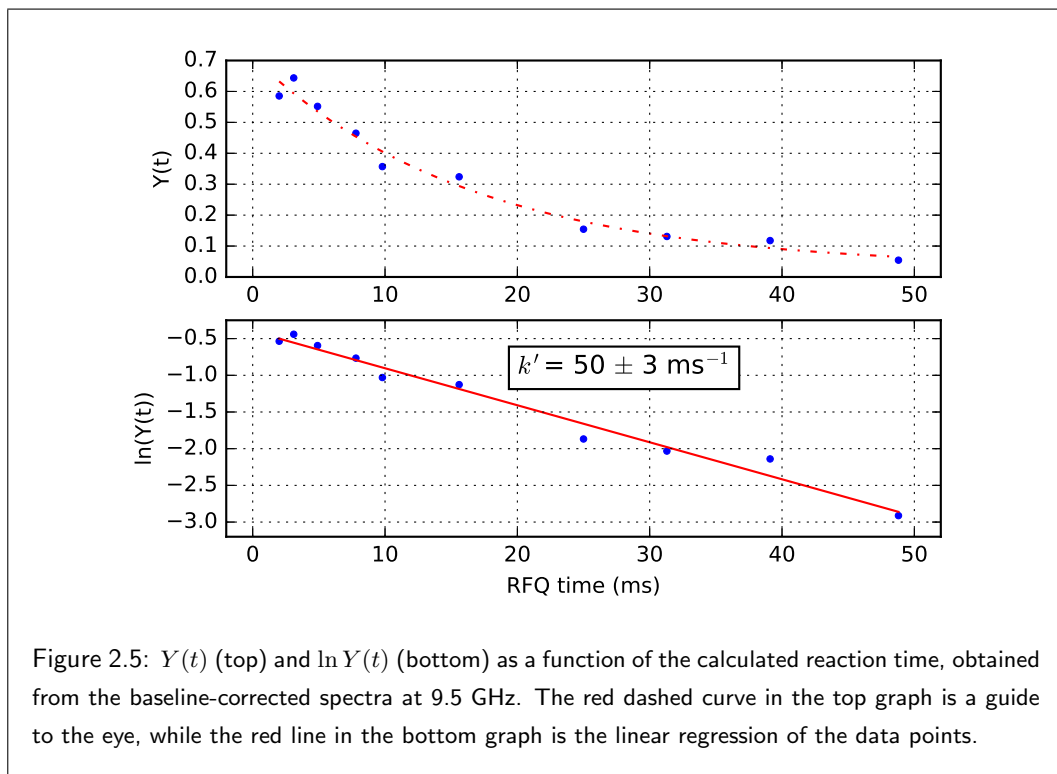
Figure 2.4: Baseline-corrected, single-scan 9.5 GHz cw EPR spectra of RFQ samples, Mb1 to Mb10, in the time range between 2.0 and 48.8 ms.

range of the contamination.

From the logarithmic linearization of the decay (Figure 2.5, bottom) the apparent reaction rate $k' = 50 \pm 3$ ms^{-1} is extracted by use of Equation 2.2. The k' then yields the real reaction rate $k = 4.2 \pm 0.2 \cdot 10^3$ M^{-1} s^{-1} through Equation 2.3. By extrapolating the semilogarithmic line to $\ln Y(t) = 0$, a freezing time of 7.9 ± 0.4 ms is obtained.

Figure 2.6 shows the 275 GHz spectra of the Mb0 sample to illustrate the low-field HS-Fe(III) signal at $B_0 = 3.54$ T (left), and the Mn^{2+} signal (right) around $g = 2$ (central $B_0 = 9.8453$ T). Because the range of the magnetic field is broad, it is more convenient to record the two spectra separately. The six lines of the manganese spectrum arise from the transition between the two spin states $m_s = \pm 1/2$, which are further split by the hyperfine interaction with the $I = 5/2$ nuclear spin of Mn.

Figure 2.7 shows the Mn^{2+}-normalized spectra of the RFQ samples Mb1 to Mb10. The solution Mb0 is included to show the intensity of the HS-Fe(III) signal in the absence of sodium azide, i.e., ideally at a reaction time $t = 0$. The decay of the HS-Fe(III) signal as a function of time, obtained from the spectra of the RFQ samples Mb1 to Mb10, is depicted in Figure

Figure 2.5: $Y(t)$ (top) and $\ln Y(t)$ (bottom) as a function of the calculated reaction time, obtained from the baseline-corrected spectra at 9.5 GHz. The red dashed curve in the top graph is a guide to the eye, while the red line in the bottom graph is the linear regression of the data points.

2.8 (top), along with the linearization of the points. The HS signal intensity was taken at $B_0 = 3.4780$ T (max) and $B_0 = 3.5948$ T (min), while the Mn^{2+} intensity was taken from the sixth peak of the Mn^{2+} spectrum at $B_0 = 9.8680$ T (max) and $B_0 = 9.8690$ T (min).

An apparent reaction rate $k' = 52 \pm 2$ ms^{-1} is extracted with Equation 2.2, from which the reaction rate $k = 4.3 \pm 0.2 \cdot 10^3$ M^{-1} s^{-1} is obtained with Equation 2.3. By extrapolating the semilogarithmic line to $\ln Y(t) = 0$, a value of 0.25 ± 0.01 ms is obtained.

2.4   Discussion and conclusions

The reaction rates calculated from the logarithmic $Y(t)$ curves obtained from 9.5 GHz and 275 GHz spectra (Figures 2.5 and 2.8, respectively) coincide, keeping into account the measurement errors of about 4 and 6 %, respectively.

As mentioned in the Results Section, by extrapolating to $\ln Y(t) = 0$ of the semilogarithmic lines of the decays obtained at 9.5 and 275 GHz, values of 7.9 ± 0.4 ms and 0.25 ± 0.01 ms are

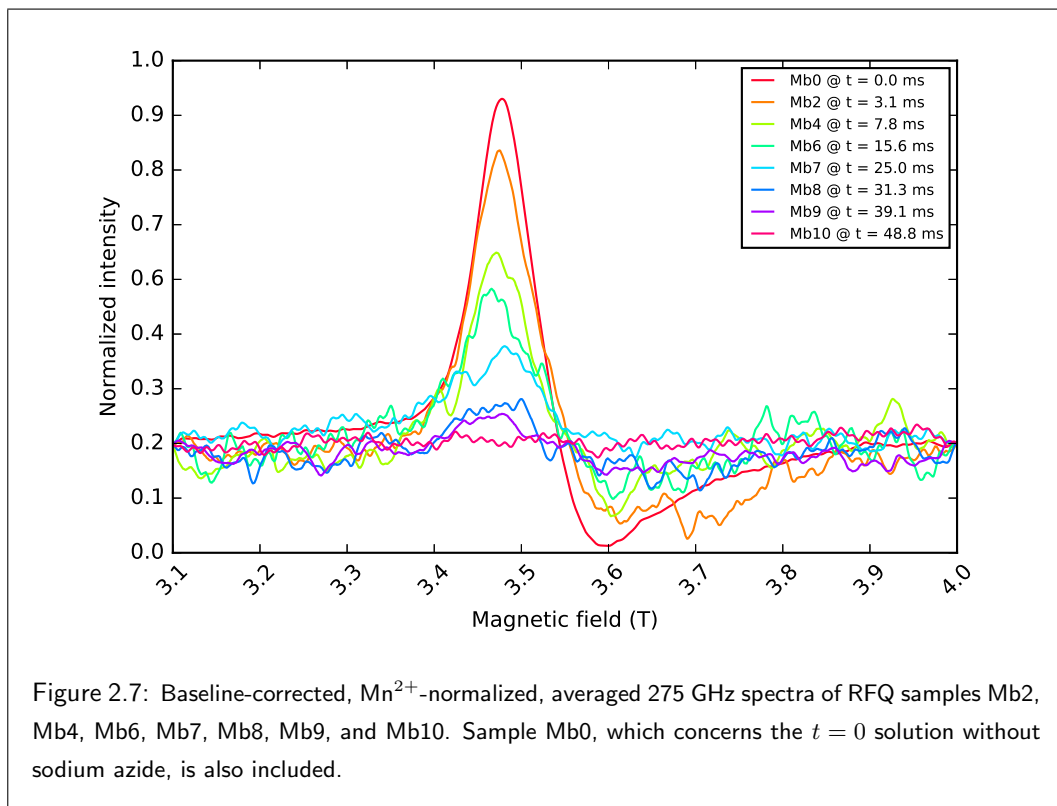Figure 2.6: Baseline-corrected, averaged 275 GHz spectra of sample Mb0: the myoglobin HS-Fe(III) signal (left), and the Mn^{2+} signal (right).
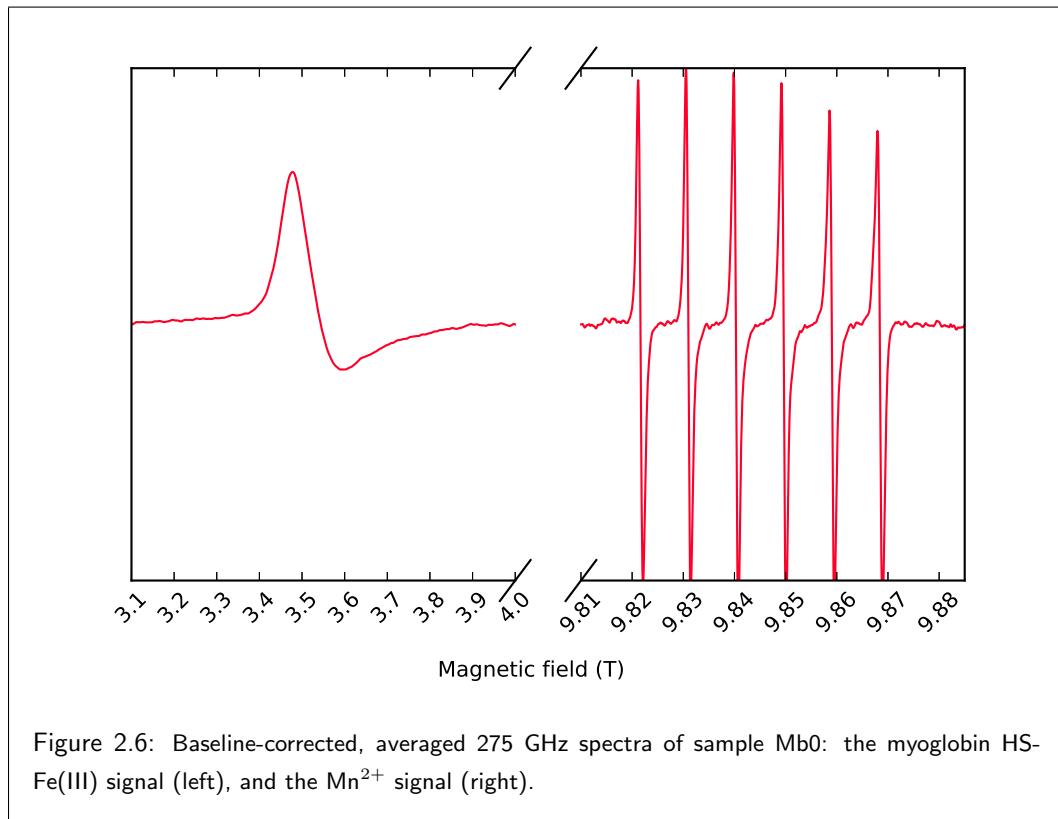
obtained, respectively. While for the experiments at 9.5 GHz the Mb0 sample (representing the reaction at $t = 0$) was prepared from the very same solution batches as the other RFQ samples, for the experiments at 275 GHz this was not possible because, as mentioned in Subsection 2.2.2, these were performed about a year later. The Mb0 solution was thus prepared from different batch solutions than the original ones used to prepare the RFQ samples. It is thus clear that in the case of the experiments at 275 GHz, the Mb0 does not constitute a reliable representation of the reaction at $t = 0$. Therefore, only the semilogarithmic decay obtained at 9.5 GHz can yield a measure of the so-called *freezing time*.

It is interesting to analyze the semilogarithmic decays obtained at 9.5 GHz and 275 GHz *together*, so as to get an average value of k. However, since the semilogarithmic decay at 275 GHz returns a different time when extrapolated to $\ln Y(t) = 0$ than the decay at 9.5 GHz, in order to be able to plot the two together it is necessary to vertically shift the former by a factor ΔY given by 2.9:

2. EFFECTIVE COUPLING OF RFQ TO HIGH-FREQUENCY EPR

Figure 2.7: Baseline-corrected, Mn^{2+}-normalized, averaged 275 GHz spectra of RFQ samples Mb2, Mb4, Mb6, Mb7, Mb8, Mb9, and Mb10. Sample Mb0, which concerns the $t = 0$ solution without sodium azide, is also included.

$$\Delta Y = \frac{m_{275}}{m_{9.5}} q_{9.5} - q_{275} = 0.4 \tag{2.9}$$

where m_{275}, $m_{9.5}$, and q_{275}, $q_{9.5}$ indicate respectively the slopes and intercepts of the linear fits of the logarithmic $Y(t)$ curves, from 275 and 9.5 GHz experiments.

If the points of the 275 GHz kinetics are thus shifted by ΔY, as expected they end up within the same range as the points of the 9.5 GHz kinetics, and in this way it is possible to calculate a regression line originating from the unified points at 9.5 and 275 GHz (Figure 2.9). An apparent k' is thus obtained of 51 ± 2 ms^{-1} by use of Equation 2.2, corresponding to a reaction rate $k = 4.2 \pm 0.2 \cdot$ M^{-1} s^{-1} (obtained through Equation 2.3).

As summarized in Table 2.4, this value of k lies in the range of reaction rates to be found in the literature for the myoglobin-azide reaction, under conditions similar to those of the present work. It should be noticed that the reaction has a critical dependence on the pH [45] and on the azide concentration [35] [36], although in theory all the studies reported in Table 2.4 are carried
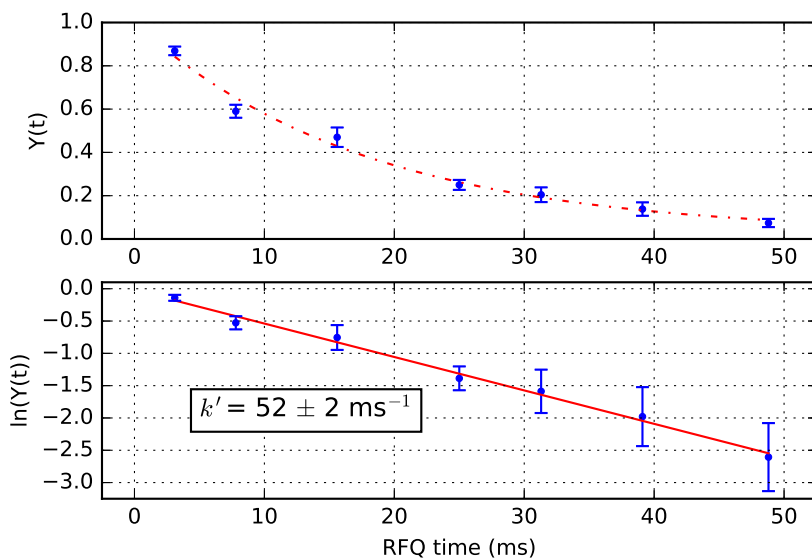
Figure 2.8: $Y(t)$ (top) and $\ln Y(t)$ (bottom) as a function of the calculated reaction time, obtained from the spectra at 275 GHz. The red dashed curve in the top graph is a guide to the eye, while the red line in the bottom graph is the linear regression of the data points.

out under pseudo-first-order conditions. Given these considerations, the k found in the present work is in good agreement with the data from the literature.

In conclusion, these results convincingly prove that the method described in the present work, i.e., the coupling of RFQ to HF-EPR, is successful.

The approach is based on a previously developed method that enables the efficient and reproducible packing of RFQ samples in 150-μm sized capillaries suitable for 275 GHz EPR, and the safe and fast loading of the capillaries in the pre-cooled cryostat of our 275 GHz EPR spectrometer.

Besides this notable improvement over other methods reported in the literature so far, our approach also allows the use of only one single series of RFQ samples, to be used both at 9.5 and 275 GHz, and flexibly at any intermediate frequency in between. This remarkable advantage reduces the amount of material to be used in kinetic studies (which is particularly beneficial for biological samples), and improves the consistency of the method in that only one set of samples is used for the two frequencies.
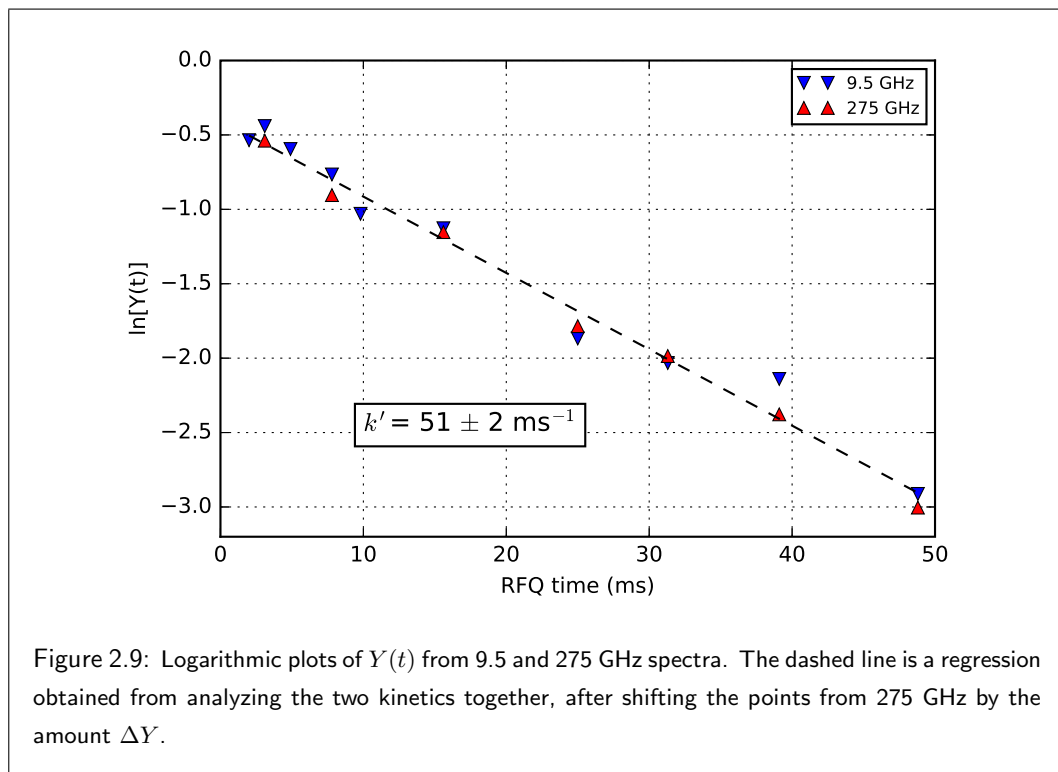
Figure 2.9: Logarithmic plots of $Y(t)$ from 9.5 and 275 GHz spectra. The dashed line is a regression obtained from analyzing the two kinetics together, after shifting the points from 275 GHz by the amount ΔY.

Source	k ($\cdot\ 10^3$ M^{-1} s^{-1})	[metMb] : [Az] (mM)	pH	T (°C)
This work	4.2 ± 0.2	1.2 : 12	7.8	21.5
[45]	4.4 / 3.1 / 2.5	0.09 : 0.05 ÷ 0.7	7.0 / 7.3 / 7.5	25.0
[35]	3.04 (2.83)	0.44 : 6.25 (12.5)	7.8	21.7
[36]	2.9 (1.9)	0.25 : 6.25 (12.5)	7.8	21.8
[39]	2.2	0.625 : 6.25	7.8	22.0
[21]	6.0	1 : 5	7.0	23.0
[37]	2.8 ± 0.3	2.4 : 30	7.8	not specified

Table 2.4: Comparison of the values of k for the reaction of metmyoglobin (metMb) with sodium azide (Az), as found in the present work and from the literature, under similar conditions of concentration ratios, pH, and temperature. In References [35] and [36], two different values of k are found for two different concentrations of sodium azide, which are reported in brackets. In Reference [45], three different values of k are found for three different values of pH; as far as the concentration of sodium azide is concerned, the authors refer to a range of concentrations, without specifying the actual ones.

3

Temperature-Cycle EPR: A novel method for the investigation of chemical dynamics

3.1   Introduction

Investigating intermediates and kinetics of chemical reactions is essential to understand the function and mechanism of many (bio)molecular processes, from enzymatic catalysis to polymer degradation. However, given the short time scales on which most chemical systems react, and the even shorter time scales on which their intermediates exist, kinetic measurements are not an easy task.

It is often the case in molecular systems of biological importance that the reaction intermediates involved are paramagnetic species, for whose investigation the most suitable technique is Electron Paramagnetic Resonance (EPR) [46] [12].

The research idea of this Chapter is therefore that of finding a method that enables EPR investigations of chemical kinetics. The method should be flexible and versatile enough, so as to be applicable to a wide range of molecular systems, and on time scales down to milliseconds.

Flow methods, such as the stopped- and continuous-flow ones, where the reaction of two components is followed after they have been rapidly mixed, have extensively been employed to study chemical kinetics down to several milliseconds and tens of microseconds [47] [48]. They are of great importance because they offer high time resolution and quantitative applications in EPR [49], and they allow continuous detection of the kinetics of molecular systems. However, such methods require large volumes of reactants, which is disadvantageous when having to do with biological materials.

Rapid Freeze-Quench (RFQ) is another well-established, standard technique to investigate chemical kinetics with a time resolution of milliseconds down to microseconds [35] [38] [20]. However, as described in Chapter 2 of this thesis, this method suffers from a few drawbacks, such as the large amount of material required, a low reproducibility due to the number of different samples needed, and the inefficient sample packing for applications in EPR.

It is thus desirable to turn to alternative methods to investigate (bio)molecular dynamics, ideally allowing high time resolution, need of little amount of material, and versatility of application.

The idea of producing temperature jumps (T-jumps) directly on the system under study was first put forward by Eigen and coworkers in 1963, who devised a method to induce a T-jump via an electrical discharge of a high-voltage capacitor through a conductive solution [22], and thus also called "Joule heating". To date still commercially available [23], this method has been extensively used in various fields, from biophysics [50] [51] to inorganic chemistry [52] [53], and has been coupled to several detection techniques, mainly optical spectroscopies such as fluorescence spectroscopy [54]. The Joule-heating technique makes it possible to achieve a time

resolution down to microseconds, but only when T-jumps of a few degrees are applied; this is a clear limitation of the method, as an increase of the extent of the T-jumps implies significantly longer heating pulses. Furthermore, since the solution medium being conductive calls for high concentrations of electrolytes added to it, applications of the Joule heating method are limited to polar solvents.

With the advent of pulsed lasers, dramatically shorter time scales were reached in biophysics (from milliseconds down to nanoseconds), thanks to the high time resolution offered by the pulsed-laser technologies.

Upon light excitation of dye molecules added to the system or, more universally, of the solvent molecules, heat release follows, and the system is then subject to a temperature-increasing T-jump. Particularly for aqueous solutions, excitation of the overtone of the OH stretching band of water molecules is possible upon intense irradiation with near-infrared light between 1300 and 2100 nm [55].

The first attempts of laser-induced T-jump experiments date back to the 1960s, with T-jumps between 0.1 and 10 °C in microliter-size volumes of aqueous solutions with IR or visible laser pulses of the length of tens of nanoseconds [56] [57] [58].

Since their introduction, laser-induced T-jump methodologies have found biophysical applications in the study, for instance, of the folding of peptides, proteins, and nucleotides [59] [60] [61] [62], of the dynamics of enzymatic reactions [63], and of protein-nucleic acid interactions [64].

The presence of a large body of well-established T-jump methodologies applied to the study of (bio)molecular dynamics, together with the importance of EPR as a unique tool in biophysical and biochemical investigations, were the starting points in the design of a method that couples laser-induced T-jumps to EPR for the study of chemical kinetics.

This Chapter describes the implementation of *Temperature-Cycle EPR* (abbreviated as T-Cycle EPR), a novel high-frequency EPR technique that couples laser-induced T-jumps to a home-built 275 GHz EPR spectrometer to explore short-lived intermediates and kinetics of chemical reactions in aqueous solutions involving paramagnetic species. The reason for a method with high-frequency EPR (HF-EPR) is that it offers high spectral resolution and, if coupled to single-mode cavities, high sensitivity [34] [65].

The minuscule resonant volume (20 nL) of the single-mode cavity of our 275 GHz EPR spectrometer [34] can be advantageously exploited to heat *in situ* a mixture of reactants, initially at a temperature where no reaction occurs, by means of an IR-laser-induced T-jump, in a homogeneous, reproducible, and controllable manner. This *in-situ* T-jump increases the temperature

of the mixture (controlled by a cryostat) to a temperature at which the reaction takes place for an arbitrary period of time. The application of a sequence – or *cycle* – of T-jumps to the frozen mixture thus lets the molecular reaction under study unfold, the paramagnetic species involved being depleted (in the case of reactants) or being formed (in the case of intermediates or products), and a kinetic study of the chemical system is possible.

3.2   Temperature-Cycle EPR

To give a simple illustration of the working of T-Cycle EPR, its application to a mixture of two reagents, sitting at a temperature where no reaction occurs, is considered. The bottom part of Figure 3.1 schematically illustrates a sequence of T-Cycle *steps* applied on the aforesaid mixture (note that what is referred to as T-Cycle is the ensemble of all such steps). Upon application of each T-Cycle step, the reaction has progressed by a time amount in principle defined by the duration of the laser-induced T-jump associated to the T-Cycle step. The reactants are thus depleted and, in the case where at least one of the two is paramagnetic, their EPR signal decreases over time. This is depicted in a simplified way in the upper part of Figure 3.1, with a model intensity decay of the EPR signal of one of the two reactants as a function of time.

The whole kinetics of a reaction, or the evolution of paramagnetic intermediate species, can thus be studied from one single sample, as the laser-induced T-jumps are applied *in situ* directly into the spectrometer's cavity where the sample is located.
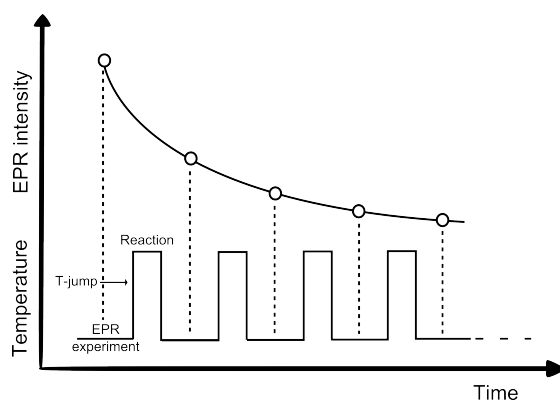

Figure 3.1: Scheme of a Temperature-Cycle experiment.

Each step of a T-Cycle experiment can be viewed as composed of five parts, involving up to

three different temperatures, namely a *Measurement Temperature*, a *Preparation Temperature*, and a *Reaction Temperature*. Figure 3.2 schematically represents the three temperatures and the parts a T-Cycle step is composed of:

(A) A mixture of reactants sits at an arbitrary *Measurement Temperature*, namely a temperature at which no reaction occurs, and which is suitable to perform a desired EPR experiment. It can be arbitrarily low (i.e., as low as a He-flow cryostat allows), and thus be suitable for all those EPR experiments that require cryogenic temperatures.

(B) The non-reacting mixture is taken to a higher temperature, called *Preparation Temperature*, still low enough for the sample not to undergo any reaction, but high enough to apply a T-jump to temperatures at which the reaction takes place.

(C) An IR-laser-induced T-jump of arbitrary time length and power is applied. During this time the sample reaches a temperature defined as *Reaction Temperature*, where the reaction occurs for the specific time length.

(D) When the IR-heating is turned off, the sample's temperature drops back to the *Preparation Temperature*, which prevents the reaction to go further.

(E) The sample can be taken again to the *Measurement Temperature*, where the next EPR spectrum can be recorded.

Both the Measurement Temperature and the Preparation Temperature are regulated by a cryostat.

The Temperature-Cycle method was implemented on a home-built 275 GHz EPR spectrometer, whose insert is wired with a multimode optical fiber that couples the cavity with an infrared diode laser operating at 1550 nm (details are provided in Subsection 3.3.2). This wavelength is absorbed by the solvent water molecules [55], which release heat upon relaxation, causing an aqueous solution in the cavity to warm up (the solution may or may not be frozen). The laser's light is not focused and is shone through the lower, grid-like part of the brass cavity, so that a scattering of the light is produced and the laser hits the sample directly in the cavity.

The thermal diffusivity of the solvent and of the sample holder in contact with it is one of the factors limiting how fast a determined volume of solution reaches a certain temperature when subjected to a laser-induced T-jump [23]. It follows that, associated to any T-jump, there always are a rise time and a fall time, determined by the physical properties of the solvent and of the
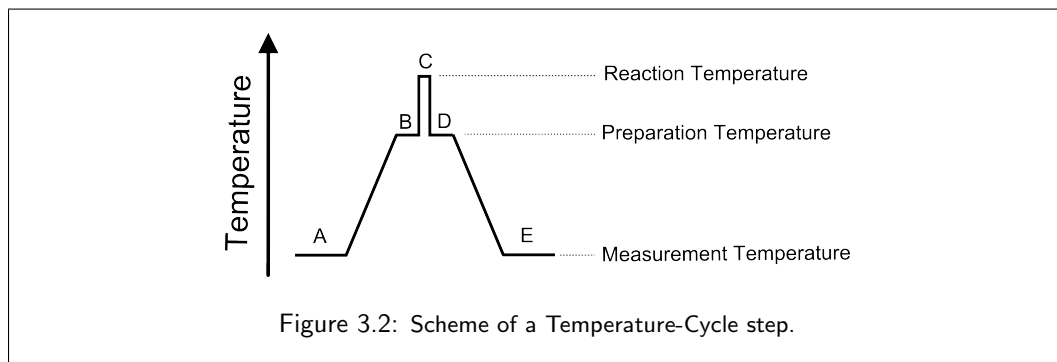
Figure 3.2: Scheme of a Temperature-Cycle step.

sample-holder. In order to achieve a picture of the time scales of the rise and fall time involved in a laser-induced T-jump event, the 275 GHz EPR intensity variations of a TEMPONE solution in a mixture of water and glycerol were recorded as a function of time, while periodically heating the solution with laser pulses to induce T-jumps. TEMPONE is a nitroxide radical structurally and chemically similar to TEMPOL, with the difference that the former has a 4-oxo moiety instead of a 4-hydroxyl one. A solution of TEMPONE in water and glycerol acts as a sort of thermometer to characterize the T-jumps, because the high-frequency EPR intensity variations of this system are closely associated to a change in temperature. Figure 3.3 shows the averaged time profile of a TEMPONE solution, and provides some experimental details. Upon applying a laser pulse of the duration of 1200 ms at a power of 3.5 W, a rise time of at least 300 ms and a fall time of at least 500 ms can be deduced. This affects the time the system spends at the equilibrium temperature reached with the T-jump, and obviously becomes more and more important to take into account as the duration of the laser pulse becomes shorter. An analysis of the temperatures that are possible to reach upon application of a laser-induced T-jump is provided in the Appendix to this Chapter, and constitutes a novel method following the premises cast in the work published by Azarkh and Groenen [24].

3.3 Experimental

3.3.1 Materials

The mixtures of 4-hydroxy-TEMPO, also known as TEMPOL (Sigma-Aldrich, cat. n. 176141), and L($+$)-ascorbic acid (Carl Roth, cat. n. 3525.1) used for the T-Cycle experiments described in this Chapter were prepared from batch solutions at concentrations of 4 mM (TEMPOL) and 2 mM (ascorbic acid), in a mixture of water and glycerol 1:1 in volume. In this way, after mixing
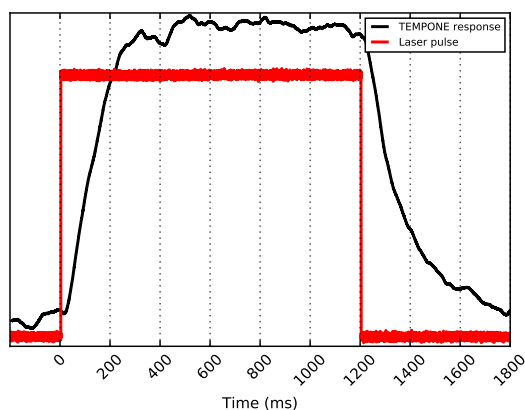
Figure 3.3: Black: time profile of the EPR signal of a solution of TEMPONE (at a concentration of 2 mM, in a mixture of water and glycerol 1:1 in volume), when heated with a 1200 ms long laser pulse at 3.5 W, from a cryostat-regulated temperature of 243 K. The red trace represents the laser pulse, turned on at $t = 0$. The time profile is visualized with an oscilloscope while measuring the 275 GHz EPR intensity of the TEMPONE solution at a magnetic field of 9.8202 T, which is a field position where the spectral intensity of TEMPONE is particularly sensitive to temperature variations (as can be appreciated in Figure 3.13).

equal volumes of the two reagents, the resulting concentrations of TEMPOL and ascorbic acid were 2 and 1 mM, respectively. Unless otherwise specified, all the experiments described in this Chapter were performed on samples having the above mentioned composition.

Since under such conditions the reduction of TEMPOL by ascorbic acid takes place on a time scale of minutes, the manual mix of the components is an easy procedure. To prepare each sample, 100 μL of TEMPOL were added to 100 μL of ascorbic acid under magnetic stirring, and after waiting a few seconds to let the two solutions mix homogeneously, a previously prepared quartz capillary (150 μm inner diameter) is dipped in the mixture, which is collected simply by capillary force. The capillary is then rapidly dropped in liquid nitrogen so as to stop the reaction, and stored for later measurements. The whole procedure, from the manual mixing to the freezing of the filled capillary, takes between 7 and 10 seconds, which constitute an acceptable "dead time" of the method, considering the time scales involved in the experiments described in this Chapter.

3.3.2 Setup

The samples are introduced in the single-mode cavity of a pre-cooled home-built probe head [43] in the way described in Chapter 2 of this thesis. The probe head is then inserted in the He-flow cryostat (CF935, Oxford Instruments) of a home-built 275 GHz EPR spectrometer [34], at a Measurement Temperature of 223 K. A Preparation Temperature of 243 or 263 K, depending on the experiment, is reached prior to the application of a T-jump.

The probe head is wired with a multi-mode optical fiber (Thorlabs, model n. FG105LCA, 0.22 NA, core size 105 μm, FC/PC connector to the laser) that couples the cavity to a diode laser operating at 1550 nm, with a maximum output power of about 3.5 W (SemiNex Corp., model n. HHF-110, serial n. 2027). The diode laser is mounted on a home-built power supply and fan-cooling unit that allows the tuning of the input current fed to the laser and thus of the output power.

As schematically shown in Figure 3.4, the flat-cleaved end of the fiber enters the bottom of the probe head, facing the grid-like part of the brass cavity and thus allowing direct irradiation of the sample.

Figure 3.4: Scheme of the probe head of the 275 GHz EPR spectrometer. On the left is shown the bottom of the probe head, and the arrow indicates the distance of the resonant cavity from the bottom. In red is depicted the optical fiber that couples the probe head to the laser. Its flat-cleaved end sits in front of the bottom of the cavity.
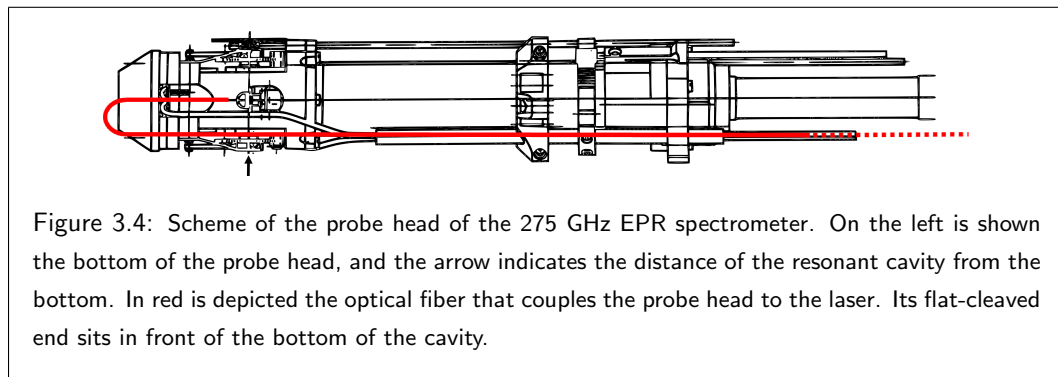
Figure 3.5 depicts a zoomed-in scheme of the flat-cleaved end of the optical fiber wired to the probe head. The optical fiber with its protective tubing (shown in orange) is secured on a T-shaped brass support, which is later screwed onto the bottom of the probe head. The terminal portion of the fiber's protective tubing is removed, and the fiber is fastened on the brass support. The last portion of the fiber's cladding is stripped off, and the bare fiber is exposed. Appropriate lengths are illustrated in the Figure.

Given the time scale of minutes at which the system under study reacts, relatively long laser

Figure 3.5: Top-view scheme of the flat-cleaved end of the fiber (on the right), secured on a T-shaped brass support, entering the bottom of the probe head. The end of the bare fiber is at a distance of 3 mm from the center of the probe head's cavity.
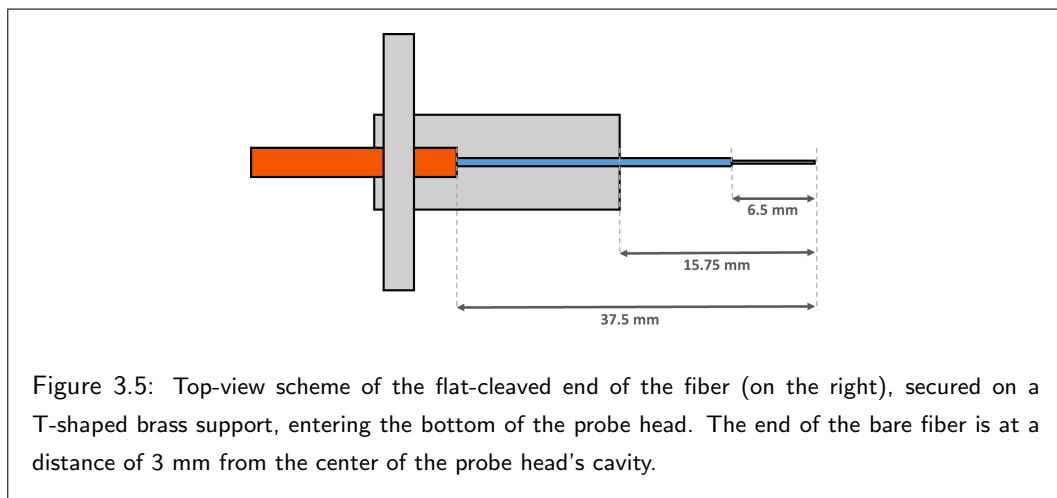
pulses – of the duration between 20 and 400 s – were applied in the experiments described in Section 3.4.

The cryostat temperature was detected with a Pt100 sensor, whose resistance and calculated temperature values were read with a Keithley 2100 $6^{1}/_{2}$ Digit Multimeter (Tektronix). The Pt100 sensor is located in the close proximity of the insert's cavity; however, since it is not situated exactly *in* the cavity, the actual temperature of the sample might deviate from those presented here.

3.3.3   Internal standard

Preliminary experiments showed that uncontrolled changes in the EPR cavity occur upon laser irradiation, resulting in variations of the TEMPOL signal that may be larger than its decay due to the reduction of TEMPOL by ascorbic acid. Such variations might thus make it impossible to follow a kinetic curve without the use of a standard signal.

A broadly used standard in EPR is the manganese(II) ion, which at high frequency shows six intense and well-defined lines arising from the transition between the two spin states $m_s = \pm^1/_2$, further split by the nuclear hyperfine interaction with the nuclear spin $I = {}^5/_2$ of the manganese nucleus.

At the time of the experiments described in this Chapter, an incidental presence of Mn^{2+} signals was observed in the cavity of the 275 GHz spectrometer. Since this contamination clearly showed the typical 6-line spectrum of Mn^{2+} (see Figure 3.6), with spectral intensities suitable for the

purposes of the present research, it was used in the experiments described below (Section 3.4), instead of adding $MnCl_2$ to the solution. This procedure differs from what is commonly done in EPR studies, where manganese(II) is added in small concentration to the studied system in the form of $MnCl_2$ [66].
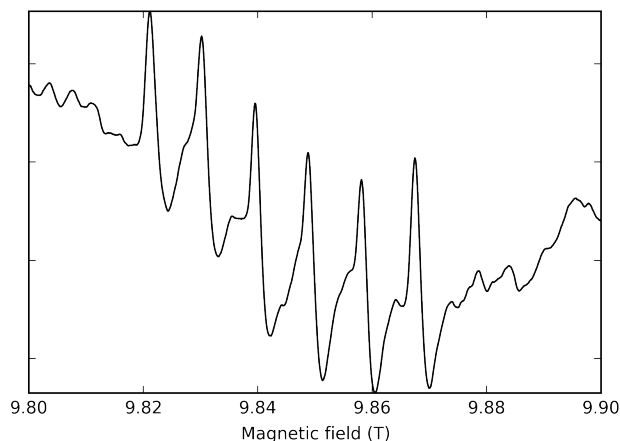
Figure 3.6: Room-temperature cw EPR spectrum at 275 GHz of the Mn^{2+} present in the probe head cavity as an incidental contamination, and used as an internal standard.

3.4 Temperature-Cycle EPR demonstrated on a model reaction

This Section describes the application T-Cycle EPR on frozen mixtures of TEMPOL and ascorbic acid, whose reaction is taken as a model system for the present investigations (as described in Subsection 3.4.1). Subsection 3.4.2 shows that T-Cycle EPR yields kinetics on a time scale of minutes. Subsection 3.4.3 shows that T-Cycle EPR allows to study chemical reactions flexibly, as arbitrary Reaction Temperatures can be reached by selecting appropriate Preparation Temperatures and laser powers.

3.4.1 The TEMPOL-ascorbic acid reaction as a model system

In order to show the working of T-Cycle EPR, a well-known model reaction was used, namely the reduction of the nitroxyl radical TEMPOL (4-hydroxy-TEMPO) by ascorbic acid, yielding

the corresponding diamagnetic hydroxylamine (a scheme of the reaction is shown in Figure 3.7) [67] [68] [69] [70]. This reaction is particularly advantageous for the purposes of this Chapter for two reasons. Firstly, it occurs on relatively long time scales (minutes), which is ideally suited for the demonstrative experiments aimed at proving the effectiveness of T-Cycle EPR. Secondly, the fact that the TEMPOL molecule gives rise to spectra that differ greatly in intensity and shape as a function of temperature (as described in Section 3.2), is of great use for the determination of the reaction temperatures reached upon application of the T-jumps, as described in detail in the Appendix to this Chapter.
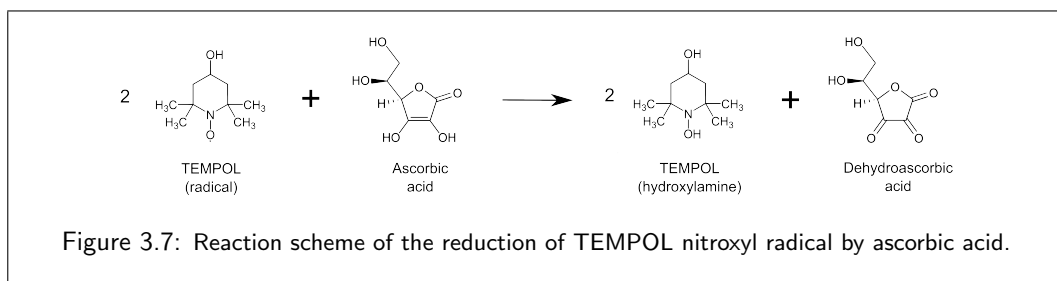

Figure 3.7: Reaction scheme of the reduction of TEMPOL nitroxyl radical by ascorbic acid.

Before going into the details of the results, a brief introduction will be given as to what a typical EPR spectrum of a nitroxide radical looks like at high microwave frequency.

As can be seen from the representation of the TEMPOL molecule in the left-hand side of Figure 3.7, a single unpaired electron, having spin $S = 1/2$, is localized on the nitroxide group of the molecule and thus interacts with the ^{14}N nucleus, which possesses nuclear spin $I = 1$. This hyperfine interaction causes a splitting of the spin energy levels of the electron, which in addition exhibits an anisotropic **g** tensor. The resulting high-frequency EPR spectrum is shown in Figure 3.8, arising from a frozen TEMPOL solution. The three components g_x, g_y, and g_z of the **g** tensor are clearly separated. The splitting of the lines into $2I + 1 = 3$ components due to the hyperfine interaction with the ^{14}N nucleus is only visible in the high-field part of the spectrum, as the hyperfine tensor **A** is anisotropic too and only the A_z component is large enough to be resolved [24].

Finally, three out of six lines of the Mn^{2+} spectrum are visible around 9.86 T (the first three, at lower field, are hidden in the TEMPOL spectrum, which is much more intense).

In order to monitor the reduction of TEMPOL by ascorbic acid, for each time point the intensity of the g_x component of the EPR spectrum of TEMPOL at 9.8064 T was measured, and divided by the peak-to-peak intensity of the fifth line of the spectrum of Mn^{2+} at 9.858 T,
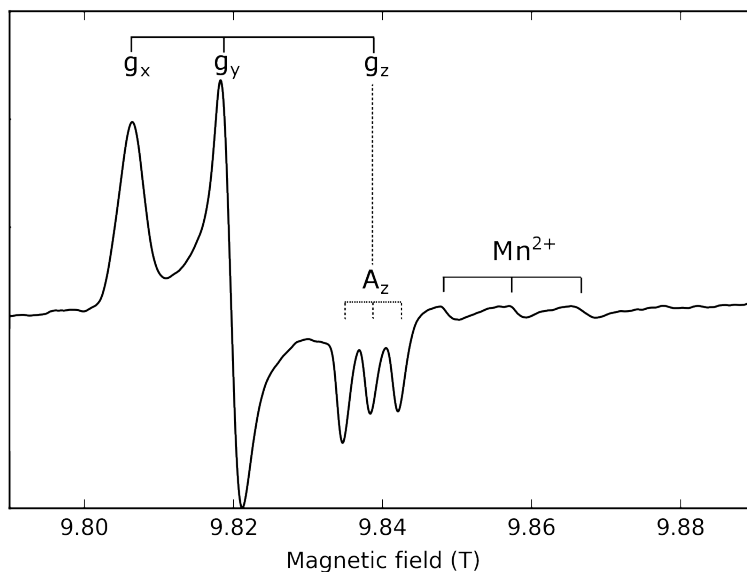
Figure 3.8: Continuous-wave 275 GHz EPR spectrum at 223 K of a frozen solution of TEMPOL at a concentration of 2 mM, in a mixture of water and glycerol 1:1 in volume. The three high-field components are part of the six-line spectrum of Mn^{2+}, present as an incidental impurity in the spectrometer's cavity.

used as a standard as described in Subsection 3.3.3. A decay curve is thus obtained by plotting the Mn-normalized decrease of the spectral intensity of TEMPOL as a function of the time steps where the laser was turned on. The g_x peak of TEMPOL at 9.8064 T was chosen because it does not overlap with the Mn^{2+} spectrum, and because it is known that the ascorbate radical anion gives a signal overlapping the g_y of TEMPOL [67].

Similarly to the procedure described in Chapter 2 of this thesis, in order to obtain a decay from the reduction of TEMPOL by ascorbic acid, the quantity $Y(t)$ has to be calculated from the decay of the TEMPOL signal as a function of time. $Y(t)$ is the ratio of the concentration of TEMPOL at any time point t and at $t = 0$, $[TL]_t/[TL]_0$, and is directly proportional to the ratio of the EPR intensity of the respective signals normalized by the Mn^{2+} signal, $(S'_{TL})_t/(S'_{TL})_0$, as shown in Equation 3.1. Note that S' represents the signal S *normalized* by manganese (Equation 3.2). Note that although S_{Mn} does not change as a function of time, it still might differ from spectrum to spectrum due to the changes in the cavity induced by the laser-induced T-jumps.

It is therefore measured for each spectrum.

$$Y(t) = \frac{[TL]_t}{[TL]_0} = \frac{(S'_{TL})_t}{(S'_{TL})_0} \tag{3.1}$$

$$(S'_{TL})_t = \frac{(S_{TL})_t}{S_{Mn}} \tag{3.2}$$

The EPR spectra used to determine the decays described in Section 3.4.2 and 3.4.3 are the average of four scans. Whenever shown, the error bars associated to the points of the decays represent the standard errors calculated from the four scans. Table 3.1 displays the experimental parameters used to record the spectra.

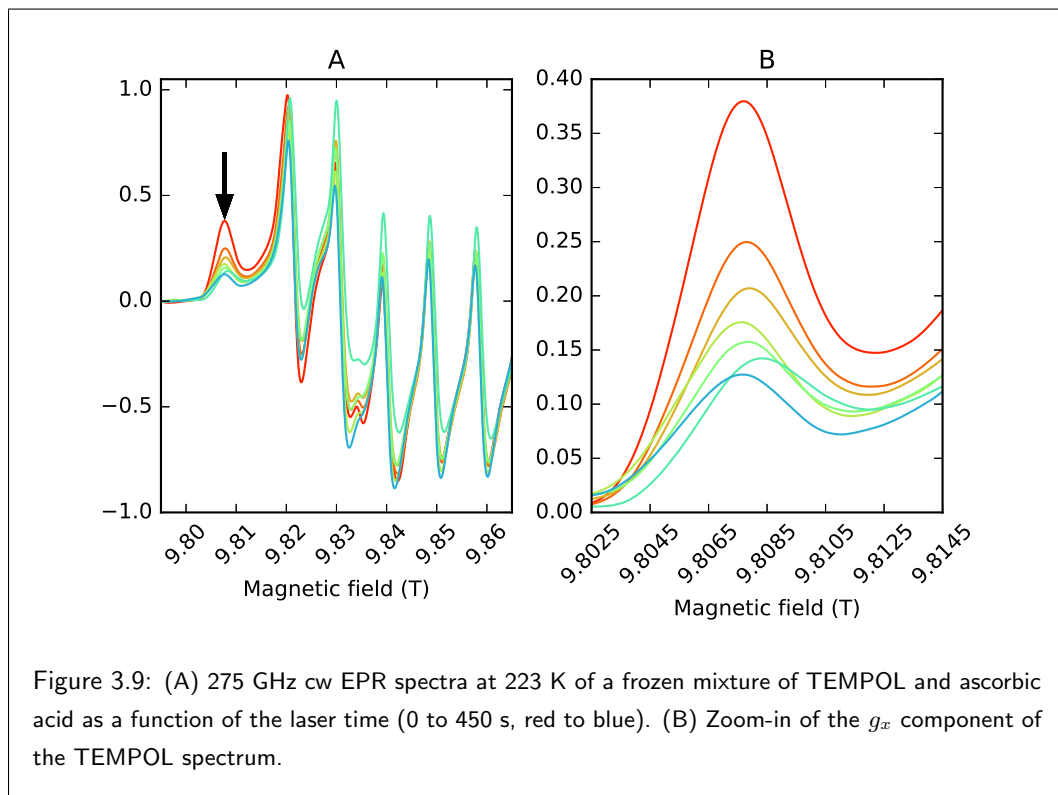| Field range (T)	# of points	Mod. freq. (kHz)	Mod. ampl. (mT)	Time const. (s)	Conversion time (ms)	Microwave power (μW)	T (K)
9.7950 ÷ 9.8650	1800	1.253	1.0	1	62.5	1.74	223

Table 3.1: Experimental parameters of the spectra at 275 GHz. *Mod. freq.* and *Mod. ampl.* are the field modulation frequency and amplitude, respectively.

3.4.2 First demonstration of Temperature-Cycle EPR

The application of T-Cycle is demonstrated on a frozen mixture of TEMPOL and ascorbic acid, and the resulting kinetics is observed at 275 GHz. The T-Cycle steps designed for this experiment, of the kind shown in Figure 3.2, feature a Measurement Temperature of 223 K, and a Preparation Temperature of 243 K, both cryostat-controlled. The T-jumps are applied with laser pulses at a nominal power of 3.5 W, with a duration of either 50 or 100 s. The experiment described in this Subsection is henceforth referred to as "Experiment A".

Figure 3.9 A shows the 275 GHz EPR spectra of TEMPOL normalized by Mn^{2+}, each obtained after a T-Cycle step described above. The low-field part of the spectrum shows the g_x component of TEMPOL, which is the only one not overlapping with the Mn^{2+} spectrum used for normalization. Figure 3.9 B is a zoomed-in view of the g_x component of TEMPOL, which shows a decay as a function of the laser time (red to blue).

By plotting the quantity $Y(t)$ (introduced in Subsection 3.4.1) as a function of the "laser time", a clear decay curve is achieved, as shown in Figure 3.10. The laser-time axis is obtained by summing up the duration of each T-jump in the T-Cycle sequence, up to 450 s. A decay with a characteristic time of more than 100 s can be observed.

Figure 3.9: (A) 275 GHz cw EPR spectra at 223 K of a frozen mixture of TEMPOL and ascorbic acid as a function of the laser time (0 to 450 s, red to blue). (B) Zoom-in of the g_x component of the TEMPOL spectrum.

3.4.3 Flexibility of Temperature-Cycle EPR

Being able to achieve different Reaction Temperatures, either by adjusting the Preparation Temperature, or by applying laser pulses of different power, is a desirable feature of the T-Cycle method, as it provides flexibility in the study of chemical kinetics in conditions different from room temperature. This Subsection describes the feasibility of different kinds of T-Cycle EPR experiments on samples of identical composition.

Figure 3.11 shows the design of three experiments performed to show the flexibility of the T-Cycle method. In the rest of this Subsection, the three temperatures that constitute the T-jumps (as described in Section 3.2) will be shortened as T_{meas}, T_{prep}, and T_r.

The three experiments A, B, and C, carried out at a T_{meas} of 223 K on three frozen mixtures of TEMPOL and ascorbic acid of identical composition, are described below. Note that Experiment A is the same as that described in Subsection 3.4.2.

(A) From $T_{prepA} = 243$ K, a laser power of 3.5 W is applied, letting the sample reach a T_{rA}
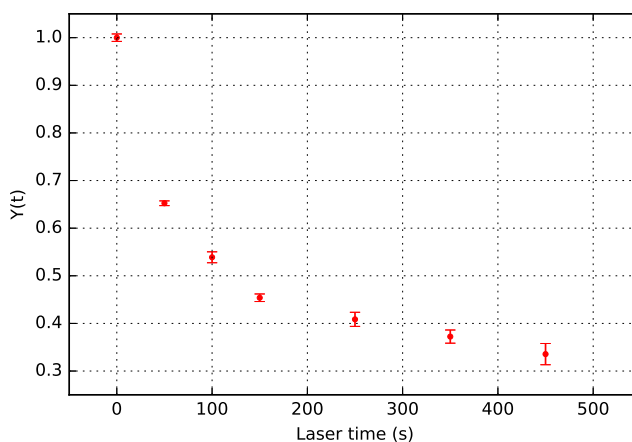
Figure 3.10: Decay curve of a frozen mixture of TEMPOL and ascorbic acid.

of about 360 K.

(B) From $T_{prepB} = 243$ K (the same as T_{prepA}), a laser power of 2.8 W is applied, letting the sample reach a T_{rB} of about 330 K. Given the lower T_r, a slower reaction is expected as compared to Experiment A.

(C) From $T_{prepC} = 263$ K, a laser power of 3.5 W is applied, letting the sample reach a T_{rC} of about 380 K. Given the higher Reaction Temperature, a faster reaction is expected as compared to Experiment A.
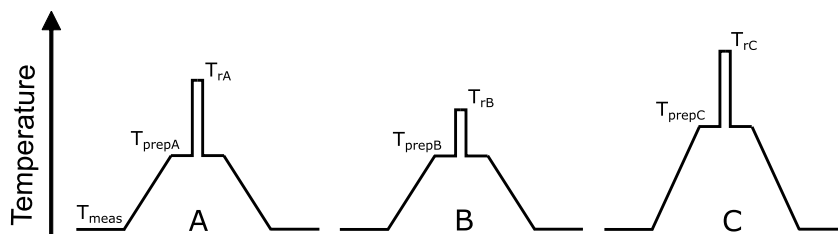

Figure 3.11: Scheme representing the steps of the flexibility experiment.

The Reaction Temperatures reported above are determined from the temperature calibration

described in the Appendix to this Chapter.

For Experiment B and C, decay curves were obtained similar to that of Experiment A, already shown in Figure 3.10, but with different decay times, as expected. As shown in Figure 3.12, experiments A, B, and C yield three distinct decays for frozen mixtures of TEMPOL and ascorbic acid with the same composition, confirming that kinetics at different Reaction Temperatures can be obtained with T-Cycle EPR by flexibly altering the Preparation Temperature and/or the laser power. Furthermore, it can be appreciated that the decay rates shown in Figure 3.12 are consistent with the experiment scheme of Figure 3.11: to a higher Reaction Temperature corresponds a faster kinetic decay, namely A and C faster than B, with T_{rA} and T_{rC} higher than T_{rB}.
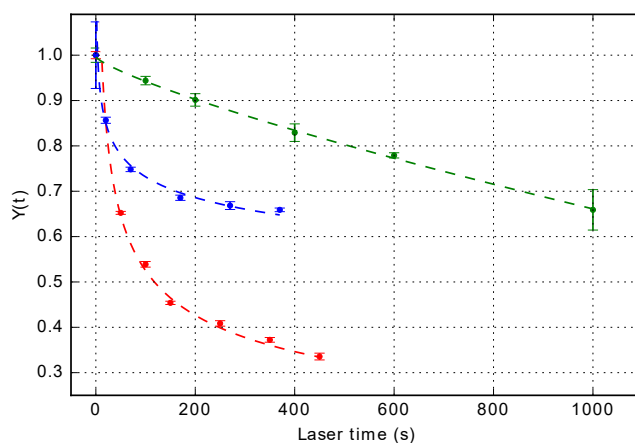
Figure 3.12: Decay curves obtained from Experiment A (red), B (green), and C (blue). The dotted lines are meant to guide the eye.

3.5 Discussion and conclusions

For the first time, the *in-situ* application of laser-induced T-jumps is coupled to high-frequency EPR (275 GHz) for the investigation of chemical kinetics. By taking as a model reaction the reduction of TEMPOL nitroxide by ascorbic acid, Temperature-Cycle EPR is shown to be an effective, versatile, and flexible method.

The first proof of T-Cycle EPR was applied on a time scale of minutes, yielding a characteristic

time of about 100 s. This result is corroborated by literature data, where decays of the TEMPOL-ascorbate system on the same time scale are reported [67] [69] [71] [72]. In these studies, the concentration conditions were such that the reaction exhibits a pseudo-first-order behavior; moreover, since the species actually responsible for the TEMPOL reduction is the ascorbate anion, the system was buffered so as to maintain a pH that maximizes the concentration of ascorbate rather than ascorbic acid. In the present work, neither pseudo-first-order conditions were employed, nor buffered solutions. Our aim was not that of achieving quantitative kinetic results, but rather that of showing the validity of the T-Cycle EPR method.

T-Cycle EPR allows a flexible temperature manipulation of the sample, whereby faster or slower kinetic behaviors can be obtained depending on the higher or lower Reaction Temperature reached. By selecting an appropriate Preparation Temperature (through the cryostat's temperature controller) and an appropriate laser power for the T-jump, the frozen sample reaches different Reaction Temperatures, and resultingly different decays are obtained. Depending on the composition of the solvent, T-jumps between 20 and 120 °C can be achieved, as described in the Appendix to this Chapter. This wide range of T-jumps makes it possible to study chemical kinetics unfolding at conditions different than room temperature, offering an advantageously flexible applicability of the T-Cycle method.

From the decays depicted in Figure 3.12, three different kinetics are obtained from experiments A, B, and C. These three experiments differ in the Reaction Temperature the sample reaches, namely T_{rA} and T_{rC} are higher than T_{rB}. The reduction of TEMPOL by ascorbic acid is an endothermic reaction [73], thus a slower decay is expected upon decreasing the Reaction Temperature. Consistently, the fastest decay is measured for experiments A and C, followed by experiment B.

In conclusion, this Chapter described the development of Temperature-Cycle EPR, a novel, versatile technique to study chemical kinetics and paramagnetic intermediates of (bio)molecular systems. Firstly, it was shown that T-Cycle EPR works in observing decays on time scales of minutes. Secondly, a series of experiments were designed to show that, by manipulating the Preparation Temperature and/or the laser power associated to the T-Cycle steps, different Reaction Temperatures are achievable, which makes T-Cycle a flexible and powerful technique for the investigation of (bio)molecular dynamics.

Important advantages of T-Cycle EPR are the use of only one sample to carry out a kinetic study, which does not pose limitations on the reproducibility of the sample preparation, and the need for only a small amount of material. Both characteristics are important features of T-Cycle

EPR, and are beneficial with respect to other methods that require larger amounts of materials and/or multiple samples, such as Rapid Freeze-Quench or flow methods.

The time scales described in this Chapter (of hundreds of seconds) were convenient as a first proof of the feasibility of the method, but are of limited applicabililty when investigating molecular processes that are not *ad-hoc* slowed down, such as most chemical kinetics and biochemical processes. However, since the T-Cycle method is based on laser pulses, it is in principle possible to downsize the time scales by several orders of magnitude, so as to achieve sub-second time scales that should give access to many biochemical processes.

3.6   Appendix

Azarkh and Groenen [24] characterized what temperature is possible to reach upon irradiating the cavity with an infrared diode laser operating at 1550 nm. Depending on the solvent composition, they reported T-jumps of over 50 °C with an appropriate laser power.
Characterizing the temperature reached by the sample is possible thanks to the fact that solutions of nitroxide radicals show significant spectral changes as a function of temperature. Such changes are related to the rotational correlation time, τ_c, of the molecule in its medium. An expression of τ_c is given by Equation 3.3, which is the rotational-diffusion equivalent of the Stokes-Einstein equation, commonly used in EPR studies [28]:

$$\tau_c = \frac{4\pi\eta r_0^3}{3k_B T} \tag{3.3}$$

with η and T being, respectively, the viscosity and the absolute temperature of the solution, r_0 the hydrodynamic radius of the diffusing molecule, and k_B the Boltzmann constant.
Since τ_c is a function of the viscosity and of the temperature of the solution, the high-frequency EPR intensity and shape variations of nitroxide radicals represent a good indicator of the temperature changes of solutions whose viscosity varies strongly with temperature. In particular, mixtures of water and glycerol exhibit a strong dependence of their viscosity on temperature [74], and are thus particularly suited to be used as solvents of nitroxide radicals for a temperature calibration of a T-Cycle experiment. Following is a characterization of the temperatures reached upon application of T-jumps on a solution of TEMPOL in a mixture of water and glycerol, with the setup described in Subsection 3.3.2. Such temperature calibrations are closely dependent on the setup used and, needless to say, on the composition of the sample and on the sample holder. The main factors to be taken into account are, among others, the model and connector of the diode laser and the optical fiber, the distance of the bare fiber's end from the cavity, and

the laser's power supply and cooling system. These elements all affect the effective amount of laser power that is absorbed by the sample, and therefore the final temperature reached during a T-jump.

Figure 3.13 shows the dependence on temperature (A) and on laser power (B) of the 275 GHz cw EPR spectrum of a TEMPOL solution (2 mM) in a mixture of water and glycerol 1:1 in volume. Interpretation of the 275 GHz EPR spectrum of TEMPOL is provided in Subsection 3.4.1; what is interesting to realize is the huge variation of the spectral shape as a function of temperature, here shown in the range between about -32 and +23 °C (Figure 3.13 A).
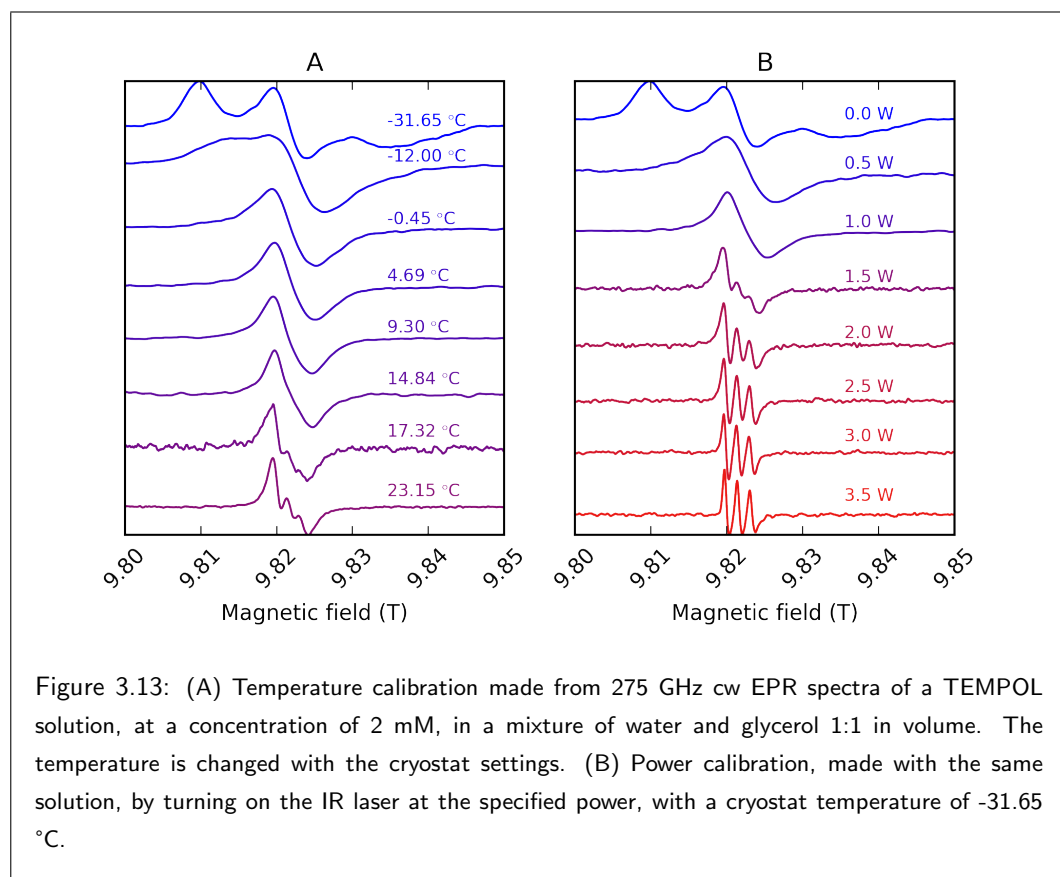
Figure 3.13: (A) Temperature calibration made from 275 GHz cw EPR spectra of a TEMPOL solution, at a concentration of 2 mM, in a mixture of water and glycerol 1:1 in volume. The temperature is changed with the cryostat settings. (B) Power calibration, made with the same solution, by turning on the IR laser at the specified power, with a cryostat temperature of -31.65 °C.

A temperature calibration is possible by considering that to each temperature corresponds a unique value of the ratio of viscosity and temperature, η/T, of a solution of given composition. This is shown in Figure 3.14 (red triangles), where tabulated values of η/T are plotted as a

function of temperature, for a mixture of water and glycerol 60% in weight [74].
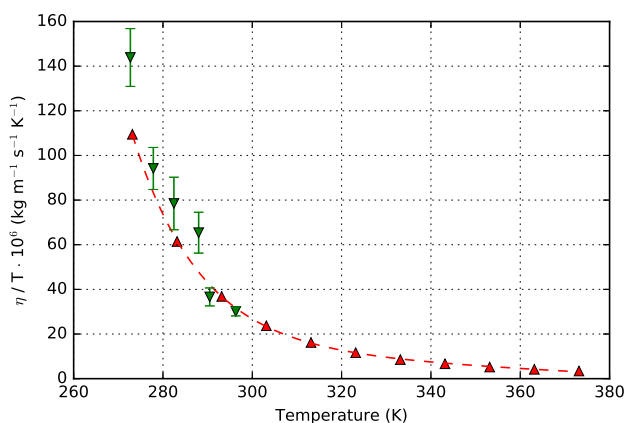
Figure 3.14: Values of η/T plotted versus T. Red triangles: obtained from [74] for a mixture of water and glycerol 60% in weight. Green triangles: obtained with Equation 3.3 from the EasySpin simulations of the spectra of Figure 3.13 A. The error bars are calculated from the error estimation on the τ_c calculated from the simulations.

Since there is a unique relation between η/T and T, the same must be true for η/T and τ_c, as expressed by Equation 3.3. By simulating the spectrum at 23.15 °C of Figure 3.13 A with EasySpin (v. 5.2.16, run on MATLAB Release 2017a) [31], a rotational correlation time $\tau_c = 100$ ps is found (in agreement with [24]). This value, together with a viscosity of 7.75 centipoise obtained from [74], are used to find the hydrodynamic radius to be $r_0 = 2.3$ Å with Equation 3.3, which is in agreement with the value ranges reported in the literature [75].

With a determined value of r_0, it is possible to obtain ratios of η/T from the EasySpin simulations of the spectra of Figure 3.13 A, and associate them to the corresponding temperatures. This is shown in Figure 3.14, where the green triangles (calculated from simulations) match quite well the red dots (tabulated). Note that the calculated points refer to a mixture of water and glycerol 50% in *volume*, which corresponds to $\sim$ 56% in *weight*, very close to the 60% weight composition of the tabulated data. In Figure 3.15 are shown the simulations run on the spectra of Figure 3.13 A.

Running EasySpin simulations on the spectra of Figure 3.13 B (as a function of nominal laser power) yields values of τ_c and, through Equation 3.3, ratios of η/T associated to each laser

Figure 3.15: EasySpin spectral simulations (on the right) of the 275 GHz EPR spectra (on the left) from Figure 3.13 A, as a function of temperature.

power. In Figure 3.16 are shown the simulations run on the spectra of Figure 3.13 B. By making use of the fitting (red dotted line) of the tabulated points of Figure 3.14, it is possible to turn the ratios η/T to values of temperatures, and associate them to the respective nominal laser powers. Calculation of the relative T-jumps is then straightforward, and their relation to the laser power is shown in Figure 3.17, where a linear trend is observed within the evaluated errors (which is consistent with what reported in [24] for T-jumps between 10 and 55 °C). T-jumps between roughly 20 to 120 °C can be obtained in the nominal power range between 0.5 to 3.5 W. It should be noticed that these values of T-jumps derive from the extrapolation of the experimental points of Figure 3.14 (green triangles) to higher temperatures, assuming they match the reference data points (red triangles of Figure 3.14).

It can be appreciated how faithfully the simulations of Figures 3.15 and 3.16 reproduce the experimental spectra, confirming that the model chosen here is appropriate. Table 3.2 summarizes the parameters fed to EasySpin for the simulations: while the main parameter that was varied to fit the simulations to the spectra was the τ_c, also the microwave frequency had to be slightly adjusted for each simulation – the latter in order to account for the magnetic field
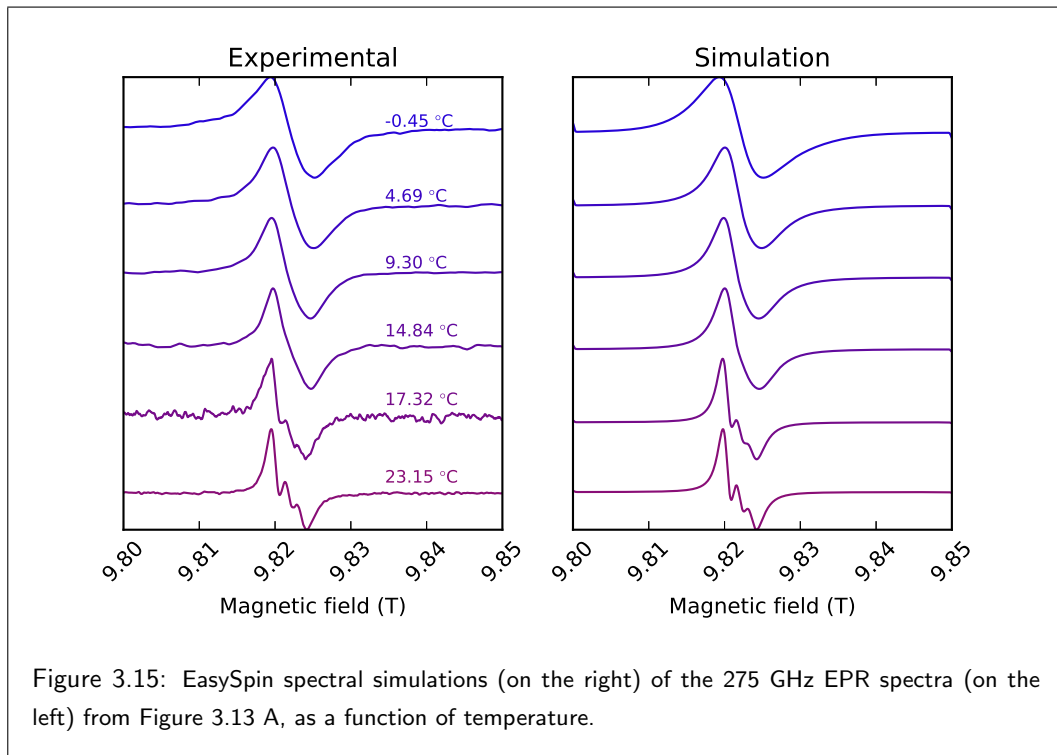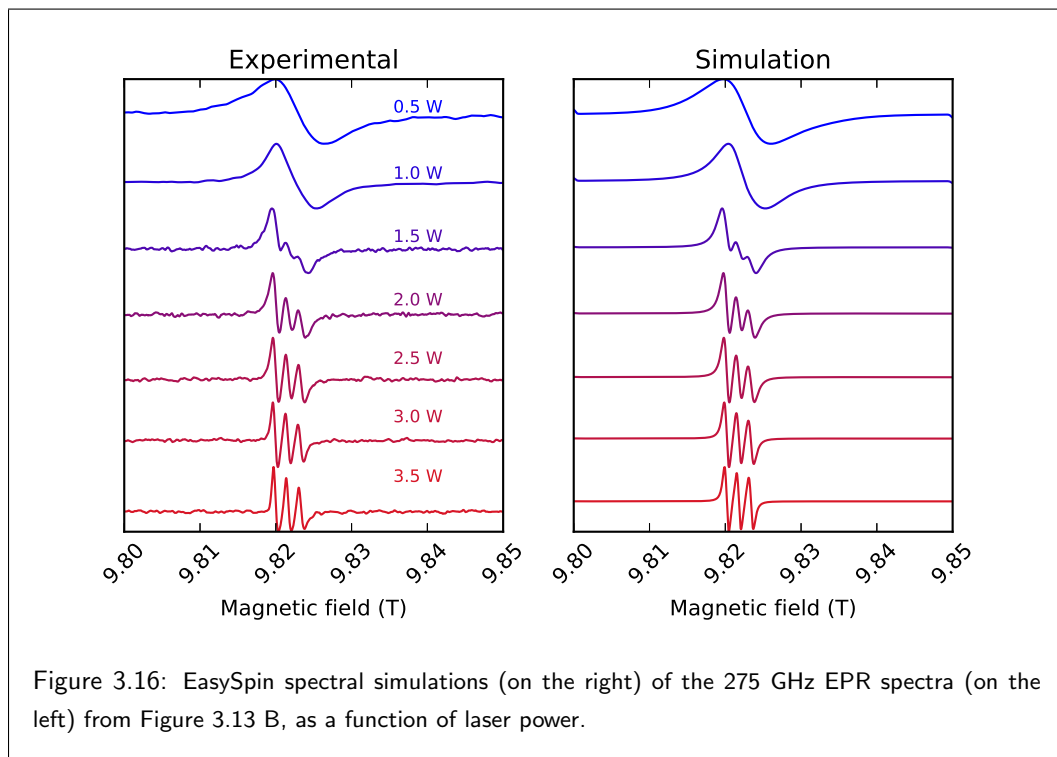
Figure 3.16: EasySpin spectral simulations (on the right) of the 275 GHz EPR spectra (on the left) from Figure 3.13 B, as a function of laser power.

shifts associated to each experimental scan. The peak-to-peak intrinsic linewidth mentioned in Table 3.2 is a parameter EasySpin requires in order to produce a smooth spectral output.

As a final remark, from Figure 3.13 it can be appreciated how the spectral linewidth decreases with increasing temperature or, equivalently, with increasing laser power. By defining what is here referred to as "partial linewidth", i.e., the full width at half maximum of the peak around 9.8195 T for the spectra of Figure 3.13 B, it is possible to obtain a measure of the line broadening of each spectrum. Notice that the partial linewidth can be unequivocally quantified only for the spectra that are not in the rigid-limit regime, namely – for the spectra shown here – from -0.45 °C onwards.

Since the partial linewidths are unambiguously associated to their corresponding laser powers, it is possible to link the T-jumps from Figure 3.17 – and therefore the temperature of the sample, taking into account the Preparation Temperature – directly to the partial linewidths, as shown in Figure 3.18. Partial linewidths can thus be translated to temperatures in a one-to-one relation, which allows the determination of the latter in a convenient manner, since measuring the spectra's partial linewidths is a much easier and more straightforward procedure than obtaining rotational
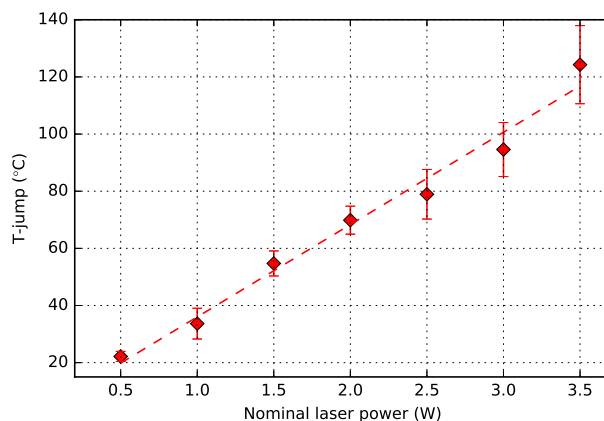
Figure 3.17: T-jumps as a function of the nominal laser power. The T-jumps are calculated from the fitting of the values of T versus η/T (see Figure 3.14), from the starting temperature of -31.65 °C. The error bars are calculated from the error estimation on the τ_c calculated from the simulations.

correlation times through simulations, or using the second-moment analysis described in [24].
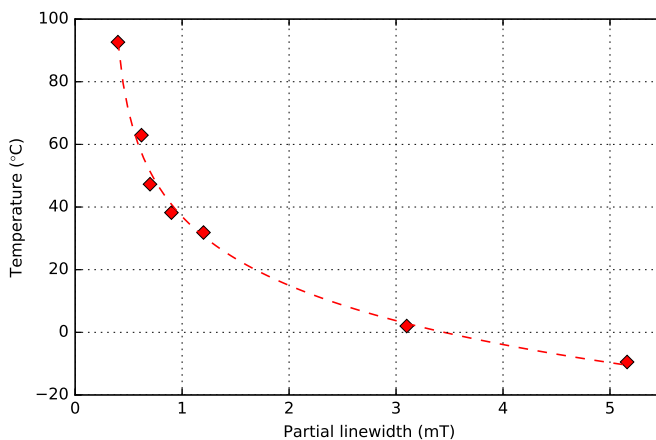
Figure 3.18: Relation between the sample temperature and the partial linewidth of the corresponding 275 GHz cw EPR spectrum. The dotted line is a guide to the eye.

Simulated spectrum	τ_c (ps)	μw freq. (GHz)
-0.45 °C	550 ± 50	275.75
4.69 °C	360 ± 36	275.75
9.30 °C	300 ± 45	275.74
14.84 °C	250 ± 35	275.74
17.32 °C	140 ± 15	275.725
23.15 °C	115 ± 7	275.725
0.5 W	600 ± 48	275.77
1.0 W	340 ± 54	275.76
1.5 W	130 ± 10	275.72
2.0 W	70 ± 5	275.72
2.5 W	50 ± 5	275.72
3.0 W	30 ± 3	275.72
3.5 W	15 ± 2	275.72

Table 3.2: EasySpin parameters of the simulations of the 275 GHz EPR spectra from Figures 3.15 and 3.16. The two parameters that are varied to adjust the simulation to the experimental spectrum are the rotational correlation time (τ_c) and the microwave frequency (μw freq.). The other parameters, kept fixed, are: field range, 9.8 ÷ 9.850 T; number of points, 1000; peak-to-peak intrinsic linewidth, 0.3 mT (taken 50% Gaussian and 50% Lorentzian); **g** tensor, [2.0083 2.0058 2.0030]; **A** tensor for ^{14}N, [18 18 99] (in MHz). The last two are taken from [24]. Notice that the microwave frequency is adjusted to compensate for the shifts in magnetic field, the largest totaling 1.8 mT.

4

Exploring Temperature-Cycle EPR in the sub-second time domain

4.1 Introduction

Being able to investigate chemical kinetics in the sub-second time domain gives access to a great deal of reactions of biological relevance, which occur in a broad range of time domains: from milliseconds to nanoseconds [23], and even down to femtoseconds [76]. Many are the techniques to determine kinetics on the time scale of milliseconds, most notably Rapid Freeze-Quench and flow methods; however, it is the IR-laser-induced temperature-jump techniques that allow – in principle – a considerable downsizing of the accessible time scales in molecular dynamics investigations.

In the previous Chapter, the Temperature-Cycle EPR method was introduced, and demonstrated on a model reaction occurring on a time range of minutes. Bringing about several advantages over other techniques, most importantly the need for one single sample per experiment and therefore the use of a small amount of material, a decisive improvement is needed as far as the time scales within reach are concerned. Since T-Cycle EPR is based on laser-induced T-jumps, in principle the duration of a T-jump can be scaled down by several orders of magnitude as compared to the minute-range obtained in Chapter 3, the main limitation being the heat conductivity of the solutions under study.

The present Chapter is devoted to the application of T-Cycle EPR on a model reaction that takes place over several hundreds of milliseconds, using a similar setup as described in the previous Chapter. A new hand-mixing method is described to easily and efficiently mix the reagents without them reacting. Furthermore, quantitative kinetics can be obtained provided an analysis of the sample's temperature profile during the laser pulse is performed, which also yields the effective reaction time per T-jump, and the dependence of the rate constant on temperature.

4.2 Experimental

4.2.1 Materials and setup

Oxygen-free mixtures of TEMPOL (4-hydroxy-TEMPO, Sigma-Aldrich, cat. n. 176141) and sodium dithionite ($Na_2S_2O_4$, sodium hydrosulphite 85%, Sigma-Aldrich, cat. n. 15,795-3) used for the T-Cycle experiments in this Chapter were prepared from batch solutions at concentrations of 2 and 100 mM, respectively, in a mixture of phosphate buffer and glycerol 1:1 in volume. In view of the high reactivity of sodium dithionite with oxygen [77], both the TEMPOL and buffer batch solutions, together with the sodium dithionite powder prior to dissolution, were bubbled with argon for at least one hour while kept in air-tight vials sealed with rubber septa caps, to

ensure a complete removal of oxygen. In order to transfer the buffer:glycerol solution into the vial containing the sodium dithionite powder, and to transfer the de-oxygenated solutions to the beaker for the mixing (see Subsection 4.2.3), a Hamilton air-tight syringe was employed.

The phosphate buffer solution had a concentration of 120 mM and a pH of 7.0, and was prepared from stock solutions of sodium phosphate monobasic (G-Biosciences, cat. n. RC-098) and sodium phosphate dibasic (Sigma-Aldrich, cat. n. S5136-1KG) dissolved in Milli-Q water; glycerol was purchased from Sigma-Aldrich (puriss., cat. n. 15523-1L-R).

Resulting concentrations of TEMPOL and sodium dithionite of 1 and 50 mM respectively were then obtained upon hand mixing with the special technique explained in Subsection 4.2.3.

$MnCl_2$ at a concentration of 10 μM was added to both solutions prior to mixing, to be used as an internal standard. Details on the practice of using Mn^{2+} as a standard are provided in Chapter 3.

The samples are introduced in the single-mode cavity of a pre-cooled home-built probe head in a similar way as described in Chapter 2 of this thesis. Like described in Chapter 3, the probe head is then inserted in the He-flow cryostat of a home-built 275 GHz EPR spectrometer at a measurement temperature of 243 K.

The T-Cycle setup is essentially the same one as described in Chapter 3, except for a few modifications, such as the multi-mode optical fiber (Thorlabs, model n. FG200LCC, 0.22 NA, core size 200 μm, HPSMA connector to the laser) and the 4.4-W diode laser (SemiNex Corp., model n. 15P-110, serial n. 7559). With this setup, the behavior of a solution of TEMPOL in a mixture of buffer and glycerol is reported in Figure 4.1 A as a function of nominal laser power, in the range between 0.5 and 4.4 W. By employing the relation between spectral "partial linewidth" and temperature illustrated in the Appendix to Chapter 3, it is possible to link the nominal laser power to the temperature reached by the sample, as shown in Figure 4.1 B (here, this is possible in the range between 2.0 and 4.4 W). With this arrangement, the maximum T-jump obtained is $\sim$ 60 °C at 4.4 W nominal laser power from a starting temperature of $\sim$ -30 °C, in contrast with a maximum T-jump of $\sim$ 120 °C at 3.5 W reported for the setup of Chapter 3.

Laser-induced T-jumps were applied with pulses of the length of either 50 or 100 ms. The pulse duration was controlled by an electronic clock that triggered the current fed to the diode laser. Since the rise and fall time of the laser-induced T-jump on the sample are long as compared to the duration of the pulses applied here, which therefore do not allow the system to reach a steady state, an analysis of the temperature profile of the sample during the T-jump is required in order to determine quantitative kinetics (see Subsection 4.3.2).
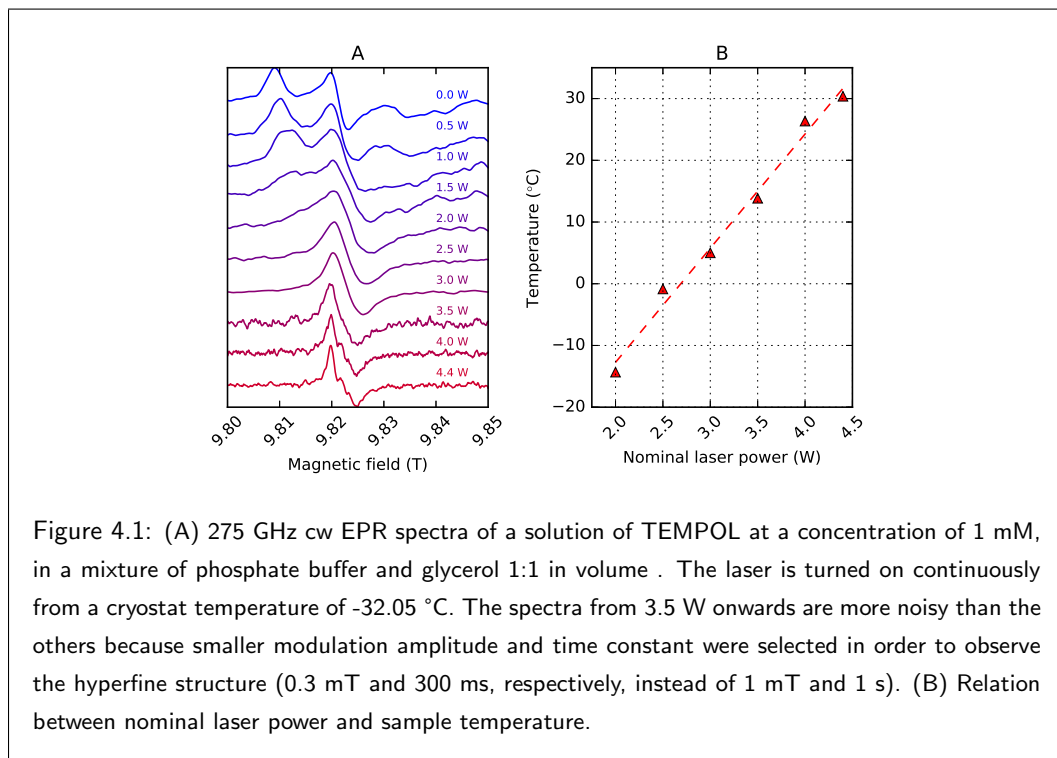
Figure 4.1: (A) 275 GHz cw EPR spectra of a solution of TEMPOL at a concentration of 1 mM, in a mixture of phosphate buffer and glycerol 1:1 in volume . The laser is turned on continuously from a cryostat temperature of -32.05 °C. The spectra from 3.5 W onwards are more noisy than the others because smaller modulation amplitude and time constant were selected in order to observe the hyperfine structure (0.3 mT and 300 ms, respectively, instead of 1 mT and 1 s). (B) Relation between nominal laser power and sample temperature.

The time profiles shown in Subsection 4.3.2 were obtained with an oscilloscope (LeCroy WaveSurfer 424), by measuring the 275 GHz EPR intensity of a solution of TEMPOL at the fixed magnetic field of 9.8197 T as a function of time, while applying laser pulses of a length of either 100 or 500 ms with a repetition time of 3 s. The oscilloscope window was set to 50 mV/div and 100 ms/div, and the signal was averaged 1600 times, because of the high noise level caused by the spectrometer's time constant of 3 ms used to record the time profiles. The TEMPOL solution was kept in the spectrometer's cryostat at a temperature of 243 K, at a concentration of 3 mM, in a mixture of glycerol and phosphate buffer (120 mM, pH 7.0), 1:1 in volume. The EPR parameters are the same as reported in Table 4.1; however, when recording a spectrum with the laser on, a smaller modulation amplitude and time constant were used, of 0.3 mT and 0.3 s, respectively.

The simulations shown in Section 4.4 were made with the COMSOL Multiphysics software (v. 5.3 a), performing a time-dependent study of the sample's temperature (0 to 1500 ms, with steps of 10 ms) with the package for heat transfer in fluids. To model the experimental conditions, a simplified geometry made up of an ensemble of five cylinders was created (see Figure 4.10).

Further details on their sizes and explanations on their meaning in the model are provided in Subsection 4.4.1. As far as the meshing is concerned, since the interesting temperature variations to simulate were those of the sample, the size of the meshing patterns were set differently for the sample cylinder ("Extremely Fine" mesh) as compared to the other cylinders ("Fine" mesh for the quartz cylinder, "Coarse" or "Normal" mesh for the helium cylinders inside the quartz, and "Extremely Coarse" mesh for the bigger helium cylinder). In all cases, the meshes were automatically generated with the program's "physics-controlled" algorithm. The physical properties as a function of temperature needed to perform the simulations (i.e., heat capacity at constant pressure, density, thermal conductivity, and dynamic viscosity) were taken automatically from the COMSOL Multiphysics library for quartz and helium; the properties of the mixture of water and glycerol 1:1 in volume had to be specified manually and were obtained from [74].

4.2.2 The TEMPOL-dithionite reaction

The reduction of TEMPOL by sodium dithionite is a well-established reaction employed in millisecond-scale kinetic EPR studies [78] [79] [66]. With a much higher concentration of sodium dithionite ($[S_2O_4^{2-}]$) over TEMPOL ($[TL]$), the reaction exhibits a pseudo-first-order behavior, as expressed in Equation 4.1 (after [66]):

$$\frac{d[TL]}{dt} = k' \cdot [TL] \tag{4.1}$$

$$k' = k \cdot [S_2O_4^{2-}] \tag{4.2}$$

with k' being the apparent rate constant. Sodium dithionite is known to undergo a dissociation equilibrium that produces the sulfonyl radical anion, $SO_2^{\bullet-}$, which gives a sharp EPR signal at $g = 2.0057$ [79]. Since the EPR signal of $SO_2^{\bullet-}$ overlaps with the g_y-component of the spectrum of TEMPOL around 9.82 T, the g_x-component around 9.81 T was chosen instead to follow the reaction.

4.2.3 Sub-zero mixing

Since the reduction of TEMPOL by dithionite unfolds within milliseconds, simple hand mixing of the two components at room temperature is not possible. A convenient feature of mixtures of pure water and glycerol is their low freezing point, which makes them highly viscous fluids at temperatures well below 0 °C [74]. Based on such property, for the experiments described in this Chapter a mixing method was devised, henceforth referred to as "sub-zero mixing", that

allows an effective and simple hand mixing of the solutions of TEMPOL and sodium dithionite at a temperature of roughly -50 °C, i.e., well below the temperature at which the mixture starts to react.

A 5-mL Pyrex beaker is kept inclined at about 45° and immersed in liquid nitrogen. A volume of 150 μL of one reagent is transferred into the inclined side of the beaker, as shown in Figure 4.2 A. Upon freezing of the solution, the beaker is inclined on the other side (while still being kept in liquid nitrogen), and a volume of 150 μL of the other reagent is transferred into that side, where it freezes. Care is taken to avoid the two solutions to ever be in physical contact, as shown in Figure 4.2 B. The beaker is then transferred in a setup very similar to that described in Chapter 2, namely a polystyrene box partly filled with liquid nitrogen, having a metal plate in it, secured on top of an octagonal polystyrene box. On the metal plate stands a 3.5-cm-high metal slab, on top of which is placed the 5-mL beaker containing the separated frozen solutions. By optimizing the level of liquid nitrogen in the polystyrene box (with a filling level of about 2 cm), and the flow of cold gaseous nitrogen blowing on the liquid nitrogen (which keeps the temperature immediately above the metal plate at about -50 °C), the metal slab stabilizes at a temperature of about -60 °C, and the frozen solutions in the beaker warm up from liquid-nitrogen temperature to about -50 °C. At this temperature, the solutions have a toothpaste-like texture, and can easily be mixed with a pre-cooled spatula. The reagents are thus efficiently mixed at a temperature where no reaction occurs (Figure 4.2 C).
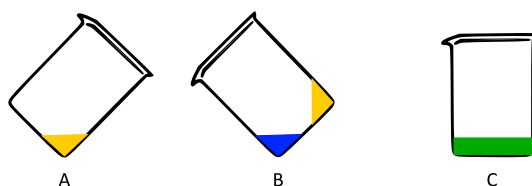
Figure 4.2: Scheme of steps for the sub-zero mixing. One reagent solution (depicted in yellow) is dropped on one side of the inclined beaker, where it freezes being at liquid nitrogen temperature (A). The other reagent solution (depicted in blue) is then dropped on the other side of the inclined beaker, and let to freeze (B). The beaker is finally placed on a metal slab, where it reaches a temperature of -50 °C, and it is possible to mix the two solutions (C).

Quartz capillaries connected to a syringe, prepared and handled in a similar way as described in Chapter 2 of this thesis, are then used to suck the cold mixture of reagents up to the silica-gel

filter in the capillary. Once filled, the capillary is transferred in a metal block (described in Chapter 2), and is then stored in dry ice for later measurements. The capillary is finally loaded in the pre-cooled spectrometer probe head following the procedure described in Chapter 2.

4.3 Results

This Section reports the 275 GHz cw EPR spectra obtained from applying the Temperature-Cycle method on a mixture of TEMPOL and sodium dithionite (experimental parameters are provided in Table 4.1), and the resulting subsecond-range decay. Similarly to Chapter 3, the spectral peak around 9.81 T was monitored, and the function $Y(t)$ was calculated versus time through normalization with the Mn^{2+} signal around 9.8408 T. See Chapter 3 also for the interpretation of the 275 GHz EPR spectra of TEMPOL. Whenever shown, error bars are calculated from the standard error on the four scans that are averaged. The standard error is calculated as follows:

$$e_n = \sqrt{\frac{1}{M_n} \sum_{m=1}^{M_n} (Y_{n,m} - \langle Y_n \rangle)^2} \tag{4.3}$$

where $Y_{n,m}$ is the value of Y for the m-th scan of the n-th point in time, $\langle Y_n \rangle$ is the averaged value of Y of the n-th point in time, and M_n is the total number of scans of the n-th point. Expressing the errors in this way represents the EPR intensity variation from scan to scan, which – except for a few points – outweighs the noise level.

Field range (T)	# of points	Mod. freq. (kHz)	Mod. ampl. (mT)	Time const. (s)	Conversion time (s)	Microwave power (μW)	T (K)
9.8 ÷ 9.855	1100	1.253	1.0	1	0.125	1.74	243

Table 4.1: Experimental parameters of the cw spectra at 275 GHz. *Mod. freq.* and *Mod. ampl.* are the field modulation frequency and amplitude, respectively.

4.3.1 Temperature-Cycle EPR on a sub-second time scale

In the experiment described here, Temperature-Cycle EPR is applied on a mixture of TEMPOL and sodium dithionite, prepared with the "sub-zero mixing" described in the previous Section. The sub-zero mixing ensures that the two reagents have not reacted during the mixing prior to exposure to the laser-induced T-jumps, so that the reaction is effectively observed from $t = 0$. Furthermore, the mixture is kept at a cryostat temperature of -30 °C, which prevents the reaction

to occur. A sequence of T-jumps, obtained by turning the laser on for a duration of either 50 or 100 ms at a nominal power of 4.4 W, is then applied on the mixture, and the reduction of TEMPOL by dithionite can be followed by measuring the 275 GHz EPR spectral intensity of the sample after each laser pulse.

The result is a decay of the 275 GHz EPR intensity of TEMPOL as a function of the laser time. As shown in Figure 4.3 A, a progressive decrease of the intensity of the TEMPOL spectrum is observed (red to fuchsia spectra), until no signal is detected anymore except for the lines from Mn^{2+}, thus showing that a spectral decay can be obtained when applying T-Cycle EPR with laser pulses of a duration well below the second. By plotting the $Y(t)$ function, calculated from the g_x spectral component of TEMPOL, an intensity decay can be observed on the laser-time axis up to 1850 ms, as shown in Figure 4.3 B. The five points after the first one in the decay of Figure 4.3 B correspond to laser pulses of a duration of 50 ms, while the later ones correspond to laser pulses of a duration of 100 ms.

Since the rise time of a T-jump lasts at least 300 ms (as described in Chapter 3), the system in the present experiment does not reach an equilibrium temperature during the time the laser is turned on. In order to determine the time that the sample effectively spends above a temperature where it starts to react, an analysis of the temperature profile of the sample during the application of a laser pulse is required.

4.3.2 Quantitative analysis of the sub-second kinetics

In Chapter 3 of this thesis, it was described how, upon turning the laser on for a relatively long time, it takes the sample at least 300 ms to reach an equilibrium temperature. In the experiments described in the present Chapter, however, the laser is turned on for a considerably shorter time (50 or 100 ms). The sample therefore does not have the time to reach an equilibrium temperature while the laser is on. This poses a twofold difficulty; firstly, on the actual time the sample spends at the reaction temperature, and secondly, on the definition of the reaction temperature itself, given that no steady state is ever reached during the T-jump. Hereinafter is the description of a method to determine the effective time that the sample spends at a temperature where the reaction occurs, upon application of a laser pulse of the duration of 100 ms. This method allows to calculate the reaction rate's dependence on temperature, and provides a way to estimate the reaction's activation energy. The idea at the basis of the method is that of assigning the EPR intensity variations of TEMPOL as a function of temperature (determined by recording a cw spectrum at different cryostat temperatures), to the intensity variations as a function of time (recorded with an oscilloscope), obtained by applying laser pulses of 100 ms on the sample. As
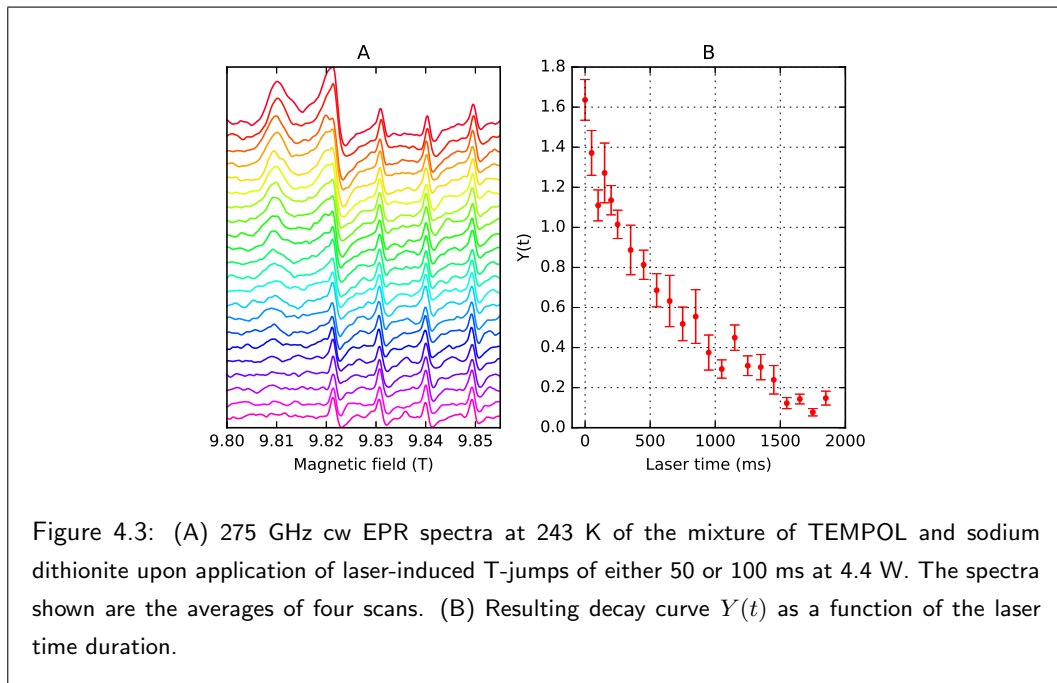
Figure 4.3: (A) 275 GHz cw EPR spectra at 243 K of the mixture of TEMPOL and sodium dithionite upon application of laser-induced T-jumps of either 50 or 100 ms at 4.4 W. The spectra shown are the averages of four scans. (B) Resulting decay curve $Y(t)$ as a function of the laser time duration.

a result, by taking into account the fact that the temperature of the sample changes during the application of the laser pulse (since an equilibrium temperature is not reached), the rate constant as a function of temperature can be modeled quantitatively, and the reaction's activation energy can be estimated. Furthermore, it is possible to determine the time that the sample effectively spends at a temperature at which the reaction takes place (which is shorter than the nominal 100 ms of the laser pulse application).

The 275 GHz EPR spectral changes of a solution of TEMPOL (in the absence of sodium dithionite) as a function of temperature are shown in Figure 4.4 A, where spectra are obtained at several cryostat temperatures in the range between $\sim$ -33 and +28 °C. Details about the causes of such behavior are provided in the Appendix to Chapter 3. By sitting on a fixed magnetic field, it is possible to plot the spectral intensity at that field as a function of temperature; this is shown for four different values of magnetic field in Figure 4.4 B. It can be appreciated how the EPR intensity at the field of 9.8197 T (blue triangles) is particularly sensitive to temperature variations in the range between $\sim$ -20 and +30 °C, as compared to the curves at other fields. This specific field value was thus chosen to characterize the temperature profile associated to the 100 ms laser pulse.
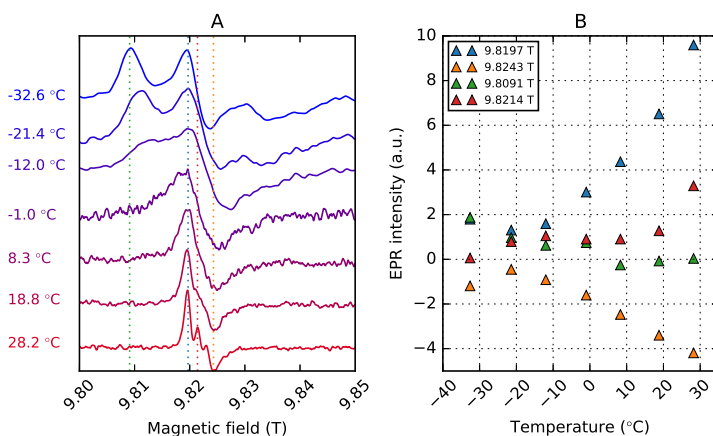
Figure 4.4: (A) 275 GHz spectra as a function of the cryostat temperature of a 1-mM solution of TEMPOL in a mixture of glycerol and phosphate buffer (120 mM, pH 7.0), 1:1 in volume. The colored dotted lines show the magnetic field values at which the spectral intensities are taken and plotted as a function of temperature, in (B). Notice that in (A) each spectrum is normalized within the range 0 to 1, while the intensities in (B) are from the actual experimental spectral intensities.

With an oscilloscope, the 275 GHz EPR intensity variation of a solution of TEMPOL at the fixed magnetic field of 9.8197 T was measured while applying 100 ms long laser pulses at a nominal power of 4.4 W. Figure 4.5 A shows the raw time profile (profile on top), the baseline time profile recorded at a magnetic field of 9.8 T (i.e., without an EPR signal, profile in the middle), and the difference of the two (profile at the bottom). The baseline correction is essential to obtain a time profile without the disturbance effects induced by the laser pulse on the spectrometer's cavity, which last even longer than the duration of the pulse itself. By comparing the corrected time profile of Figure 4.5 A (bottom) and the curve at 9.8197 T of Figure 4.4 B (blue triangles), a consistent trend can be appreciated; furthermore, it can be visualized that with a laser pulse of the duration of 100 ms the sample does not reach an equilibrium temperature, because the laser is switched off before an intensity plateau is attained.

In order to associate the EPR intensity variations at 9.8197 T from Figure 4.4 B (blue triangles) to the time profile of Figure 4.5 A (bottom), a comparison is made between the latter and a time profile with a longer laser pulse, which enables the sample to reach an equilibrium temperature. The green profile of Figure 4.5 B, obtained by applying laser pulses of 500 ms at the same nominal power of 4.4 W, shows that the sample reaches an equilibrium temperature
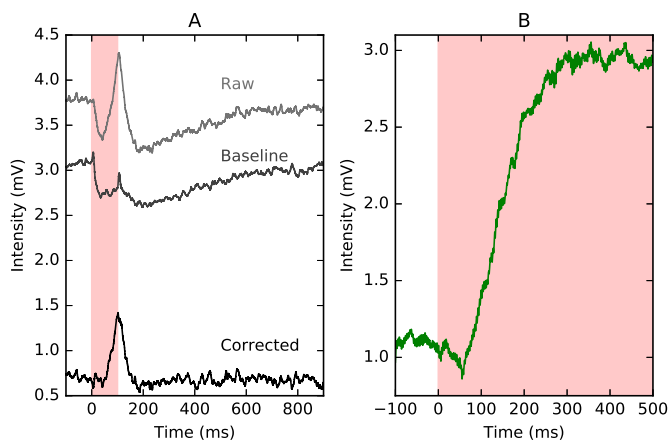
Figure 4.5: Time profiles of the 275 GHz EPR spectral intensity at the magnetic field of 9.8197 T of a 3-mM solution of TEMPOL in a mixture of glycerol and phosphate buffer (120 mM, pH 7.0), 1:1 in volume. (A) Upon application of 100 ms long laser pulses at a nominal power of 4.4 W. The raw time profile (light gray) is corrected by the baseline time profile (dark gray) recorded at the magnetic field of 9.8 T. (B) Upon application of 500 ms long laser pulses, at the same power. This time profile was corrected by the baseline time profile from (A).

after about 300 ms from the beginning of the laser pulse. The baseline profile corresponding to the green profile was not measured, so that the laser's disturbance effects on the cavity are partly visible at the beginning of the profile; however, the profile's baseline level was shifted by the baseline of the profile at 100 ms from Figure 4.5 A.

The equilibrium temperature corresponding to the intensity plateau of the 500 ms profile is straightforwardly obtained by measuring the cw EPR spectrum of the sample with the laser continuously on, which yields the spectrum A of Figure 4.6. The good match with the spectrum at +28.2 °C from the temperature calibration of Figure 4.4, reported as spectrum B in Figure 4.6, confirms the equilibrium temperature of the 500 ms pulse to be around +30 °C. Figure 4.6 also compares spectrum C, corresponding to the baseline of the time profiles of Figure 4.5 (recorded at -32.0 °C with the laser off) with the spectrum at -32.6 °C from the temperature calibration, here presented as spectrum D. Once again, the good match confirms the starting temperature of the profile of Figure 4.5 to be around -30 °C.

The baseline level of the profile of Figure 4.5 A (bottom) therefore corresponds to the intensity of the point at -32.6 °C of Figure 4.4 B (blue triangles); the value of this initial intensity is assigned
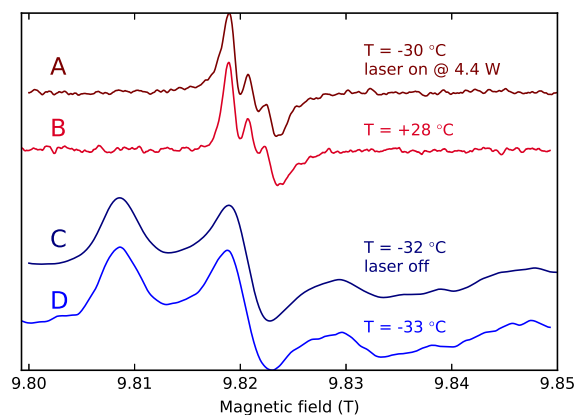
Figure 4.6: Comparison of 275 GHz spectra of TEMPOL in solution with a mixture of glycerol and phosphate buffer (120 mM, pH 7.0), 1:1 in volume. (A) and (C) correspond to the experiment shown in Figure 4.5, recorded, respectively, at a temperature of -30.2 °C with the laser continuously on at a nominal power of 4.4 W, and of -32.0 °C with the laser off. (B) and (D) correspond, respectively, to the first (at -32.6 °C) and the last (at +28.2 °C) spectrum of the temperature calibration of Figure 4.4.

to 1 mV in the scale of Figure 4.5. Moreover, the plateau of the green profile of Figure 4.5 B corresponds to the intensity of the point at +28.25 °C of Figure 4.4 B (blue triangles), i.e., to a value of about 3 mV in the scale of Figure 4.5. In this way, the curve at 9.8197 T of Figure 4.4 (blue triangles) can be overlaid on the profile of Figure 4.5 A, and the temperature variations can then be associated to the time scale, as shown in Figure 4.7. Although the points at -21.4 and -12.0 °C (depicted as white circles) can only be tentatively associated to the time profile because of the noise level, the points from -1.0 to +18.8 are matching well the intensity change of the time profile within the laser pulse, and are linearly related to the initial point at -32.6 °C. The inset of Figure 4.7 shows the linear behavior of these temperatures as a function of the time of the laser pulse.

In order to understand how long a time interval the sample spends at temperatures at which the reaction actually takes place within the time scale of milliseconds, a slower decay of the reduction of TEMPOL by dithionite is considered. Although the experimental conditions employed to obtain this decay are the same as described in this Chapter, the T-Cycle setup was different, namely different models of the optical fiber, diode laser, and fiber connector were used

Figure 4.7: Corrected time profile from Figure 4.5, with the temperature curve of Figure 4.4 (blue triangles) overlaid on it. The inset shows the linear relationship between the temperature of the sample and the time of the laser pulse. Note that the points corresponding to the temperatures of -21.4 and -12.0 °C, shown as white circles, cannot be assigned to the time profile because of the noise level; for this reason they have been excluded from the linear regression of the inset.
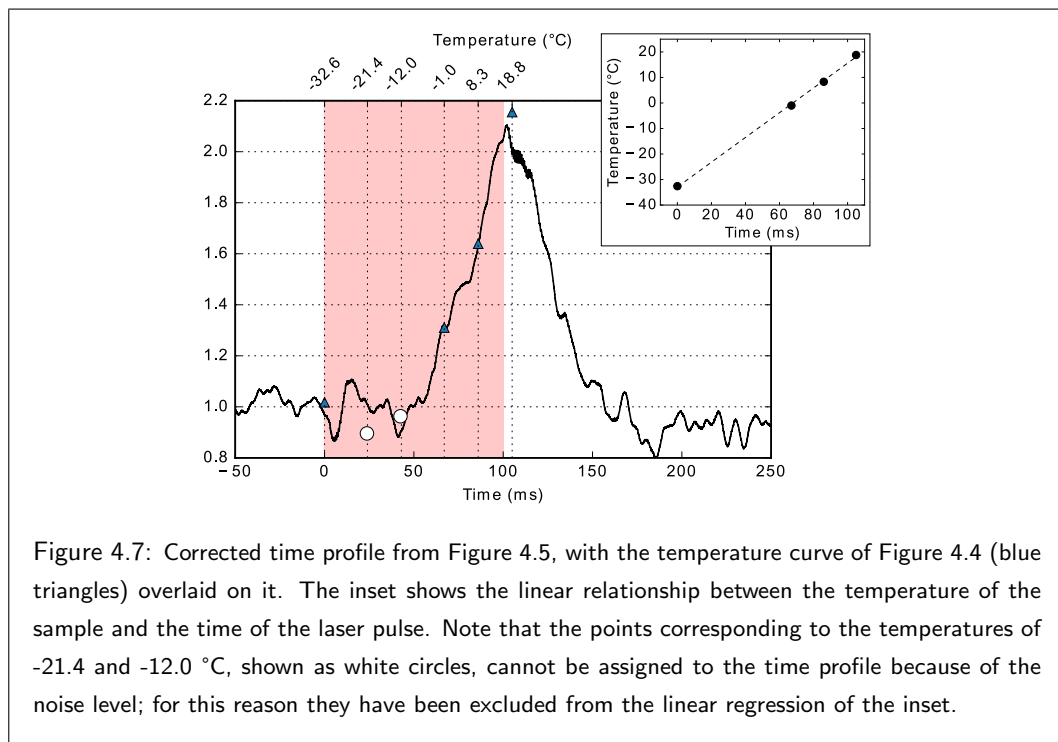
as compared to those reported here.

Figure 4.8 A reports such decay, showing a complete depletion of the TEMPOL signal within 40 s, upon application of laser pulses of the duration of 5 s (20 s for the last point) at a nominal power of 2.0 W. Since the laser pulses are much longer than the rise time, at each point the sample does reach a steady temperature which is also the reaction temperature, determined to be ~ 8 °C by comparing the spectrum of a solution of identical composition (but without sodium dithionite) with the laser continuously on (a in Figure 4.8 B), with the spectrum at 8.3 °C from the temperature calibration of Figure 4.4, here shown as spectrum b. Figure 4.8 B also compares the spectrum of the sample at the starting temperature of -30 °C (spectrum c) with the one at the same temperature from the temperature calibration (spectrum d), showing a good match and thus confirming the starting temperature. From the fit of the decay of Figure 4.8 A, a rate $k(8°C) = 2.0 \pm 0.2$ M^{-1} s^{-1} is calculated.

The time interval that the sample spends at a temperature greater than or equal to 8 °C appears to be about 40 ms from Figure 4.7. With the aforesaid rate at 8 °C of 2.0 M^{-1} s^{-1}, the intensity change of the TEMPOL signal is less than 1% within the time window of 40 ms.
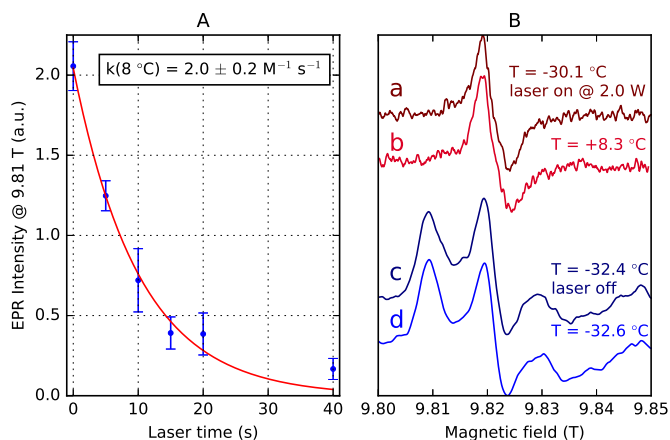
Figure 4.8: (A) Decay obtained by applying T-Cycle EPR on a mixture of TEMPOL and sodium dithionite of identical composition as for the decay of Figure 4.3. The laser pulses are applied with a duration of 5 s (or 20 s, for the last point) at a nominal power of 2.0 W, with the sample sitting at a cryostat temperature of 243 K. (B) Spectra comparison of: (a) a solution of identical composition as that of the decay (except for sodium dithionite), with the laser continuously on at 2.0 W; (b) the spectrum at 8.3 °C from the temperature calibration of Figure 4.4; (c) solution giving the decay shown in (A), before applying the laser pulses, at a cryostat temperature of 243 K; (d) the spectrum at -32.6 °C from the temperature calibration of Figure 4.4. Notice that for (A), and thus for spectra (a) and (c), the T-Cycle setup used was different with respect to the optical fiber, diode laser, and fiber connector used in this Chapter.

The temperatures responsible for the sub-second decay observed in Figure 4.3 must therefore be higher than 8 °C. Within 40 ms, the sample goes through increasing temperatures, with corresponding faster rates, all contributing to an average rate constant, $\langle k \rangle$, responsible for the observed decay. By taking 40 ms as the effective duration of the T-jump produced by a laser pulse of 100 ms, a new time axis is generated, with a decay up to 650 ms, as shown in Figure 4.9, where the logarithm of the $Y(t)$ function from Figure 4.3 B is plotted versus the reaction time. Since the first five points from Figure 4.3 B correspond to laser pulses of 50 ms, while the remaining ones correspond to laser pulses of 100 ms, it is the last of the 50 ms points to be taken at $t = 0$. The resulting rate constant is calculated to be $\langle k \rangle = 71 \pm 6$ M^{-1} s^{-1}. Notice that varying the length of the time window by $\pm$ 10% leads to variations of $\langle k \rangle$ within the calculated error of $\pm$ 6 M^{-1} s^{-1}.

Figure 4.9: Semi-logarithmic plot of the decay of the mixture of TEMPOL and sodium dithionite. The time axis is obtained considering 40 ms as the effective duration on which the reaction takes place. The point at $t = 0$ of this plot is the last one at 50 ms laser pulse from Figure 4.3 B, while all the other points here were obtained from 100 ms laser pulses.
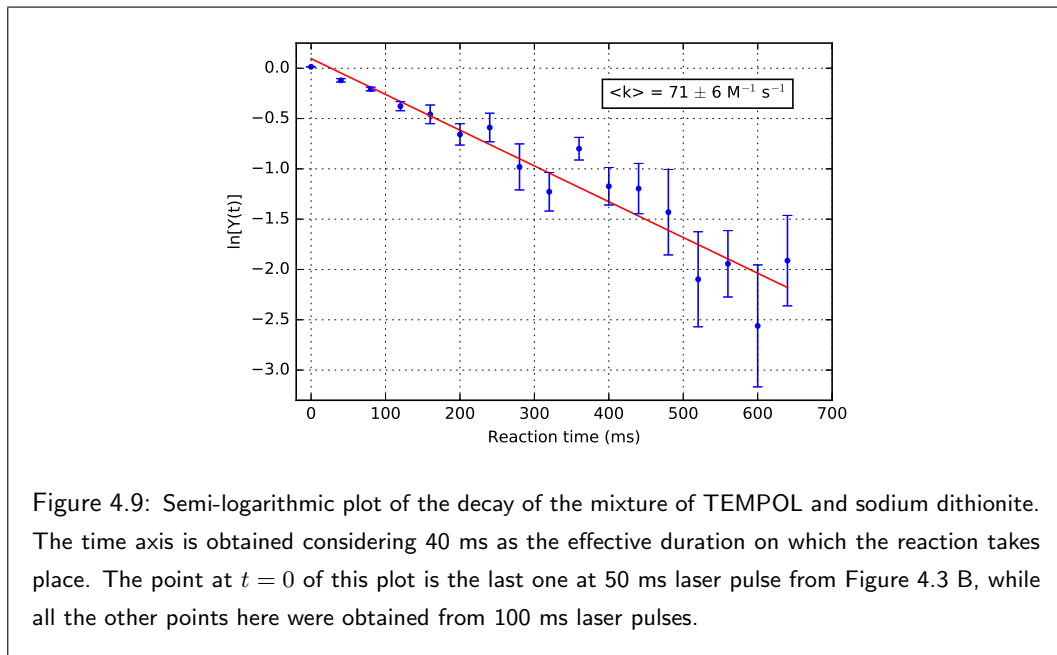
The average $\langle k \rangle$ can be modeled as follows. Firstly, the time interval $\Delta t = 40$ ms that the sample spends at a temperature greater than or equal to 8 °C is divided into n time elements δt, for whose length the sample's temperature can be considered constant. After each successive element, the decay of the 275 GHz EPR intensity of TEMPOL can be expressed as:

$$I_1 = I_0 e^{-k_1' \delta t}$$
$$I_2 = I_1 e^{-k_2' \delta t} = I_0 e^{-(k_1' + k_2') \delta t}$$
$$\vdots$$
$$I_n = I_0 e^{-(k_1' + k_2' + \ldots + k_n') \delta t} = I_0 e^{-\frac{1}{n}(\sum\limits_{i=1}^{n} k_i') \Delta t} = I_0 e^{-\langle k' \rangle \Delta t}$$

(4.4)

where $\Delta t = n\delta t$ is the total time interval (40 ms in this case). The average apparent rate constant is thus defined as $\langle k' \rangle = \frac{1}{n} \sum\limits_{i=1}^{n} k_i'$, from which the average rate constant is calculated through Equation 4.2 as $\langle k \rangle = \frac{\langle k' \rangle}{[S_2 O_4^{2-}]}$.

Secondly, knowing $k(8°C) = 2$ M^{-1} s^{-1}, and guessing an initial value of $k(19°C)$, it is possible to calculate $k(T)$ at the intermediate temperatures defined by the time elements δt,

assuming the $k(T)$'s behave according to the Arrhenius equation. By making the time step δt small enough so that temperature does not change during it, it is possible to calculate a set of $k(T)$ for each guess of $k(19°C)$, by linearizing the Arrhenius equation between $k(8°C)$ and $k(19°C)$. Through the linear relation between temperature and time shown in the inset of Figure 4.7, it is found that during a time interval $\delta t = 1$ ms the temperature changes by about 0.5 °C, which results in a negligible change in the rate constant at that δt, confirming that 1 ms is indeed a small enough time element. In this way, the value of $k(19°C) = 166 \pm 15$ M^{-1} s^{-1}, which yields the same average rate as that of the plot of Figure 4.9 (i.e., $\langle k \rangle = 71$ M^{-1} s^{-1}), is found after applying the aforesaid calculations for a couple of iterations. The value of the activation energy can thus also be calculated, and is found equal to $E_a = 280 \pm 14$ kJ mol^{-1}.

4.4 Discussion

Building on the achievements described in Chapter 3, Temperature-Cycle EPR is here taken a step further in investigating chemical kinetics on the sub-second time scales. The decay of the reduction of TEMPOL by dithionite is observed over a total laser time of 1850 ms with 275 GHz EPR, by application of laser pulses of 4.4 W nominal power and a duration of 100 ms. The decay time observed here is significantly shorter as compared to those of Chapter 3. As opposed to the experiments of Chapter 3, where the pulses applied are long enough for the sample to reach an equilibrium temperature, in the current study the pulses are much shorter, so that the system never reaches a steady state during the time the laser is on, but rather it goes through a temperature gradient during and after each laser pulse. On account of this, a quantitative analysis is performed on the temperature profile of the sample as a function of time, both during and after the application of a 100 ms long laser pulse. As a consequence, it is possible to determine a time window of about 40 ms per laser pulse within which the reaction takes place at temperatures higher than 8 °C; this results in a total effective laser time of 650 ms, constituting an improvement on the time resolution of the Temperature-Cycle technique of two orders of magnitude as compared to the time scales of Chapter 3. Furthermore, following such analysis it is possible to calculate the kinetic parameters of the reaction, such as the corresponding activation energy, and the rate constant as a function of temperature.

Corroboration of the analysis above comes from the comparison of the rate constant obtained here with those found in the literature for the reaction of TEMPOL and dithionite, in similar conditions as those reported here. Goldfarb *et al.* [66] reported a complete depletion of TEMPOL by dithionite to occur within 60 ms at room temperature, with a rate constant $k(RT) = 800 \pm 100$ M^{-1} s^{-1}. The most important difference between the conditions of the

present Chapter and those of [66] is the amount of glycerol in the solution, being 30% in volume there, while 50% in volume here. Further, in [66] a comparison is made with the $k(RT) = 4000$ M^{-1} s^{-1} extracted from other works for the same system [78] [79], except for the absence of glycerol in the solution. From this literature data, a 5-fold decrease of the rate constant is observed when going from 0% to 30% glycerol (i.e., from 4000 to 800 M^{-1} s^{-1}). In the present Chapter, another 5-fold decrease is found (i.e., from 800 to 166 M^{-1} s^{-1}), in the presence of 50% glycerol – namely, about a factor of 2 as compared to the conditions from Goldfarb *et al.*. The value of $k(RT)$ found here is thus most reasonable as compared to the literature data, which supports the analysis performed.

It is evident from the temperature profile as a function of time following the application of a laser pulse (Figure 4.7, and also Figure 3 of Chapter 3) that the temperature decay takes a longer time than the temperature rise. This asymmetry is understandable considering that during the temperature rise, the process of laser absorption adds on the active cooling constantly acting on the sample. The sample cooling is a process determined by the thermal conductivity of the sample itself and of the medium surrounding it, namely the quartz capillary and the helium gas, which slow down the rate of the heat transfer from the sample to the environment. A limit of the T-Cycle technique in its current state is thus the heat transfer rate of the system, acting both on the heating and on the cooling of the sample following a laser pulse. Such limitation may however be lessened, as discussed below.

Improvements both on the rise and fall time of the temperature profile can be envisioned. The former can be shortened by designing a different cavity within the probe head for the 275 GHz EPR spectrometer: the current one is basically a metal cylinder featuring a grid-like bottom part that blocks a portion of the incoming beam directed onto the sample, so that only parts of the sample effectively absorb the laser. An IR-transparent dielectric cavity without such a grid-like bottom could make the laser absorption more efficient, as the whole sample would directly be irradiated by the laser beam. Also the cooling time could be reduced by acting on experimental aspects such as the sample volume and the temperature difference between the sample and the bath. By shrinking the former and/or increasing the latter, a more efficient heat transfer is to be expected, and thus a faster recovery of the temperature after the laser pulse.

4.4.1 Modeling of the temperature decay following a laser pulse

In order to verify the considerations mentioned above, namely whether reducing the size of the sample volume and/or increasing the ΔT of the T-jump may accelerate the cooling process, the physical system of the present Chapter was modeled and simulated using the COMSOL

Multiphysics software (see technical details in Subsection 4.2.1). The geometry of the model was implemented with five cylinders, and is shown in Figure 4.10:

- A cylinder made of helium, much bigger than the sample size, acting as a thermal bath that simulates the cryostat;

- A much smaller cylinder made of quartz, placed in the center of the helium cylinder, representing the portion of the capillary used as a sample holder for 275 GHz experiments that is located in the spectrometer's cavity, and in the proximity thereof;

- A cylinder made of a mixture of water and glycerol 1:1 in volume, put inside the quartz cylinder, and representing the sample;

- Two cylinders made of helium, placed inside the quartz cylinder and at the two sides of the sample cylinder, used as a filling to avoid the quartz cylinder to be a solid quartz block.

The temperature at $t = 0$ of all the cylinders was set to either 243 K or 223 K, except for the sample cylinder whose temperature was set to 303 K.

Two major simplifications were made in the model, with the purpose of simplifying the complexity of the system and saving computational time. First, no active cooling of the bath was taken into account, but rather a large volume of helium gas was created, containing the sample (of much smaller volume) at its center; refer to Figure 4.10 for the geometry used in the simulations. The volume of the helium gas used as a thermal bath ($\sim$ 20 mL), much larger than that of the sample ($\sim$ 35 nL), ensures that the temperature of the bath is maintained at 243 K (or 223 K), as the sample cools down from the initial temperature of 303 K. The second simplification regards the initial temperature of the quartz containing the sample, and the helium gas inside the quartz, on both sides of the sample: in the simulations their temperature at $t = 0$ was set equal to that of the outer helium bath; nonetheless, more realistically a temperature gradient is present through the walls of the quartz capillary, and along the helium gas directly in contact with the sample. However physically inaccurate these two simplifications might be, in consideration of the degree of accuracy needed for the present study, they actually represent a minor deviation from the physical processes of interest here, and they allow a beneficially shorter calculation time.

Figure 4.11 shows the output of four different cases simulated with COMSOL Multiphysics, namely the sample diameter being either 150 or 75 μm (A, C and B, D respectively), and the temperature of the bath being either 243 K or 223 K, thus the ΔT being either 60 K or 80 K

Figure 4.10: Geometry of the model used to calculate the temperature profiles of Figure 4.11 with the COMSOL Multiphysics software. (A) Cylinder of helium (diameter 30 mm, length 25 mm), having the sample in its center, shown enlarged in (B) and (C). (B) Quartz capillary (total diameter 250 μm, thickness 50 μm, length 10 mm) with water and glycerol 1:1 in volume as the sample, highlighted in purple (diameter 150 μm, length 2 mm). (C) Same as (B), but the quartz capillary thickness is 87.5 μm, so that the sample diameter is 75 μm.

(A, B and C, D respectively). The sample's temperature decay from the initial value of 303 K is calculated for each mesh point of the sample cylinder; since both the surface points and the inner points are evaluated, and the former are subject to a faster cooling than the latter, the result is a temperature decay represented as a band in the plots of Figure 4.11. When comparing plot A with B, and C with D, a shortening of the cooling time is observed, as a result of a four-fold decrease of the sample volume. Similarly, when comparing plot A with C, and B with D, a shortening of the cooling time is observed resulting from an increase of the ΔT between the sample and the bath. To better illustrate these temperature decays quantitatively, Table 4.2 summarizes the average time it takes, in each case, for the sample cylinder to reach the temperature of 270 K from 303 K. The most dramatic effect can be appreciated when the sample diameter is reduced by half: for both ΔT considered, the cooling time becomes about five times shorter. Also changing the ΔT from 60 to 80 K reduces the cooling time significantly (of about two times), for both sample diameters considered.
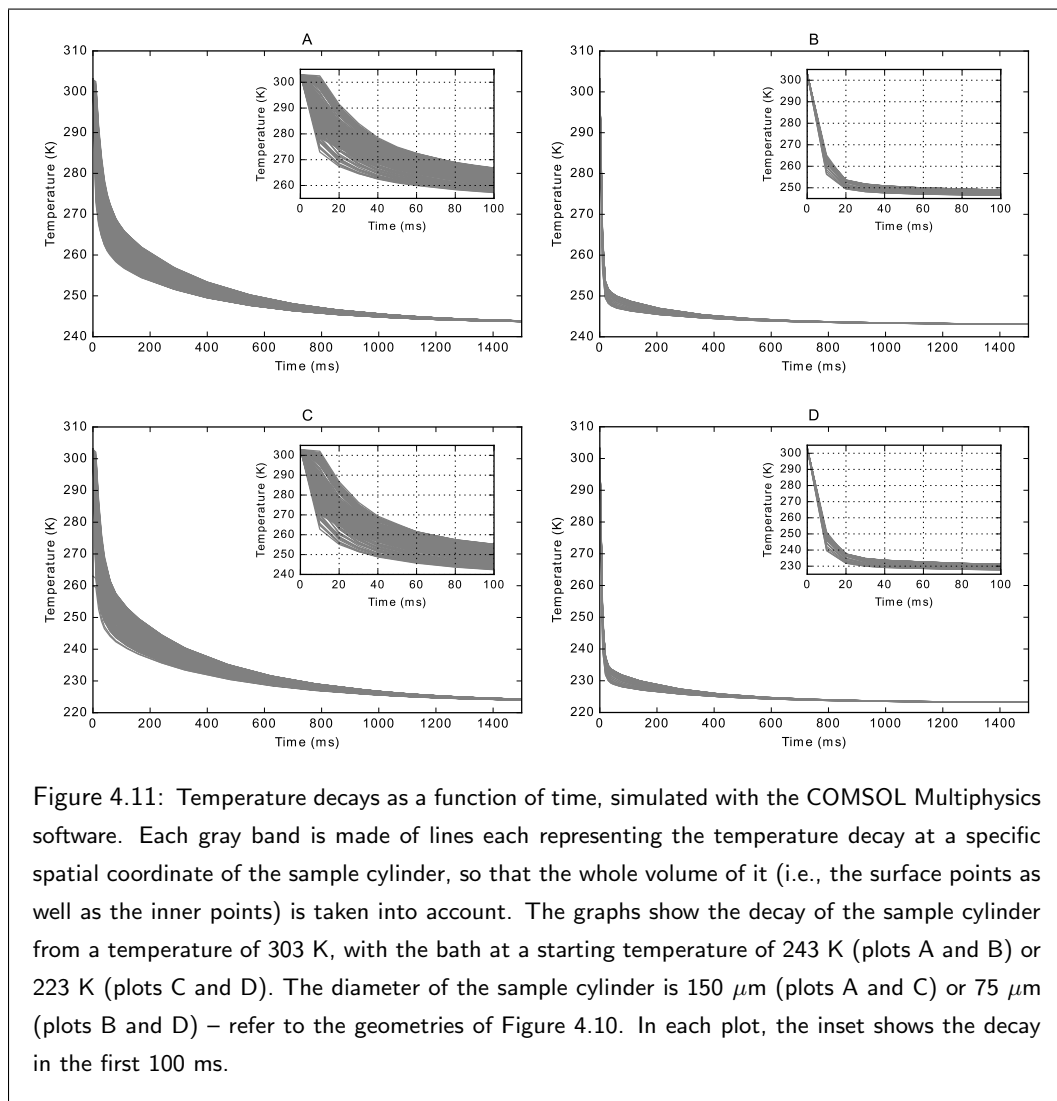
Figure 4.11: Temperature decays as a function of time, simulated with the COMSOL Multiphysics software. Each gray band is made of lines each representing the temperature decay at a specific spatial coordinate of the sample cylinder, so that the whole volume of it (i.e., the surface points as well as the inner points) is taken into account. The graphs show the decay of the sample cylinder from a temperature of 303 K, with the bath at a starting temperature of 243 K (plots A and B) or 223 K (plots C and D). The diameter of the sample cylinder is 150 μm (plots A and C) or 75 μm (plots B and D) – refer to the geometries of Figure 4.10. In each plot, the inset shows the decay in the first 100 ms.

From the simulations shown above it thus appears that it is possible to improve the current T-Cycle technique as far as the time for the cooling of the sample is concerned, at least by acting on two factors. One is the reduction of the sample volume, and therefore the increase of the thickness of the capillary walls; this, however, comes at the cost of a smaller signal, which might constitute a problem for low-concentrated samples. Moreover, reducing the sample diameter implies having a shorter optical path for the laser absorption, which might result in a less efficient laser-induced heating, as the sample's absorbance scales with the path length

ΔT	$d = 150\ \mu$m	$d = 75\ \mu$m
60 K	$\langle t_A \rangle = 44$ ms	$\langle t_B \rangle = 8$ ms
80 K	$\langle t_C \rangle = 23$ ms	$\langle t_D \rangle = 5$ ms

Table 4.2: Variations of the average time ($\langle t \rangle$) it takes the sample to reach the temperature of 270 K starting from 303 K, by changing two parameters in the simulations: the diameter (d) of the sample cylinder, and the temperature difference (ΔT) between the sample and the bath. The subscripts A, B, C, and D refer to the plots of Figure 4.11, where the $\langle t \rangle$'s are taken from.

according to the Lambert-Beer law. The other factor is the increase of the ΔT between the sample and the bath, or, in other words, the increase of the T-jump. Both factors contribute to a significant reduction of the cooling time of the sample, which thus in principle enables an even better time resolution.

4.5   Conclusions

In this Chapter, the reaction time scale accessible by Temperature-Cycle EPR was downsized to a few hundreds of milliseconds, rendering this technique apt for kinetic and dynamic studies of a great deal of chemical and biological processes. Starting from the time scale of minutes achieved in Chapter 3, where characteristic times of about 100 seconds were attained, a much faster decay was shown here, with a characteristic time of less than 300 milliseconds, which constitutes an improvement of two orders of magnitude. In addition to the increased time resolution of the method, the analysis of the time profiles of the sample's temperature upon application of a laser pulse leads to the determination of the reaction's kinetic parameters, namely its activation energy and the rate constant as a function of temperature. Furthermore, the feasibility of manual mixing of the reagents at temperatures well below 0 °C represents an attractive alternative to other techniques, such as Rapid Freeze-Quench or flow methods.

In its current state, Temperature-Cycle EPR offers the advantages of high-frequency EPR (such as high spectral resolution, and high sensitivity) with a time resolution already optimal for a wide range of (bio)chemical systems. Given the reaction time window of about 40 ms with which it is possible to follow a kinetic process with the present setup, a reaction with a characteristic time as short as 100 ms would be perfectly within reach. Additionally, in studies whose goal is the investigation of the evolution of paramagnetic reaction intermediates rather

than quantitative kinetics, the present setup can be employed in the time regime of tens of milliseconds.

However powerful the T-Cycle technique already is in the present, there is room to substantial improvements, particularly regarding the time resolution attainable. By acting on certain experimental parameters, such as reducing the sample volume and/or increasing the temperature difference between the sample and the cryostat, the result is a more efficient heat transfer, which is the main limitation in the cooling phase of the sample, and thus a shorter reaction time per laser pulse. Calculations performed on a model system suggest that the cooling of the sample could occur one order of magnitude faster if the sample diameter is halved as compared to the current setup, and the temperature of the cryostat is set 20 °C lower. An improved heat transfer, however, represents an obstacle to the heating of the sample, which could anyway be circumvented by devising a setup that allows a more efficient light absorption by the sample, such as a probe head with an IR-transparent dielectric cavity without a grid-like bottom that blocks part of the laser beam.

As an outlook for future developments on T-Cycle, the following considerations are advanced. With the laser-induced T-jump of $\sim$ 50 °C of the present Chapter, the temperature of $\sim$ 19 °C is reached within 100 ms. Since the increase in temperature is linear with time during a laser pulse, with a laser-induced T-jump twice as big (100 °C, shown to be possible in Chapter 3), the same temperature would be reached in as little as 50 ms, to which corresponds an even shorter reaction time per pulse. Although dealing with faster reactions might pose a challenge in terms of the manual mixing of the reagents with the method described in this Chapter, the combination of a more efficient laser absorption with a more efficient cooling of the sample can open the doors for T-Cycle EPR to kinetic investigations in time regimes of a few tens of milliseconds, if not less.

5

Venturing on the reoxidation of T1D SLAC with Temperature-Cycle EPR

5.1   Introduction

Temperature-Cycle EPR is a novel technique recently proven to be robust and flexible in the investigation of chemical dynamics down to the millisecond time domain. In the previous Chapters the method was demonstrated by employing well-understood, simple chemical reactions involving the reduction of a nitroxide radical. Given the successes achieved, an attempt to pioneeringly apply Temperature-Cycle EPR to the study of a biologically relevant enzymatic system on the sub-second time scale is presented here.

Multi-Copper Oxidases (MCO) are oxygen-reducing enzymes deriving their name from the four copper ions they use to promote the 4-electron reduction of O_2 to H_2O, while oxidizing a broad catalog of diverse substrates [80]. In particular, laccases are a group of multidomain MCOs that catalyze the oxidation of aromatic substrates, most notably phenols. They are ubiquitously found in nature, performing physiological roles in a wide range of organisms, and find (bio)technological applications in many industrial processes as "green" biocatalysts as they can be versatilely engineered [81] [82].

Small Laccase (SLAC) is a homotrimer laccase whose structure and mechanism of catalysis are objects of ongoing studies [83] [84] [85] [86] [87] because it operates with a different mechanism as compared to that of most MCOs. It features three identical domains, each one containing – like other MCOs – one Type-1 copper ion (T1Cu) and a trinuclear cluster (TNC) composed of one Type-2 (T2Cu) and two Type-3 (T3Cu) copper ions. The SLAC crystal structure is shown in Figure 5.1, with the three domains highlighted in different colors, and the T1Cu and TNC represented as orange and yellow spheres, respectively. The T1Cu works in pair with the TNC from an adjacent domain; the former acts as the oxidation center for the substrates, while the latter binds molecular oxygen and reduces it to water with the electrons coming from the T1Cu through the bridging aminoacid residues.

The copper ions in the fully oxidized SLAC all share a d^9 electronic configuration, exhibiting an electron spin $S = 1/2$ and thus being paramagnetic. The two T3Cu of the TNC are antiferro-magnetically coupled and are thus EPR-silent, while the T1Cu and T2Cu show clearly distinguish-able EPR spectra due to very distinct values of the A_z copper hyperfine component [81] [88]. When SLAC is fully reduced, the copper ions have a a d^{10} electronic configuration and are thus diamagnetic.

For the study of the present Chapter a particular mutant of SLAC was employed, namely the T1Cu-depleted (T1D) enzyme [85], henceforth referred to as T1D SLAC. In this mutant, the
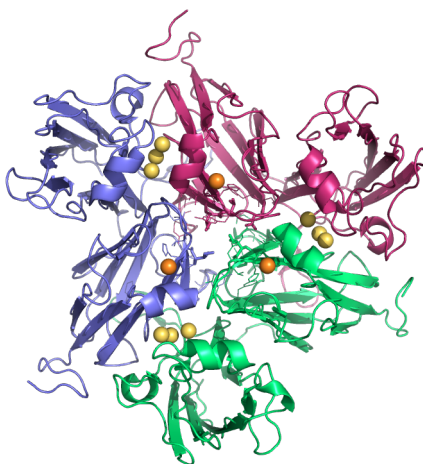
Figure 5.1: Ribbon depiction of the structure of wild-type SLAC (PDB 3CG8, from [84]). The three enzyme domains are highlighted in different colors. Type-1 copper ions are displayed as orange spheres, while Type-2 and Type-3 copper ions (forming the trinuclear copper clusters) are displayed as yellow spheres.

cysteine residue that coordinates the T1Cu in the wild-type SLAC is replaced by a serine residue, which results in an empty T1Cu site, while leaving the TNC intact. The T1D SLAC is still able to perform the reduction of O_2 to H_2O even without the T1Cu. EPR studies indicate that the role of T1Cu as electron donor in the fully reduced T1D SLAC is probably taken by a tyrosine residue, as suggested by the identification of a paramagnetic intermediate composed of a tyrosyl radical of spin $S = 1/2$ in exchange interaction with the T2Cu^{2+} of the TNC [85] [86] [30]. The tyrosyl radical is estimated to be located at a distance of about 5 Å from the T2Cu, which is confirmed by crystallographic data [84]. The T2Cu–Tyr intermediate biradical couple gives rise to a triplet signal at 9.5 GHz EPR that develops within milliseconds and fades away in hours [85].

In order to avoid confusion between the different forms of oxidized and reduced T1D SLAC, the scheme of Figure 5.2 summarizes the essential states of the TNC of the enzyme when it is subject to reoxidation, and provides a simplified scheme of the reoxidation (after [89]):

- The fully oxidized, *as-synthesized* enzyme, features a paramagnetic T2Cu^{2+} (blue) axially bound to a water molecule, and two T3Cu^{2+} (light blue) antiferromagnetically coupled and thus EPR silent. A tyrosine residue (Y$_{108}$), which will provide an electron for the reduction of oxygen, lies in the proximity of the TNC.

- Upon reduction with sodium dithionite ($Na_2S_2O_4$), all three copper atoms of the TNC turn to the diamagnetic Cu^+ oxidation state (green), and the enzyme is in its *fully reduced* state.

- After molecular O_2 binds to the TNC, the reduced copper ions are reoxidized (which occurs in several steps), and the tyrosine residue releases an electron, becoming the tyrosyl radical (orange). This state is the enzyme's *intermediate*, featuring a $T2Cu^{2+}$–Tyrosyl biradical couple.

- As the reduction of oxygen progresses, the tyrosyl radical receives an electron and the enzyme intermediate turns to its *reoxidized* form. Notice that the as-synthesized and reoxidized forms of T1D SLAC show slight differences structurally and spectroscopically, most likely owing to a different proton arrangement at the TNC.

A first high-frequency EPR characterization of the intermediate of T1D SLAC was attempted by Nami in her PhD thesis [30], where also the development as a function of time was studied at 9.5 GHz EPR with Rapid Freeze-Quench (RFQ). In that work, however, interpretation of the spectra at 275 GHz EPR remained doubtful; furthermore, RFQ does not come free of a number of drawbacks, such as sample packing and reproducibility, and amount of material required. Considering the achievements with the Temperature-Cycle EPR technique built up in the previous Chapters of this thesis, here are reported T-Cycle EPR experiments to study the sub-second reoxidation of T1D SLAC at 275 GHz, in an attempt to prove the applicability of the method to an enzymatic system, without making use of RFQ.

5.2 Experimental

5.2.1 Materials and setup

The batch of T1D SLAC was isolated following the procedure described by Canters *et al.* [83], and dissolved in phosphate buffer (100 mM, pH 6.8) at a concentration of 4 mM (determined spectrophotometrically with the extinction coefficient $\epsilon_{280} = 48$ mM^{-1} cm^{-1}). The as-synthesized enzyme solution was stored at -80 °C until use.

Reductions of the as-synthesized T1D SLAC solutions containing 20% in volume of glycerol (Sigma-Aldrich, puriss., cat. n. 15523-1L-R) were carried out in a glove box with slight nitrogen overpressure at room temperature, with a solution of sodium dithionite ($Na_2S_2O_4$, sodium hydrosulphite 82%, Sigma-Aldrich, cat. n. 71699-250G) in slight excess concentration. In order to

Figure 5.2: Forms of T1D SLAC in the reoxidation process, simplified from [89]: the as-synthesized (top), the fully reduced (right), the intermediate (bottom), and the reoxidized enzyme (left). Cu^{2+} ions are highlighted in blue or light blue, depending on whether they are Type-2 or Type-3, respectively; Cu^+ ions are highlighted in green. The tyrosyl radical is highlighted in orange. The arrows next to the paramagnetic species represent an unpaired electron, and their direction indicates whether they are ferro- or antiferromagnetically coupled.

obtain a reacting mixture to be studied with T-Cycle EPR, the fully reduced sample was mixed with oxygen-saturated solutions of phosphate buffer (100 mM, pH 6.8), bubbled for one hour with oxygen, in the ratio of 1:2 in volume. The fully reduced sample was checked with 9.5 GHz EPR to ensure that no signal was present. Two samples were prepared by differently mixing the fully reduced enzyme and the oxygen-saturated buffer:

- a sample hand-mixed at room temperature with final T1D SLAC concentration of 800 μM and glycerol 7% in volume. This percentage of glycerol is obtained by mixing one part of enzyme solution containing 20% in volume glycerol, with two parts of oxygen-saturated

buffer without glycerol. Upon manual mixing at room temperature in nitrogen atmosphere (which took about two minutes), the solution was immediately frozen and stored in liquid nitrogen until needed. This sample is henceforth referred to as "RT-mixed sample", and is described in Subsection 5.3.1;

- a sample mixed with the "sub-zero mixing" technique described in Chapter 4, with final T1D SLAC concentration of 800 μM and glycerol 50% in volume. This percentage of glycerol is obtained by mixing one part of enzyme solution, having 20% in volume glycerol, with two parts of oxygen-saturated buffer with 65% in volume glycerol. A glycerol content of 20% is such that at the temperatures described for the sub-zero mixing in Chapter 4 (namely, between -50 and -60 °C), the enzyme solution is solid. For this reason, the sub-zero mixing took place at a temperature of about -30 °C, obtained thanks to a cold atmosphere produced by blowing a flow of cold nitrogen gas on a layer of liquid nitrogen. The mixture spent up to 30 minutes at that temperature due to the procedure to pack it in the capillaries for the measurement. This sample is henceforth referred to as "cryo-mixed sample", and is described in Subsection 5.3.2.

The samples for 275 GHz EPR measurements were handled, prepared, and loaded into the spectrometer's probe head using the same low-temperature setup and procedure as described in Chapters 2 to 4.

The EPR measurements were carried out with a commercial 9.5 GHz EPR spectrometer and a home-built 275 GHz EPR spectrometer; details of both are provided in Chapter 2 of this thesis. The EPR experimental parameters used to record the EPR spectra of the T1D SLAC samples are summarized in Table 5.1. The 9.5 GHz spectra were averaged 4 times, while the 275 GHz spectra were averaged between 9 and 16 times.

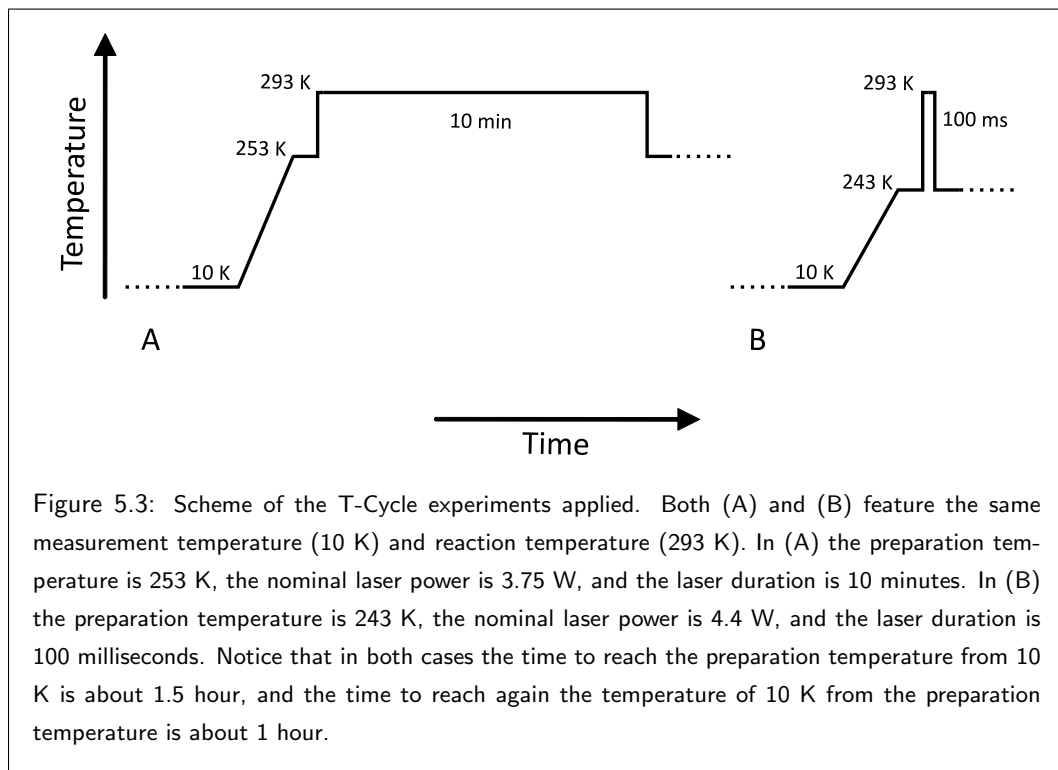| EPR freq. (GHz)	Field range (mT)	# of points	Mod. freq. (kHz)	Mod. ampl. (mT)	Time const. (s)	Conversion time (ms)	Microwave power (μW)	T (K)
9.5	250 ÷ 380	2048	100	0.5	0.3	82	100	40
275	8200 ÷ 10500	2300	1.253	0.7	1	500	1.28	10

Table 5.1: Experimental parameters of the EPR spectra at 9.5 GHz and 275 GHz. *Mod. freq.* and *Mod. ampl.* are the field modulation frequency and amplitude, respectively.

The T-Cycle hardware setup used here is the same one as described in Chapter 4 of this thesis. The duration and power of the laser pulses, and the temperatures involved here are summarized

in the scheme of Figure 5.3 and described below. In particular, since the ratio of water and glycerol is different in the two T-Cycle experiments performed here, in order to take the sample always to the temperature of +20 °C, the laser power and the preparation temperature (T_{prep}) employed had to be adjusted from case to case. It should be noticed that in both experiments the measurement temperature (T_{meas}) is 10 K, while the T_{prep}'s are more than 230 K higher: as opposed to the experiments described in Chapter 3 and 4 of this thesis, where T_{meas} and T_{prep} coincide, in this case it thus takes a certain amount of time (about one hour and a half) to reach the T_{prep} from the T_{meas}. From the moment the sample reaches the designated temperature and the moment the laser is turned on, an interval of less of half a minute elapses. The same applies when cooling down again to 10 K after the laser irradiation, which in total takes about an hour.

In the T-Cycle experiment described in Subsection 5.3.1 (shown in Figure 5.3 A), involving a 10 min continuous laser irradiation of the RT-mixed T1D SLAC sample containing as little as 7% in volume glycerol, a T_{prep} of -20 °C was selected, and a nominal laser power of 3.75 W. These were chosen after the laser calibration of Chapter 4: there it is shown how, with a power of 3.75 W and a composition of water and glycerol 1:1 in volume, a T-jump of about 50 °C is obtained. However, in [24] it is reported that in the absence of glycerol (i.e., a condition similar to the RT-mixed T1D SLAC sample), the laser-induced T-jumps are about 25% smaller than in the presence of 50% in volume glycerol. A T-jump of $\sim$ 40 °C is thus expected in this case, rather than of $\sim$ 50 °C derived from the previous Chapter. The final reaction temperature (T_r) of the sample is thus about +20 °C.

The T-Cycle experiment described in Subsection 5.3.2 involves two kinds of T-jump, applied on the cryo-mixed T1D SLAC sample: one induced by a laser pulse of the duration of 100 milliseconds (Figure 5.3 B), and one induced by continuous laser irradiation for the duration of 10 minutes, just like the one of the previous experiment (Figure 5.3 A). Since the sample of this experiment contains 50% in volume glycerol and the setup is identical to that described in Chapter 4, the same power calibration applies here. Therefore, for the 100 ms pulse a T_{prep} of -30 °C was selected, and a nominal power of 4.4 W; while for the 10 min continuous irradiation, a T_{prep} of -20 °C was selected, and a nominal power of 3.75 W. In both cases, the sample reaches a final T_r of +20 °C, although for the 100 ms pulse, this is achieved for a time much shorter than the duration of the pulse itself.

Figure 5.3: Scheme of the T-Cycle experiments applied. Both (A) and (B) feature the same measurement temperature (10 K) and reaction temperature (293 K). In (A) the preparation temperature is 253 K, the nominal laser power is 3.75 W, and the laser duration is 10 minutes. In (B) the preparation temperature is 243 K, the nominal laser power is 4.4 W, and the laser duration is 100 milliseconds. Notice that in both cases the time to reach the preparation temperature from 10 K is about 1.5 hour, and the time to reach again the temperature of 10 K from the preparation temperature is about 1 hour.

5.3   Results

In this section the EPR spectra at 9.5 and 275 GHz associated to the intermediate of T1D SLAC arising from the RT-mixed sample are reported, along with the spectrum at 275 GHz obtained after taking the RT-mixed sample to room temperature with a long laser-induced T-jump. For comparison, the spectrum of the fully oxidized T1D SLAC sample is also presented at the EPR frequency of 9.5 GHz. Furthermore, application of T-Cycle EPR to the cryo-mixed reduced T1D SLAC sample is described, and the spectra obtained are compared with the former ones used as a reference.

5.3.1   T1D SLAC sample mixed at room temperature

Since the manual mixing of the reduced T1D SLAC with oxygen-saturated buffer took about two minutes prior to freezing, the intermediate of T1D SLAC can still be detected, as its formation occurs within milliseconds, but conversion to the reoxidized enzyme takes hours [85]. Figure 5.4 A shows the 9.5 GHz EPR spectra at 40 K of the RT-mixed T1D SLAC sample (red),
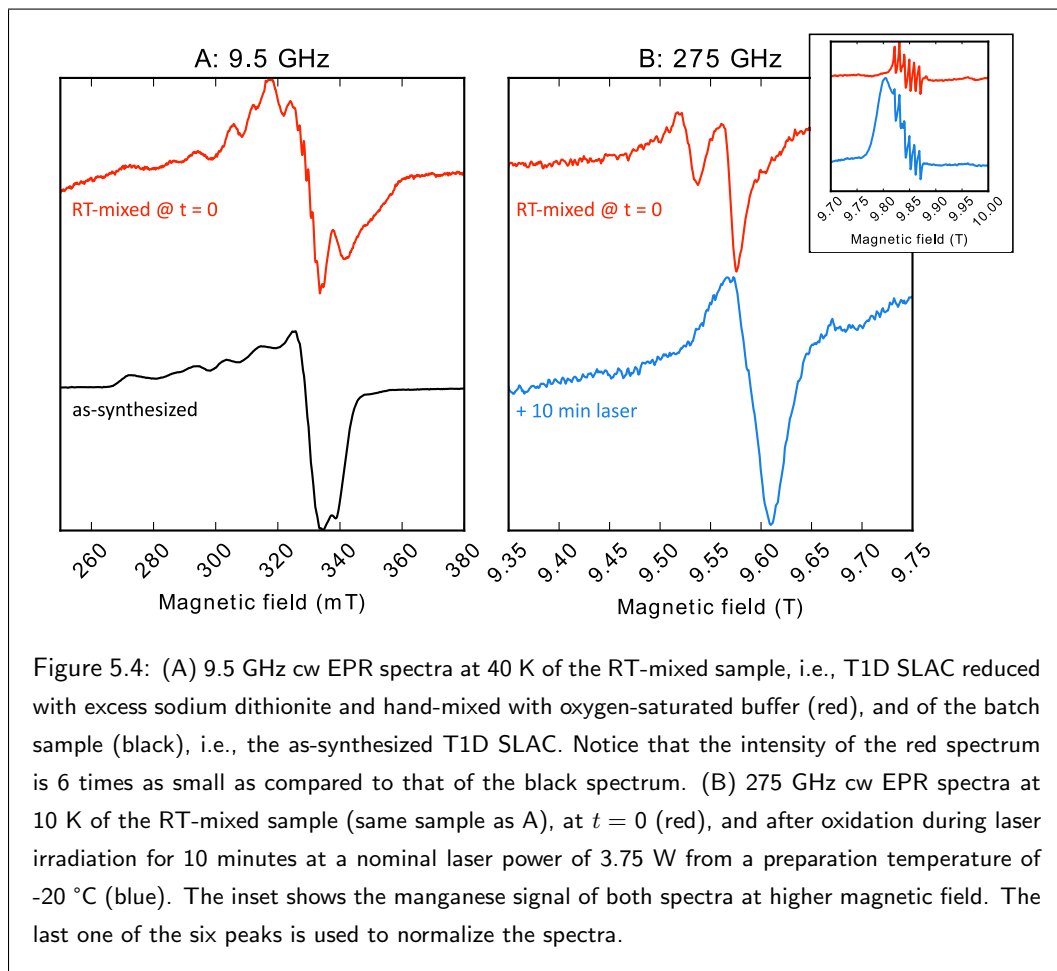
and of the as-synthesized T1D SLAC (black). By comparing with the literature [85], the red spectrum is assigned to the intermediate of T1D SLAC, while the black one is assigned to the fully oxidized as-synthesized T1D SLAC.

The same RT-mixed T1D SLAC sample studied at 9.5 GHz EPR was then measured at 275 GHz at 10 K, yielding the red spectrum of Figure 5.4 B. This spectrum, arising from the intermediate of T1D SLAC, features two peaks at $\sim$ 9.528 T and at $\sim$ 9.569 T. In order to achieve the spectrum of the reoxidized T1D SLAC (blue in Figure 5.4 B), the sample was taken to room temperature by continuously irradiating the sample at a nominal laser power of 3.75 W for the duration of 10 minutes from a preparation temperature of -20 °C. The blue spectrum of Figure 5.4 B features one single peak at $\sim$ 9.592 T, thus at a higher magnetic field value as compared to the spectrum of the intermediate. This spectrum matches with that of the reoxidized form of T1D SLAC, as confirmed by other measurements on the same system at the same frequency [88] [90], and suggests that the enzyme remains intact both after warming up from 10 K to -20 °C, and after irradiation to room temperature for a relatively long time. Both spectra of Figure 5.4 B also feature a Mn^{2+} signal at higher magnetic field, reported in the inset. The manganese signal partly originates from the buffer, as it was later detected in the spectrum of the oxygen-saturated buffer (see Subsection 5.3.2), and partly from the Mn^{2+} ions already present in the as-synthesized enzyme. The high-field manganese signal of the spectrum of the reoxidized enzyme overlaps with a more intense, broader signal of unknown nature.

5.3.2 Application of sub-second Temperature-Cycle EPR on the cryo-mixed T1D SLAC sample

Knowing the 275 GHz spectroscopic fingerprints of the intermediate and of the reoxidized form of T1D SLAC, T-Cycle EPR was applied on the cryo-mixed sample, namely the fully-reduced enzyme mixed with an oxygen-saturated buffer solution at a temperature of about -30 °C with the "sub-zero mixing" technique. Ideally, the sub-zero mixing should yield a system where no reaction has taken place, i.e., the fully reduced T1D SLAC. However, this turned out not to be the case, as the orange spectrum of Figure 5.5 was obtained, showing similarities with the spectrum of the intermediate of Figure 5.4 B, but with the peaks at a higher magnetic field, namely around 9.546 T and 9.594 T.

A T-Cycle of three steps was applied on the above mentioned cryo-mixed sample, each step consisting of heating the sample from the measurement temperature of 10 K to the preparation temperature of -30 °C, applying a laser pulse of the duration of 100 ms and of nominal power

Figure 5.4: (A) 9.5 GHz cw EPR spectra at 40 K of the RT-mixed sample, i.e., T1D SLAC reduced with excess sodium dithionite and hand-mixed with oxygen-saturated buffer (red), and of the batch sample (black), i.e., the as-synthesized T1D SLAC. Notice that the intensity of the red spectrum is 6 times as small as compared to that of the black spectrum. (B) 275 GHz cw EPR spectra at 10 K of the RT-mixed sample (same sample as A), at $t = 0$ (red), and after oxidation during laser irradiation for 10 minutes at a nominal laser power of 3.75 W from a preparation temperature of -20 °C (blue). The inset shows the manganese signal of both spectra at higher magnetic field. The last one of the six peaks is used to normalize the spectra.

of 4.4 W, and cooling the sample back to the measurement temperature of 10 K to record a spectrum. Such steps are schematically represented in Figure 5.3 B. It should be noticed that this kind of experiment is time-consuming: in one working day, two to three spectra can be recorded, due to the time required to take the sample from 10 K to 243 K or 253 K (about 1.5 hours) and back (about 1 hour) – not to mention that temperature stabilization at 10 K requires between two to three hours. Because of the insufficient quality of the spectra relative to the first and third step, here only the spectrum of the second step is shown (green in Figure 5.5), corresponding to a total laser time of 200 ms. It features a poorly defined signal in the magnetic field range of 9.55 ÷ 9.65 T.

Finally, upon continuously irradiating the sample for 10 minutes at a nominal laser power of

3.75 W from a preparation temperature of -20 °C (as represented in the scheme of Figure 5.3 A), the light blue spectrum of Figure 5.5 is obtained, with a distinct feature at $\sim$ 9.596 T. The close resemblance of this spectrum to the blue one of Figure 5.4 B, obtained after a 10 min irradiation of the RT-mixed sample and corresponding to the fully oxidized T1D SLAC, points to the fact that also in this experiment the enzyme remains intact after application of several cycles of temperature changes, whether cryostat-controlled or laser-induced.

All three spectra of Figure 5.5 also contain a complex structure at higher field, with the six peaks of Mn^{2+} clearly identifiable, superimposed on a signal broad several hundreds of mT, plus a smaller signal around 9.969 T. Such structure does not seem to belong to T1D SLAC, as the spectrum of the buffer used in the enzyme solution (shown in gray in the inset of Figure 5.5) displays the same structure – with the addition of a smaller peak around 9.621 T – which might thus be either in the buffer stock solution, or present in the microwave cavity (which was however checked and found clean prior to the experiments described here).

5.4   Discussion and conclusions

T-Cycle EPR has been applied for the first time on an enzyme-catalyzed reaction, namely the reduction of O_2 to H_2O via reoxidation of T1D SLAC. The results shown in this Chapter, however preliminary, suggest that T-Cycle EPR can be successfully employed in the investigation of enzyme kinetics.

Firstly, because the strong temperature differences the sample is subject to do not lead to irreversible denaturation or other damage of the enzyme – this being a known problem associated to the protein going through temperature changes and phase transitions of the solution [91]. The enzyme can thus undergo at least a few T-Cycle steps, which involve first going from the temperature measurement of 10 K to the preparation temperature (with a ΔT of at least 230 K), and from the preparation temperature to the reaction temperature (i.e., room temperature) through laser-induced T-jumps.

Secondly, a spectral change of the cryo-mixed sample was detected on the time scale of hundreds of milliseconds. Although the interpretation of the ill-defined spectrum of the cryo-mixed sample after 200 ms laser irradiation remains tentative (because of both the baseline and the background signal), this suggests that the road towards future experiments to be performed to investigate the T1D SLAC system further is now open.
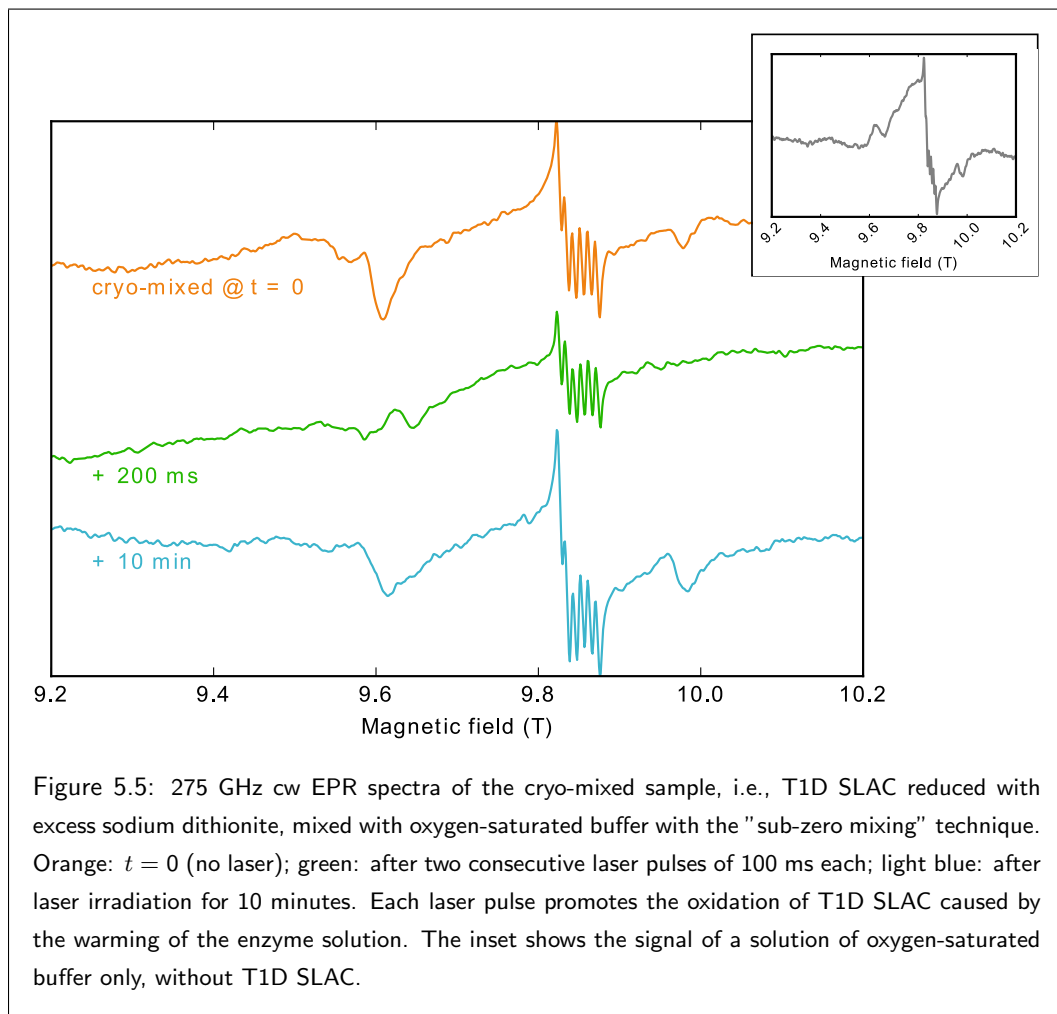
Figure 5.5: 275 GHz cw EPR spectra of the cryo-mixed sample, i.e., T1D SLAC reduced with excess sodium dithionite, mixed with oxygen-saturated buffer with the "sub-zero mixing" technique. Orange: $t = 0$ (no laser); green: after two consecutive laser pulses of 100 ms each; light blue: after laser irradiation for 10 minutes. Each laser pulse promotes the oxidation of T1D SLAC caused by the warming of the enzyme solution. The inset shows the signal of a solution of oxygen-saturated buffer only, without T1D SLAC.

Although not one of the motivations of the present research, for the first time the 275 GHz cw EPR spectrum of the intermediate of T1D SLAC is recorded here, with a structure clearly distinct from that of the reoxidized form. Such spectrum thus provides the basis for the description of the electronic structure of the intermediate, in combination with the data from 9.5 GHz EPR and possibly more frequencies. As mentioned earlier in this Chapter, the intermediate of T1D SLAC is currently understood as a triplet state originating from the coupling of the $S = 1/2$ spin of T2Cu^{2+} and of the $S = 1/2$ spin of a tyrosyl radical [85] [86] [88]. Given the high-spin nature of a triplet, a multi-frequency EPR approach is particularly advantageous in unraveling certain parameters of the spin Hamiltonian describing the system, especially regarding the dipolar

coupling and the exchange interaction of the two spins of the triplet. Further details on high-spin systems in EPR are provided in Chapter 1 of this thesis.

A comparison of the spectra obtained from the RT-mixed sample and the cryo-mixed sample indicates that the latter at $t = 0$ (orange spectrum in Figure 5.5) shows a signal, which does not correspond to the intermediate spectrum obtained from the RT-mixed sample (red spectrum in Figure 5.4), but rather it appears to contain at least a considerable amount of reoxidized T1D SLAC form. This is highlighted by the difference (shown in purple in Figure 5.6) between the spectrum of the hand-mixed sample at $t = 0$ and the spectrum of the RT-mixed sample after 10 min laser irradiation to room temperature, corresponding to the reoxidized T1D SLAC form. Although far from being conclusive, the difference clearly lacks the spectral feature of the reoxidized T1D SLAC form, while at the same time containing peaks roughly in the same field region as those of the spectrum of the T1D SLAC intermediate. These observations point to the fact that the sub-zero mixing of T1D SLAC with oxygen-saturated buffer has not resulted in a true $t = 0$ sample, but rather to one where part of the reaction has already taken place, and thus a mixture of the reoxidized form and of the intermediate are visible.

The main reason to the largely unsuccessful sub-zero mixing of the sample reported in this Chapter is to be found in the temperature at which the mixing took place, namely -30 °C instead of -50 ÷ -60 °C, like described in Chapter 4. The temperature of -30 °C might not have been low enough for the system under study not to react. For instance, supposing that at -30 °C the evolution of the intermediate of T1D SLAC (which occurs within milliseconds at room temperature) is slowed down by three or even four orders of magnitude, still the sample spends a long enough time at that temperature for the reaction to have progressed considerably. Indeed, the sample spends about 30 minutes at -30 °C during the procedure to mix the components and pack the capillaries, plus a couple of minutes more prior to the application of the laser-induced T-jumps.

Considering the non-standard conditions under which the sub-zero mixing of the enzyme was performed in this Chapter, and taking into account the successful results obtained with T-Cycle EPR on the sub-second time scale thanks to the sub-zero mixing in Chapter 4, there is reason to believe such method can be applicable to the study of the reoxidation of T1D SLAC and, more in general, to any kinetic investigation involving enzymes. Further experiments are required to prove the applicability of sub-zero mixing on such systems.

In conclusion, in this Chapter the applicability of Temperature-Cycle EPR was tested on the reoxidation of T1D SLAC, an oxygen-reducing enzyme. In particular, the experiments reported
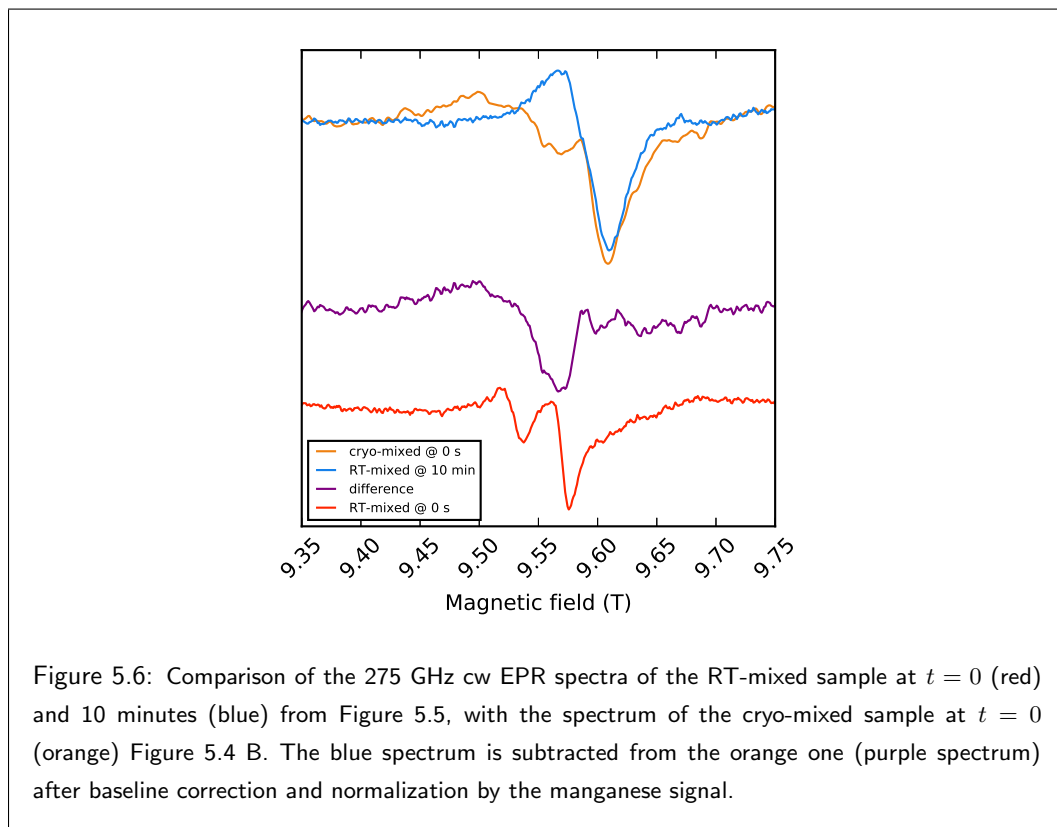
Figure 5.6: Comparison of the 275 GHz cw EPR spectra of the RT-mixed sample at $t = 0$ (red) and 10 minutes (blue) from Figure 5.5, with the spectrum of the cryo-mixed sample at $t = 0$ (orange) Figure 5.4 B. The blue spectrum is subtracted from the orange one (purple spectrum) after baseline correction and normalization by the manganese signal.

here suggest that T1D SLAC does not suffer from exposure to cyclic temperature changes, either cryostat-controlled or laser-induced (which took place continuously over days), thus making such system eligible for T-Cycle EPR. Moreover, the preliminary results of the application of laser-induced T-jumps of the order of hundreds of milliseconds point out that sub-second T-Cycle EPR on enzyme systems is feasible, provided a well-defined background-free sample at $t = 0$ is available. Achieving such starting sample by means of the sub-zero mixing technique described in Chapter 4 will require further testing, but there is no evidence that such goal is out of reach. By and large, there is indication that the way is paved towards investigations on enzyme kinetics with T-Cycle EPR.

Bibliography

[1] T.R. Cech. *Science*, 236:1532–1539, 1987.

[2] A. Hershko and A. Ciechanover. *Annual Review of Biochemistry*, 61:761–807, 1992.

[3] D. Mu, D. S. Hsu, and A. Sancar. *The Journal of Biological Chemistry*, 271, 1996.

[4] P. D. Mitchell. *Nature*, 191:144–148, 1961.

[5] P. D. Boyer. *Annual Review of Biochemistry*, 66:717–749, 1997.

[6] I. Langmuir. *Journal of the American Chemical Society*, 40:1361–1403, 1918.

[7] K. Christmann, G. Ertl, and T. Pignet. *Surface Science*, 54:365–392, 1976.

[8] A. H. Willbourn and C. N. Hinshelwood. *Proceedings of the Royal Society of London. Series A. Mathematical and Physical Sciences*, 185:353–369, 1946.

[9] M. J. Molina and F. S. Rowland. *Nature*, 249:810–812, 1974.

[10] W.B. Miller, S.A. Safron, and D.R. Herschbach. *Discussions of the Faraday Society*, 44:108–122, 1967.

[11] A. H. Zewail. *The Journal of Physical Chemistry A*, 104:5660–5694, 2000.

[12] K. Möbius and A. Savitzky. *High-Field EPR Spectroscopy on Proteins and their Model Systems*. RSC Publishing, 2009.

[13] D.A. McQuarrie and J.D. Simon. *Physical Chemistry: A Molecular Approach*, chapter 29, pages 1191–1193. University Science Books, Sausalito, CA, 1997.

[14] S. Arrhenius. *Zeitschrift für Physikalische Chemie*, 4U:96–116, 1889.

[15] K.J. Laidler and M.C. King. *The Journal of Physical Chemistry*, 87:2657–2664, 1983.

[16] H. Eyring. *The Journal of Chemical Physics*, 3:107–115, 1935.

[17] J.C. Polanyi and A.H. Zewail. *Accounts of Chemical Research*, 28:119–132, 1995.

[18] R.C. Bray. *Biochemical Journal*, 81:189–195, 1961.

[19] Update Instrument System 1000 Chemical/Freeze Quench Apparatus. User's manual.

[20] A.V. Cherepanov and S. de Vries. *Biochimica et Biophysica Acta*, 1656:1–31, 2004.

[21] R. Pievo, B. Angerstein, A.J. Fielding, C. Koch, I. Feussner, and M. Bennati. *ChemPhysChem*, 14:4094–4101, 2013.

[22] M. Eigen and L. De Maeyer. "Relaxation Methods" in *Technique of Organic Chemistry, Part II*, volume 8, pages 895–1054. Wiley Interscience, New York, 2nd edition, 1963.

[23] J. Kubelka. *Photochemical and Photobiological Sciences*, 8:499–512, 2009.

[24] M. Azarkh and E.J.J. Groenen. *Journal of Physical Chemistry B*, 119:13416–13421, 2015.

[25] J.A. Curcio and C.C. Petty. *Journal of the Optical Society of America*, 41:302–304, 1951.

[26] L. Kou, D. Labrie, and P. Chylek. *Applied Optics*, 32:3531–3540, 1993.

[27] K. Wang, W. Wen, Y. Wang, K. Wang, J. He, J. Wang, P. Zhai, Y. Yang, and P. Qiu. *Optics Express*, 25:5909–5916, 2017.

[28] N.M. Atherton. *Principles of Electron Spin Resonance*. Ellis Horwood – PTR Prentice Hall, 1993.

[29] A. Abragam and B. Bleaney. *Electron Paramagnetic Resonance of Transition Ions*. Oxford University Press, London, 1970.

[30] F. Nami. *PhD thesis*, chapter 4. Leiden University, April 2017. ISBN 9789085932895.

[31] S. Stoll and A. Schweiger. *Journal of Magnetic Resonance*, 178:42–55, 2006.

[32] R. Aasa and T. Vänngård. *Journal of Magnetic Resonance*, 19:308–315, 1975.

[33] J.H. Freed, G.V. Bruno, and C.F. Polnaszek. *Journal of Physical Chemistry A*, 75:3385–3399, 1971.

[34] H. Blok, J.A.J.M Disselhorst, S.B. Orlinskii, and J. Schmidt. *Journal of Magnetic Resonance*, 166:92–99, 2004.

[35] D.P. Ballou and G.A. Palmer. *Analytical Chemistry*, 46:1248–1253, 1974.

[36] S. Oellerich, E. Bill, and P. Hildebrandt. *Applied Spectroscopy*, 54:1480–1484, 2000.

[37] F. Nami, P. Gast, and E.J.J. Groenen. *Applied Magnetic Resonance*, 47:643–653, 2016.

[38] V. Schuenemann, F. Lendzian, C. Jung, J. Contzen, A.L. Barra, S.G. Sligar, and A.X. Trautwein. *Journal of Biological Chemistry*, 279:10919–10930, 2004.

[39] J. Manzerova, V. Krymov, and G.J. Gerfen. *Journal of Magnetic Resonance*, 213:32–45, 2011.

[40] R. Kaufmann, I. Yadid, and D. Goldfarb. *Journal of Magnetic Resonance*, 230:220–226, 2013.

[41] P.F. Lindley. *Reports on Progress in Physics*, 59:867–933, 1996.

[42] F. Nami. *PhD thesis*, chapter 3. Leiden University, April 2017. ISBN 9789085932895.

[43] G. Mathies, H. Blok, J.A.J.M. Disselhorst, H. van der Meer, D.M. Miedema, R.M. Almeida, J.J.G. Moura, W.R. Hagen, and E.J.J. Groenen. *Journal of Magnetic Resonance*, 210:126–132, 2011.

[44] A. Potapov and D. Goldfarb. *Applied Magnetic Resonance*, 37:845–850, 2010.

[45] D.E. Goldsack, W.S. Eberlein, and R.A. Alberty. *Journal of Biological Chemistry*, 240:4312–4315, 1965.

[46] A.J. Hoff, editor. *Advanced EPR: Applications in Biology and Biochemistry*. Elsevier, Amsterdam, 1989.

[47] A. Fersht. *"Structure and mechanism in protein science"*. W. H. Freeman and Company, New York, 1998.

[48] H. Roder, K. Maki, and H. Cheng. *Journal of Molecular Biology*, 106:1836–1861, 2006.

[49] E. Schubert, T. Hett, O. Schiemann, and Y. NejatyJahromy. *Journal of Magnetic Resonance*, 265:10–15, 2016.

[50] K. Kirschner, M. Eigen, R. Bittman, and B. Voigt. *Proceedings of the National Academy of Sciences of the United States of America*, 56:1661–1667, 1966.

[51] U. Mayor, C.M. Johnson, V. Daggett, and A.R. Fersht. *Proceedings of the National Academy of Sciences of the United States of America*, 97:13518–13522, 2000.

[52] F.P. Cavasino. *The Journal of Physical Chemistry*, 69:4380–4386, 1965.

[53] J.P. Kao and R.Y. Tsien. *Biophysical Journal*, 53:635–639, 1988.

[54] R. Rigler, C.R. Rabl, and T.M. Jovin. *Review of Scientific Instruments*, 45:580–588, 1974.

[55] J. Hofrichter. *"Laser Temperature-Jump Methods for Studying Folding Dynamics"* in *Protein structure, stability and folding*. Humana Press, Totowa, NJ, 2001.

[56] H. Staerk and G. Czerlinski. *Nature*, 205:63–64, 1965.

[57] H. Hoffmann, E. Yeager, and J. Stuehr. *Review of Scientific Instruments*, 39:649–653, 1968.

[58] R. Rigler, A. Jost, and L. De Maeyer. *Experimental Cell Research*, 62:197–203, 1970.

[59] W. A. Eaton, V. Muñoz, P.A. Thompson, E.R. Henry, and J. Hofrichter. *Accounts of Chemical Research*, 31:745–753, 1998.

[60] W. A. Eaton, V. Muñoz, S.J. Hagen, G.S. Jas, L.J. Lapidus, E.R. Henry, and J. Hofrichter. *Annual Review of Biophysics and Biomolecular Structure*, 29:327–359, 2000.

[61] R.B. Dyer. *Current Opinion in Structural Biology*, 17:38–47, 2007.

[62] A. Ansari, S.V. Kuznetsov, and Y.Q. Shen. *Proceedings of the National Academy of Sciences of the United States of America*, 98:7771–7776, 2001.

[63] R.H. Callender and R.B. Dyer. *Current Opinion in Structural Biology*, 12:628–633, 2002.

[64] S.V. Kuznetsov, A.G. Kozlov, T.M. Lohman, and A. Ansari. *Journal of Molecular Biology*, 359:55–65, 2002.

[65] O. Grinberg and L.J. Berliner, editors. *"Very High Frequency (VHF) ESR/EPR"* in *Biological Magnetic Resonance*, volume 22. Kluwer Academic/Plenum Publishers, New York, 2009.

[66] A. Potapov and D. Goldfarb. *Applied Magnetic Resonance*, 37:845–850, 2010.

[67] W.R. Couet, R.C. Brasch, C. Sosnovsky, J. Lukszo, I. Prakash, C.T. Gnewech, and T.N. Tozer. *Tetrahedron*, 41:1165–1172, 1985.

[68] Y.C. Liu, Z.L. Liu, and Z.X. Han. *Reviews of Chemical Intermediates*, 10:269–289, 1988.

[69] M. Shiga, Y. Miyazono, M. Ishiyama, K. Sasamoto, and K. Ueno. *Analytical Communications*, 34:115–117, 1997.

[70] A.A. Bobko, I.A. Kirilyuk, I.A. Grigor'ev, J.L. Zweier, and V.V. Khramtsov. *Free Radical Biology and Medicine*, 42:404–412, 2007.

[71] W.L. Hubbell, W. Froncisz, and J.S. Hyde. *Review of Scientific Instruments*, 58:1879–1886, 1987.

[72] Y. Lin, W. Liu, H. Ohno, and T. Ogata. *Analytical Sciences*, 15:973–977, 1999.

[73] M. Okazaki and K. Kuwata. *Journal of Physical Chemistry*, 89:4437–4440, 1985.

[74] *Physical Properties of Glycerine and its Solutions*. Glycerine Producers' Association, New York, 1963.

[75] N.A. Chumakova, V.I. Pergushov, A.K. Vorobiev, and A.I. Kokorin. *Applied Magnetic Resonance*, 39:409–421, 2010.

[76] M.H. Vos and J.L. Martin. *Biochimica et Biophysica Acta*, 1411:1–20, 1999.

[77] S.G. Mayhew. *European Journal of Biochemistry*, 85:535–547, 1978.

[78] V.M. Grigoryants, A.V. Veselov, and C.P. Scholes. *Biophysical Journal*, 78:2702–2708, 2000.

[79] G. Lassmann, P.P. Schmidt, and W. Lubitz. *Journal of Magnetic Resonance*, 172:312–323, 2005.

[80] E.I. Solomon, A.J. Augustine, and J. Yoon. *Dalton Transactions*, 30:3921–3932, 2008.

[81] P. Giardina, V. Faraco, C. Pezzella, A. Piscitelli, S. Vanhulle, and G. Sannia. *Cellular and Molecular Life Sciences*, 67:369–385, 2010.

[82] I. Pardo and S. Camarero. *Cellular and Molecular Life Sciences*, 72:897–910, 2015.

[83] M.C. Machczynski, E. Vijgenboom, B. Samyn, and G.W. Canters. *Protein Science*, 13:2388–2397, 2004.

[84] T. Skálová, J. Dohnálek, L.H. Østergaard, P. Rahbek Østergaard, P. Kolenko, J. Dušková, A. Štěpánková, and J. Hašek. *Journal of Molecular Biology*, 385:1165–1178, 2009.

[85] A.W.J.W. Tepper, S. Milikisyants, S. Sottini, E. Vijgenboom, E.J.J. Groenen, and G.W. Canters. *Journal of the American Chemical Society*, 131:11680–11682, 2009.

[86] A. Gupta, I. Nederlof, S. Sottini, A.W.J.W. Tepper, E.J.J. Groenen, E.A.J. Thomassen, and G.W. Canters. *Journal of the American Chemical Society*, 134:18213–18216, 2012.

[87] M.C. Machczynski and J.T. Babicz Jr. *Journal of Inorganic Biochemistry*, 159:62–69, 2016.

[88] F. Nami. *PhD thesis*, chapter 1. Leiden University, April 2017. ISBN 9789085932895.

[89] F. Nami. *PhD thesis*, chapter 6. Leiden University, April 2017. ISBN 9789085932895.

[90] S. Sottini and E.J.J. Groenen. Unpublished results.

[91] C. Scharnagl, M. Reif, and J. Friedrich. *Biochimica et Biophysica Acta*, 1749:187–213, 2005.

Summary

A wealth of information on chemically reactive systems can be derived by kinetic studies. In chemistry, knowledge of reaction rates and intermediates sheds light on the reaction mechanisms and, more in general, on the function of the (bio)chemical system under study in relation to its environment. However, an intrinsic difficulty of kinetic investigations are the time scales on which many chemical systems react, and the even shorter time scales on which their intermediates exist.

Rapid Freeze-Quench (RFQ) is one of the most widely used techniques to investigate chemical kinetics. Given the paramagnetic nature of the intermediates of many reactions, coupling RFQ to Electron Paramagnetic Resonance (EPR) is a desirable goal in order to unravel the structure, mechanism, and function of a range of reactive systems, such as enzymes. In particular, high-frequency EPR (HF-EPR) is the spectroscopic methodology of choice in studying paramagnetic species because it offers high resolution and better definition of the magnetic parameters. On the other hand, collection of RFQ samples for HF-EPR is troublesome since very small capillaries are used as sample holders. In **Chapter 2**, the successful coupling of RFQ to HF-EPR at 275 GHz is described. Sample collection performed with a previously developed method is efficient and reproducible. Furthermore, the approach allows the use of only one single series of RFQ samples, to be employed at any EPR microwave frequency, thus enabling multi-frequency EPR investigations. Important advantages of this approach are the reduced amount of material needed (which is particularly beneficial for biological samples), and the improved consistency of the method.

RFQ poses serious difficulties when it comes to sample packing, amount of material, and reproducibility, so that an alternative approach is highly desirable. **Chapter 3** describes the development of Temperature-Cycle EPR (T-Cycle EPR), a novel high-frequency EPR technique that couples laser-induced T-jumps of the sample to a high-frequency 275 GHz EPR spectrometer, in order to detect short-lived paramagnetic intermediates and kinetics of chemical reactions in aqueous solutions. In T-Cycle EPR, a mixture of reactants – initially at a temperature where

no reaction occurs – is heated in situ by means of an infrared laser pulse, in a homogeneous, reproducible, and controllable manner. This *in-situ* T-jump increases the temperature of the mixture so that the reaction can take place for an arbitrary period of time. The application of a sequence of T-jumps to the mixture thus lets the molecular reaction of interest unfold step by step, and a kinetic study of the chemical system is possible. In Chapter 3, it is first shown that T-Cycle EPR works, by observing a chemical reaction on the time scale of minutes. Secondly, a series of experiments are described to show that reactions at different temperatures can be studied, which makes T-Cycle a flexible and powerful technique for the investigation of (bio)molecular dynamics at temperatures other than room temperature, in contrast to RFQ. Thirdly, a method is described to calibrate the temperature of the sample. Important advantages of T-Cycle EPR are the use of only one sample to carry out a kinetic study, which does not pose limitations on the reproducibility of the sample preparation, and the need for only a small amount of material. Both characteristics are beneficial with respect to other methods that require larger amounts of material and/or multiple samples, such as RFQ.

Chapter 4 discusses the application of T-Cycle EPR on a model reaction that takes place over several hundreds of milliseconds, proving the technique is suitable for the study of many (bio)chemical systems. A new hand-mixing method is described to easily and efficiently mix the reagents at low temperatures without them reacting, which can in principle replace RFQ. Furthermore, quantitative kinetics can be obtained provided an analysis of the sample's temperature profile during the laser pulse is performed, which also yields the effective reaction time per T-jump, and the dependence of the rate constant on temperature. In its current state, T-Cycle EPR offers the advantages of HF-EPR with a time resolution already optimal for a wide range of (bio)chemical systems. Additionally, in studies whose goal is the investigation of the evolution of paramagnetic reaction intermediates rather than quantitative kinetics, the present setup could even be employed in the time regime of tens of milliseconds. Finally, COMSOL simulations provide some insights on future improvements of T-Cycle EPR, in terms of sample volume, cryostat temperature, and material of the sample holder.

A pioneering attempt to apply T-Cycle EPR to the study of an enzymatic system on the sub-second time scale is presented in **Chapter 5**. The system under study is the T1Cu-depleted mutant of Small Laccase (T1D SLAC), an oxygen-reducing enzyme, which oxidizes a number of diverse substrates. T-Cycle EPR experiments at 275 GHz are performed on the reoxidation in the sub-second time regime of fully reduced T1D SLAC, to prove the applicability of the method to an enzymatic system, without making use of RFQ. The experiments reported in Chapter 5 suggest that T1D SLAC does not suffer from exposure to cyclic temperature changes, thus making such

system eligible for T-Cycle EPR. Moreover, the preliminary results of the application of laser-induced T-jumps of the order of hundreds of milliseconds point out that sub-second T-Cycle EPR on enzyme systems is feasible.

Samenvatting

Kinetische studies kunnen een rijkdom aan informatie opleveren omtrent chemische reacties. Kennis van reactiesnelheden en tussenproducten verschaft inzicht in reactiemechanismen en, meer in het algemeen, in de functie van het (bio)chemisch systeem onder studie in relatie tot zijn omgeving. Een intrinsieke moeilijkheid in dergelijk onderzoek is echter de korte tijdschaal waarop veel reacties plaatsvinden en de korte levensduur van de tussenproducten.

"Rapid Freeze-Quench" (RFQ) is een van de meest toegepaste technieken bij de kinetische studie van chemische reacties. Gegeven het paramagnetische karakter van de tussenproducten van veel reacties is het gewenst deze techniek te koppelen aan Electron Paramagnetische Resonantie (EPR) om de structuur, het mechanisme en de functie van reagerende systemen als enzymen te ontrafelen. In het bijzonder geldt dit voor EPR spectroscopie bij hoge microgolffrequentie (HF-EPR), omdat deze techniek een hoog spectraal oplossend vermogen heeft en een nauwkeurige bepaling van magnetische parameters mogelijk maakt. Anderzijds is het maken van monsters voor HF-EPR niet zonder problemen gezien de sub-millimeter afmetingen van de monsterhouder bij hoge microgolffrequenties. In **Hoofdstuk 2** wordt de geslaagde koppeling van RFQ aan HF-EPR bij 275 GHz beschreven. Monstervoorbereiding volgens een eerder ontwikkelde methode blijkt redelijk efficiënt en reproduceerbaar in deze experimenten. Bovendien maakt deze benadering het mogelijk om met één enkele reeks monsters experimenten uit te voeren bij verschillende microgolffrequenties, hetgeen de effectiviteit van EPR zeer ten goede komt. Een belangrijk voordeel is dat minder materiaal nodig is dan in het standaard RFQ-EPR experiment, in het bijzonder relevant voor biologische monsters, en dat de resultaten van experimenten bij verschillende microgolffrequenties direct te koppelen zijn.

Een alternatieve benadering is echter gewenst, aangezien RFQ lastig blijft in de uitvoering, met name ten aanzien van monstervoorbereiding en reproduceerbaarheid. **Hoofdstuk 3** beschrijft de ontwikkeling van "Temperature-Cycle EPR" (T-Cycle EPR), een nieuwe hoog-frequent EPR techniek waarin laser geïnduceerde temperatuursprongen van een monster gekoppeld wor-

den aan 275 GHz EPR spectroscopie. Op die manier kunnen in waterige oplossing kortlevende paramagnetische tussenproducten worden gedetecteerd en kan de kinetiek van chemische reacties worden bestudeerd. In T-Cycle EPR wordt een mengsel van uitgangsstoffen – initieel bij een temperatuur waarbij geen reactie plaatsvindt – *in situ* op een homogene, reproduceerbare en controleerbare manier verwarmd door middel van een infrarood laserpuls. Daarbij bereikt het mengsel een temperatuur waarbij de reactie plaatsvindt gedurende een zekere, korte tijdsduur. Door toepassing van een reeks van infraroodpulsen, dat wil zeggen een reeks van temperatuursprongen, ontwikkelt de reactie zich verder en is een kinetische studie mogelijk. Hoofdstuk 3 laat eerst zien dat het principe werkt op een tijdschaal van minuten. Vervolgens worden een aantal experimenten beschreven die laten zien dat met T-Cycle EPR reacties bestudeerd kunnen worden bij verschillende temperaturen, in tegenstelling tot de RFQ-EPR techniek die werkt bij kamertemperatuur. Als laatste wordt een methode beschreven voor de calibratie van het monster in de EPR spectrometer. Belangrijke voordelen van T-Cycle EPR zijn dat één monster volstaat voor een volledige kinetische studie, waardoor reproduceerbaarheid van de monstervoorbereiding geen issue meer is en zeer weinig materiaal nodig is. Dit maakt de techniek superieur aan andere methoden die veel materiaal en/of meer monsters vragen, zoals RFQ.

Hoofdstuk 4 beschouwt de toepassing van T-Cycle EPR op een modelreactie die verloopt in een tijd van honderden milliseconden, waarmee de techniek bruikbaar wordt voor de bestudering van veel (bio)chemische systemen. Een nieuwe "hand-mixing" methode wordt geïntroduceerd waarmee uitgangsstoffen gemakkelijk en efficiënt gemengd kunnen worden bij lage temperatuur zonder dat deze al reageren, waardoor RFQ in principe overbodig wordt. Een kwantitatieve kinetische studie vereist een analyse van het temperatuurprofiel van het monster gedurende de laserpuls. Daarmee wordt het mogelijk de kinetische data te analyseren, en enerzijds deze data te interpreteren in termen van een effectieve reactietijd per temperatuursprong, anderzijds de temperatuurafhankelijkheid van de reactiesnelheid te bepalen. In zijn huidige vorm biedt T-Cycle EPR de voordelen van HF-EPR met een tijdsresolutie die al optimaal is voor een breed scala aan (bio)chemische systemen. In gevallen waarin de bestudering van de ontwikkeling van paramagnetische tussenproducten het doel is en niet zozeer een kwantitatieve kinetiek, kan T-Cycle EPR al ingezet worden op de tijdschaal van tientallen milliseconden. Tot slot worden simulaties met COMSOL besproken ter verkenning van de mogelijkheden om de tijdsresolutie verder te verbeteren door aanpassing van het monstervolume, de temperatuur van de cryostaat en het materiaal van de monsterhouder.

Een verkennende poging tot de bestudering van een enzymatische reactie met behulp van de nieuw ontwikkelde T-Cycle EPR techniek op een sub-seconde tijdschaal is het onderwerp

van **Hoofdstuk 5**. Bekeken is Small Laccase (SLAC), een enzym dat zuurstof reduceert onder oxidatie van verscheidene substraten. In het bijzonder betreft het een mutant van SLAC die de Type1 koper site mist (T1D SLAC). T-Cycle EPR experimenten bij 275 GHz zijn uitgevoerd aan de re-oxidatie van volledig gereduceerd T1D SLAC, om te laten zien dat de methode werkt voor de bestudering van een enzymatische reactie zonder dat gebruik gemaakt hoeft te worden van RFQ van het monster. De experimenten beschreven in Hoofdstuk 5 suggereren dat het enzym T1D SLAC niet lijdt onder de blootstelling aan temperatuurcycli, waardoor T-cycle EPR mogelijk wordt. Voorlopige resultaten van de toepassing van laser geïnduceerde temperatuursprongen van de orde van honderden milliseconden laten zien dat T-Cycle EPR aan enzymatische systemen inderdaad uitvoerbaar is.

Curriculum Vitae

Gabriele Panarelli was born on March 2nd, 1989 in Cuneo, Italy.

He obtained his Bachelor's degree in Chemistry in 2011 and his Master's degree in Physical Chemistry in 2013, both from the University of Turin, Italy. In his Master's degree experimental project, Gabriele studied surface holes in TiO_2 with Electron Paramagnetic Resonance (EPR), under the supervision of Prof. Elio Giamello and dr. Stefano Livraghi.

In 2013 Gabriele joined the group of prof. dr. Edgar Groenen as a PhD student at Leiden University, the Netherlands, to study spin systems and chemical kinetics with high-frequency EPR.

Since September 2018, Gabriele has been working as a managing editor for a portfolio of Physics journals at Elsevier, Amsterdam.

Acknowledgments

Like any successful human activity, this piece of research too is the result of an extended network of collaborations, both on a professional and on a human level, to whose members I would like to express my gratitude.

I am most grateful to my supervisor, prof. dr. Edgar Groenen, who gave me the chance to join his team in the first place, and who patiently and wisely supported my highly non-linear progress during my research. Without him believing in me and encouraging me to develop both scientifically and personally, I would not be at this point.

Some very special thanks go to dr. Peter Gast, whose immense knowledge of the instruments was simply pivotal whenever something broke down or stopped working – which happened more often than not. I am also very thankful for the opportunity he gave me to be his teaching assistant for three years.

An extremely important person in my path as a PhD student has been my friend and former colleague, dr. Mykhailo Azarkh. He was my guiding light during my first years at Leiden University, and kept carrying on that role even when he moved to Germany. There are no words with which I can express my gratitude towards him.

I am exceedingly thankful to a number of persons whose contributions to my work were paramount. Thanks to dr. Wolfgang Löffler for the big hand he provided in relation to my optical setup. His patience and expertise are exceptional, and I will never be able to thank him enough. Thanks to Harmen van der Meer and the Fine Mechanical Department, for always being ready and willing to help in relation to any aspect of the EPR spectrometers. Thanks to Bert Crama and the Electronics Department, for his fundamental role in developing and maintaining the laser setup for my experiments. Thanks to Jos Disselhorst and dr. Huib Blok, for their invaluable role in replacing the microwave mixer of the 275 GHz EPR spectrometer when it

broke down. Thanks to dr. Marcel Rost for his precious insights with the COMSOL software package. Last but not least, thanks to Henriette van Leeuwen for her exceptional assistance in administration and organization matters.

I highly appreciated the insightful conversations about EPR I had with dr. Martina Huber; the fun conversations about anything with my colleague Enrico Zurlo; and the advice I received from prof. dr. Michel Orrit.

Beside the professional support, I am extremely lucky for the care and warmth I received during these tough PhD years from a few special persons. A heartily thank you goes to Mr Jorrit van Wijk, who on countless occasions stretched out his hand to me to help me rise again during the darkest moments.

I am grateful for the fun and familiar time I spent with my friends Raffaella, Antonella, and Dimo, who contributed to making my experience here cheerful and light-hearted.

A loving thank you goes to my boyfriend Nikos, who in the last year withstood my moments of weakness with love and patience.

The most important acknowledgement and thanks are for my family. Not for a single moment did they stop encouraging me during these years, which distance made hard for all of us. Thank you mom, dad, and Annalisa, for constantly reminding me how proud you are of me, for teaching me to always stand tall, and for motivating me to always strive to be a better person. Thank you Gisella, for guiding and comforting me through your memories. Thank you Michelle, Sophie, and Ludovico, for the enthusiasm and joy you filled each of our yearned-for encounters. I love you all.